Investigation of the spectroscopic optical coherence tomography technique for tissue analysis

Tay, Benjamin Chia Meng

2012

Tay, B. C. M. (2012). Investigation of the spectroscopic optical coherence tomography technique for tissue analysis. Doctoral thesis, Nanyang Technological University, Singapore.

https://hdl.handle.net/10356/50702

https://doi.org/10.32657/10356/50702

Investigation of the Spectroscopic Optical Coherence Tomography Technique for Tissue Analysis

Tay Chia Meng, Benjamin

School of Electrical & Electronic Engineering

A thesis submitted to the Nanyang Technological University

in fulfillment of the requirement for the degree of

Doctor of Philosophy

2012

STATEMENT OF ORIGINALITY

I hereby certify that the work embodied in this thesis is the result of original research and has not been submitted for a higher degree to any other University or Institution.

20 January 2012

Date

Tay Chia Meng, Benjamin

For my beloved wife, *Ong Kye Zheng*, who is always steadfast in her love and understanding throughout the years. This work is dedicated to us and our future.

Acknowledgments

I am indebted to my supervisor Associate Professor Ng Beng Koon for accepting me as his PhD student, as well as for offering me invaluable advice and guidance throughout the course of this work. He also gave me numerous opportunities to explore the different aspects and collaborations of this PhD project. I wish to thank my fellow PhD colleagues Chow Tzu Hao, Fu Chit Yaw and Srivathsan Vasudevan for a great common experience and the countless discussions that we had, academic or otherwise, have always been stimulating and fun.

I am grateful to Prof. Thomas Loh and Judy Goh from National University Hospital – Dept. of Otolaryngology for kick starting my biomedical imaging studies by providing many tonsil samples for research. I am also very grateful to Prof. Alphonsus Chong, Dr He Min and Dr Aaron Gan from National University Hospital – Dept. of Hand and Reconstructive Surgery for providing me with countless tendon samples and also for many valuable discussions. I thank Dr Poh Wee Teng, Dahlia, Li Wen and Angie from Changi General Hospital – Histology Dept. for their invaluable help in processing histological samples. I give special thanks to Assoc. Prof Chia Tet Fatt from National Institute of Education – Dept. of Natural Sciences and Science Education for his special insight into botany which makes things so fun and interesting, and also for providing me with pigeon orchid roots which started the SOCT work.

I deeply appreciate the help and numerous enlightening discussions on tissue scaffolds with Jolene Liu from NTU – School of Chemical and Biological Engineering which helped me

immensely to learn about a new biomedical area. She also provided many samples of seeded SF scaffolds for SOCT imaging. I also wish to thank Yvonne Yee from Photonics Lab for her professionalism and for helping me out with more than equipment issues since my undergraduate days in the lab.

Special thanks to Prof. Jacob Phang from the National University of Singapore – Dept. of Electrical Engineering for the numerous discussions and his expert advice on my work.

Last but not least, I am grateful to my family for their understanding, constant love and support throughout the candidature.

Table of Contents

Abstract

Optical coherence tomography (OCT), a low coherence interferometric imaging technique, is a potentially useful tool for disease diagnosis and biological process monitoring. Spectral analysis of the OCT signals can yield additional information on the properties of scatterers in the sample, allowing tissue analysis and functional imaging to be performed. The objective of this work is to investigate the use of the spectroscopic OCT (SOCT) technique for biomedical applications. A systematic study was first carried out to determine an optimal metric for quantifying scatterer sizes using an improved SOCT analysis method. The proposed metric is then applied to the SOCT imaging of human palatine tonsil epithelial tissues for the purpose of cellular differentiation in disease management. In two tissue regeneration applications, the monitoring of stem cell seeded healing flexor tendons and fibroblast seeded silk fibroin scaffolds over time demonstrates the potential use of the SOCT method for observing cellular growth and quantifying cells of interest.

An 840 nm wavelength Fourier-Domain OCT (FD-OCT) imaging system was designed, built and characterized in this thesis. The FD-OCT system is first used to investigate the optical-biomechanical characteristics of normal and injured flexor tendons under load. OCT images reveal vertical and horizontal banding caused by different optical phenomena in the flexor tendons. Images of tendons under mechanical loading show the gradual disappearance of vertical bands caused by the collagen fibers straightening during stress. Microtears, which are not visible to the naked eye, were also observed within the tendon after the maximum load was removed. The results demonstrate that the OCT modality is

suitable for the non-invasive monitoring of tendon biomechanical properties and is potentially useful for assessing the quality of suture repair techniques.

The autocorrelation bandwidths of dual window (DW) SOCT *k*-space scattering profile of different-sized microspheres and their correlation to scatterer size were investigated. A dual bandwidth (DB) spectroscopic metric defined as the ratio of the 10% to 90% autocorrelation bandwidths is found to change monotonically with microsphere size and gives the best contrast enhancement for scatterer size differentiation in the resulting spectroscopic image. Spectroscopic images of microsphere samples based on the proposed DWDB metric showed clear differentiation between different-sized scatterers as compared to those derived from conventional short time Fourier transform (STFT) metrics. The DWDB metric was found to significantly improve the contrast in SOCT imaging and can aid the visualization and identification of dissimilar scatterer size in a sample. In applying the DWDB-SOCT technique to the imaging of human palatine tonsils, differences between connective tissue, epithelial and lymphoid cells are clearly observed in the spectroscopic images. The results show that the proposed DWDB-SOCT technique can potentially be used for the early detection of squamous cell carcinoma (SCC) in oral tissue.

The effect of bone marrow derived mesenchymal stem cells (BMSCs) on flexor tendon healing in a rabbit model is monitored using the proposed DWDB-SOCT technique. In this tissue regeneration monitoring study, four different groups based on the types of stem cells introduced to the injury site (fibrin glue control, 1M autologous BMSC, 1M allogeneic BMSC, 4M allogeneic BMSC) are established for comparison. Two time points, 3- and 8-week, are chosen to coincide with the fibroblastic proliferation and the collagen remodeling

phases of the healing process, respectively. While conventional OCT images show significant structural detail at the healing sites, no clear differences between the study groups can be observed. A scatterer size quantification method presenting the scatterer size of interest as a ratio with respect to the total scatterers in the spectroscopic image section is proposed. The results shows that BMSC-seeded tendons achieved a greater degree of healing at the 3-week time point compared to fibrin glue control tendon. At the 8-week time point, however, all BMSC seeded tendons shows identical healing levels as the fibrin glue control. Allogeneic BMSCs were found to perform better than autologous BMSCs in terms of collagen synthesized at the repair site.

Lastly, the DWDB-SOCT technique is used to monitor fibroblast cell proliferation in silk fibroin (SF) scaffolds. Time points of 1-, 3- and 5-week are chosen to give sufficient time for the fibroblasts to proliferate and the scaffolds are harvested every two weeks for imaging and analysis. Histological images of a blank SF scaffold and a MEF-seeded SF scaffold at the 5-week time point are also taken for comparison. The conventional OCT images only allow the micro and macro scaffold structural features to be observed. By contrast, clear differentiation is observed between the SF scaffold and fibroblast cells in the spectroscopic images. Cell proliferation rate in the scaffolds, quantified with the proposed scatterer size quantification method, is found to increase monotonically with time. The interaction between the fibroblasts and the scaffold can also be observed from the cell distributions in the spectroscopic images. In addition, the quantity of fibroblasts at the surface and inside the scaffold observed in the spectroscopic images reveals valuable information on tissue culture conditions.

List of Figures

List of Tables

Chapter 1 Introduction to Tissue Analysis

1.1 Motivation

During the past 100 years, the field of biomedical imaging has developed from Wilhelm Roentgen's original discovery of the X-ray in 1895 to the imaging tools of today, such as light microscopy, ultrasonography, X-ray computed tomography (CT), single photon emission CT (SPECT), positron emission tomography (PET) [1], and magnetic resonance imaging (MRI) [2-3]. These imaging technologies are based on the interaction of different forms of energy with tissues which can non-invasively create an image of a body structure from a patient or a laboratory animal [4]. There are broadly two imaging modes: *ex vivo* imaging where the sample is excised, prepared and imaged under a microscope, and *in vivo* imaging where the tissue is imaged within the patient (*in situ*). *Ex vivo* imaging systems are largely optical in nature and include brightfield microscopy, confocal microscopy, optical coherence microscopy (OCM), fluorescence microscopy, multiphoton microscopy (MPM) and second harmonic generation microscopy (SHGM) [2]. *In vivo* imaging systems such as X-ray imaging, CT, ultrasound, SPECT, PET and MRI typically offer less resolution than *ex vivo* systems, but have the advantage of real time imaging of the human body with less discomfort and faster recovery for the patient. Probe-based systems, e.g. endoscopic instruments, can image *in vivo* as well and optical techniques can be modified for *in vivo* imaging with the proper design of a probe [5].

Table 1-1 compares the capabilities of various imaging techniques. Most techniques are capable of *in vivo* imaging and are used for disease management and biological process monitoring. Optical imaging techniques are the most versatile, capable of *in vivo* and *ex*

vivo imaging with high resolution. Today, the role of novel biomedical imaging technologies is evolving in the same direction as the field of conventional medicine, i.e. away from a symptom-based problem assessment and diagnosis towards integrated solutions for specific health problems, including all aspects of diagnosis, staging, treatment and follow-up care. Methods such as SPECT and PET have emerged as highly sensitive functional imaging methods complementary to the structural imaging of CT and MRI, and are generating new paths in the development of sophisticated imaging techniques [4].

Table 1-1: A comparison of biomedical imaging modality capabilities [1, 3, 6-9].

Imaging Techniques	***ex vivo* Imaging Capability**	***in vivo* Imaging Capability**	**Used for Disease Management**	**Used for Biological Process Monitoring**
Optical Imaging	✓	✓	✓	✓
Ultrasound Imaging	-	✓	✓	✓
X-ray Imaging	-	✓	✓	✓
Nuclear Imaging (e.g. SPECT and PET)	-	✓	✓	✓
Magnetic Resonance Imaging	-	✓	✓	✓

In disease management, faster MRI sequences of the heart during stress can evaluate wall motion abnormalities [1] as well as image carcinoma [10]. PET is mainly used to image tumors non-invasively and both primary tumors and distant metastases [1, 11-14] can be detected. Multi-detector CT now allows for 4D (3D and dynamic) reconstruction of organ structure and function anywhere in the body [15]. Whole body imaging techniques are very powerful, but are usually used after the fact, when cancer has already occurred and

tumors have reached a certain size. It is not used for early cancer detection because of the limited resolution, e.g. the resolution of PET is 3 mm [3]. There is much room for the development of non-invasive depth-resolved optical techniques with high resolution and the ability to distinguish early dysplastic changes in epithelial tissue such as cell nuclei enlargement.

The monitoring and diagnosis of the tendon injury has been achieved by ultrasound [16-18] and MRI [19-20]. MRI techniques have the advantage of good soft tissue contrast and the ability to perform 3D imaging but its typical imaging resolution of about 1 mm [3] is not good enough for imaging tendon injuries compared to the ~150 μm resolution of ultrasound [8]. Besides offering a higher resolution than MRI, ultrasound imaging of tendons can be performed in real-time using a low-cost system. However, the small high-frequency probes operating in the range of 7.5 to 15 MHz required for ultrasound imaging are not widely available, and the quality and consistency of images taken is operator-dependent. In the study of the tendon healing process using advanced techniques like stem cell therapy [21-22], bright-field microscopy is conventionally used for the imaging of stained tissue sections. With optical techniques having a significantly better resolution than ultrasound imaging, cellular morphology and tissue features can be clearly observed. The histological assessment process, however, is time consuming and above all, destructive. Consequently monitoring of the healing process in the same tendon over a long time period is not possible. There is therefore a need for a non-invasive, high resolution, depth-resolved imaging technique with functional capability to better

investigate and understand injured tendon and the effect of stem cells on its healing process.

In tissue engineering applications, the imaging of tissue scaffold characteristics like pore size, porosity and strut size is achieved primarily by scanning electron microscopy (SEM) [23-25]. While this technique offers the highest resolution of ~3 nm, it is limited to imaging the surface features of a sample and the sample preparation process is also destructive. Micro-CT (μCT) has been used in bone tissue engineering to analyze scaffolds non-invasively, focusing on the imaging and quantification of scaffold characteristics like pore sizes, porosity and strut thickness [23]. It can also achieve precise measurements of bone growth into the scaffold and onto its surface. The advantages of the technique include high resolution (5−100 μm) and 3D imaging of tissue scaffold structure. The drawbacks of the technique are the use of harmful radiation and toxic contrast agents, and the limitation of tissue imaging mainly to bone tissue. MRI has also been used to image tissue growth in scaffolds, and can achieve relatively high resolution (~100 μm) using high field systems [26-27]. Tissue implantation after the scaffold tissue is ready can also be imaged *in vivo* with MRI. The disadvantages of the technique are poor resolution and only soft tissues with high water content, such as adipose tissue, can be imaged. Furthermore bones do not show up with good contrast in MRI images due to a low concentration of hydrogen atoms in them. The limitations of SEM, μCT and MRI highlights the need for a non-invasive, high resolution, depth-resolved imaging technique for imaging tissue scaffold structure and the monitoring of cellular proliferation in tissue engineering.

In addition to the imaging of tissue/cellular structure, functional information like blood flow, local chemical composition, local birefringence and cell sizes are very important for the diagnosis of disease and biological process monitoring. Some clinical imaging techniques are undergoing research development to add functional imaging capability [1]. The differentiation of cell sizes is particularly important in histopathology for the diagnosis of tissue state. Cell sizes above or below the norm in bulk tissue indicate abnormalities and the concentration and distribution of abnormal cells influence the final diagnosis by the histopathologist. For example, oral carcinogenesis is accompanied by normal cells undergoing cellular changes where the cell nucleus expands by almost 40% with little to no remaining cytoplasm [28-31] and malignant cells multiplying in the basal membrane of the mucosal tissue [32-33] between the epithelium and lamina propria. The main tool of the histopathologist is the light microscope, which is able to resolve features smaller than 1 μm, but tissue samples have to be taken from patients and biopsies carry a large degree of variation depending on the number and choice of sampling sites. An imaging tool with the requisite resolution for structural imaging and functional capability for cell size differentiation is needed to overcome this limitation. Anatomical imaging techniques like ultrasound, X-ray CT and MRI do not possess the resolution for cellular imaging. Functional imaging techniques like SPECT and PET are used for tumor imaging, but have limited resolution to identify early cancerous growths for early detection.

Optical coherence tomography (OCT) is an emerging non-invasive optical imaging technique for biomedical applications. OCT is used to obtain high resolution, cross-

sectional images of internal microstructures in biological tissue by measuring backscattered light from different transverse positions [34]. OCT is analogous to ultrasound in terms of working principle, using light instead of sound to detect and map out discontinuities in tissue structure by measuring the back reflected intensity of infrared light [35]. As an optical imaging technique, OCT can achieve free space spatial resolutions of 1–15 μm, one to two orders of magnitude finer than conventional ultrasound [36-37]. Unlike ultrasound, OCT does not require direct contact with the tissue being imaged. As light is strongly scattered in most tissues, the imaging depth of OCT is limited to a few millimeters, and thus imaging of structures deep in the body is not possible. However, a wide range of tissues can be accessed directly or via an endoscope [37]. The ultra-high imaging capabilities of OCT can provide diagnostic information on tissue microstructure that cannot be obtained using other biomedical imaging modalities. OCT has the potential to perform "optical biopsy" where tissue morphology can be determined *in situ* without the need for surgical excision. Furthermore functional extensions like spectroscopic OCT (SOCT) can be used to provide information on depth-resolved scatterer size and distribution [38-39], bringing a whole new dimension to functional OCT imaging of tissue. Thus OCT imaging can overcome many of the clinical imaging deficiencies discussed, having both the required resolution for cellular imaging as well as the functional ability to differentiate cell sizes. This puts OCT in a unique position as a potential biomedical imaging technique for disease management and biological process monitoring.

1.2 Objectives

The objectives of this thesis are briefly described below.

a) *Characterization of the biomechanical properties of flexor tendons with Fourier-domain OCT (FD-OCT)*

Imaging of normal and repaired tendons under different loading conditions can provide information for surgeons to monitor the state of tendon repair site during and post- surgery. While ultrasound and MRI imaging techniques can non-invasively monitor healing tendons, they suffer from a relatively poor resolution. OCT can potentially fill the need for a robust and high resolution method of imaging the cross-sections of tendons. The purpose of this work is to develop a FD-OCT system and investigate its use in evaluating the biomechanical properties of flexor tendons. This FD-OCT system will also be used in the subsequently development of a SOCT technique and its application in the monitoring of stem cell-seeded healing flexor tendons and fibroblast seeded silk fibroin scaffolds.

b) *Investigation of a spectroscopic metric for qualitative scatterer size differentiation in tissue*

Spectroscopic metrics for describing particle sizes are commonly derived from the analysis of the local spectral modulation in an OCT axial scan. The differentiation of scatterer sizes is affected by the choice of time-frequency transform and spectroscopic metric used in the analysis of the SOCT image. A systematic study of the local spectral modulation autocorrelation function derived from the use of various time-frequency transform is necessary to determine an optimal metric that

has the best sensitivity to scatterer size. The contrast enhancement achieved in this study will improve the qualitative and quantitative analysis of tissue scatterers in structural tissue images.

c) *Study of the effect of stem cells on flexor tendon healing with SOCT*

Tendon healing process can be controlled and accelerated using stem cell therapy. Stem cell-assisted tendon healing studies are typically performed with bright-field microscopic imaging of suitably stained tissue sections, which are time-consuming and destructive. The aim of this work is to investigate the use of SOCT and the optimized spectroscopic metric to study the effect of stem cells on flexor tendon healing.

d) *Study of cell growth in silk fibroin scaffolds with SOCT*

Tissue scaffolds have been used in tissue engineering applications to support, reinforce and organize the regenerating tissues. The design and optimization of tissue scaffolds require an accurate assessment of tissue regeneration and growth in these structures. The current methods of monitoring cell proliferation in tissue scaffolds are often time consuming, tedious and are usually destructive. SOCT can potentially overcome the disadvantages encountered in conventional tissue scaffold monitoring approaches. The objective of this work is to apply SOCT and the optimized spectroscopic metric to monitor and study the cell growth process in silk fibroin scaffolds.

1.3 Major Contribution of the Thesis

The major contributions of the thesis are:

a) An 840 nm wavelength FD-OCT imaging system was designed, built and characterized in this thesis. The FD-OCT system is first used to investigate the optical-biomechanical characteristics of normal and injured flexor tendons under load. OCT images reveal vertical and horizontal banding caused by different optical phenomena in the flexor tendons. Images of tendons under mechanical loading show the gradual disappearance of vertical bands caused by the collagen fibers straightening during stress. Microtears, which are not visible to the naked eye, were also observed within the tendon after the maximum load was removed. The results demonstrate that the OCT modality is suitable for the non-invasive monitoring of tendon biomechanical properties and is potentially useful for assessing the quality of suture repair techniques.

b) The autocorrelation bandwidths of dual window (DW) SOCT *k*-space scattering profile of different-sized microspheres and their correlation to scatterer size were investigated. A dual bandwidth (DB) spectroscopic metric defined as the ratio of the 10% to 90% autocorrelation bandwidths is found to change monotonically with microsphere size and gives the best contrast enhancement for scatterer size differentiation in the resulting spectroscopic image. Spectroscopic images of microsphere samples based on the proposed DWDB metric showed clear differentiation between different-sized scatterers as compared to those derived from conventional short time Fourier transform (STFT) metrics. The DWDB

metric was found to significantly improve the contrast in SOCT imaging and can aid the visualization and identification of dissimilar scatterer size in a sample. In applying the DWDB-SOCT technique to the imaging of human palatine tonsils, differences between connective tissue, epithelial and lymphoid cells are clearly observed in the spectroscopic images. The results show that the proposed DWDB-SOCT technique can potentially be used for the early detection of squamous cell carcinoma (SCC) in oral tissue.

c) The effect of bone marrow derived mesenchymal stem cells (BMSCs) on flexor tendon healing in a rabbit model is monitored using the proposed DWDB-SOCT technique. In this tissue regeneration monitoring study, four different groups based on the types of stem cells introduced to the injury site (fibrin glue control, 1M autologous BMSC, 1M allogeneic BMSC, 4M allogeneic BMSC) are established for comparison. Two time points, 3- and 8-week, are chosen to coincide with the fibroblastic proliferation and the collagen remodeling phases of the healing process, respectively. While conventional OCT images show significant structural detail at the healing sites, no clear differences between the study groups can be observed. A scatterer size quantification method presenting the scatterer size of interest as a ratio with respect to the total scatterers in the spectroscopic image section is proposed. The results shows that BMSC-seeded tendons achieved a greater degree of healing at the 3-week time point compared to fibrin glue control tendon. At the 8-week time point, however, all BMSC seeded tendons shows identical healing levels as the fibrin glue control.

Allogeneic BMSCs were found to perform better than autologous BMSCs in terms of collagen synthesized at the repair site.

d) The DWDB-SOCT technique is used to monitor fibroblast cell proliferation in silk fibroin (SF) scaffolds. Time points of 1-, 3- and 5-week are chosen to give sufficient time for the fibroblasts to proliferate and the scaffolds are harvested every two weeks for imaging and analysis. Histological images of a blank SF scaffold and a MEF-seeded SF scaffold at the 5-week time point are also taken for comparison. The conventional OCT images only allow the micro and macro scaffold structural features to be observed. By contrast, clear differentiation is observed between the SF scaffold and fibroblast cells in the spectroscopic images. Cell proliferation rate in the scaffolds, quantified with the proposed scatterer size quantification method, is found to increase monotonically with time. The interaction between the fibroblasts and the scaffold can also be observed from the cell distributions in the spectroscopic images. In addition, the quantity of fibroblasts at the surface and inside the scaffold observed in the spectroscopic images reveals valuable information on tissue culture conditions.

1.4 Organization of Thesis

Chapter 1 presents the motivation, objectives and major contributions of the thesis.

Chapter 2 reviews the principles of tissue analysis and the various medical imaging modalities. The background on tissue optics is also described.

Chapter 3 discuss the theory of OCT and provides a review of the SOCT technique. Important parameters related to these OCT techniques are elucidated.

Chapter 4 presents the design and development of a FD-OCT system and its characterization. The study of the biomechanical properties of normal and injured flexor tendons under load with FD-OCT is reported and discussed in this chapter.

Chapter 5 describes a systematic study of the local spectral modulation autocorrelation function using different-sized microspheres to identify an optimal DWDB spectroscopic metric for scatterer size differentiation. The differentiation of tissue scatterer sizes in tonsil samples with the proposed metric are also reported and discussed.

Chapter 6 details the use of the proposed spectroscopic metric developed in the previous chapter for monitoring the effect of BMSCs on healing in flexor tendons. The distribution of fibroblasts at the injury site for flexor tendons of 3 and 8 weeks healing time points are presented in the SOCT images. Quantitative analysis of fibroblast concentration at the injury site are performed and described.

Chapter 7 reports the monitoring of cell proliferation in fibroblasts-seeded SF scaffolds using SOCT. The SOCT images of blank and fibroblasts-seeded SF scaffolds at 1, 3, 5 weeks time points are presented and compared. Cell proliferation in the scaffolds over time is also quantified and discussed.

Chapter 8 concludes the thesis and summarizes the key contributions of this research project. Several recommendations are proposed for future work.

Chapter 2 Background

2.1 Tissue Analysis Overview

Tissue analysis provides an understanding of the structural and functional relationships of tissues which is critical to the advancement of clinical biology and biomedical applications. Tissue analysis includes the imaging and analysis of tissue samples for information on tissue state. Figure 2-1 shows the various applications associated with tissue analysis. Disease management, a major component of tissue analysis, focuses on early disease detection and diagnosis, and the monitoring of disease treatment [1].

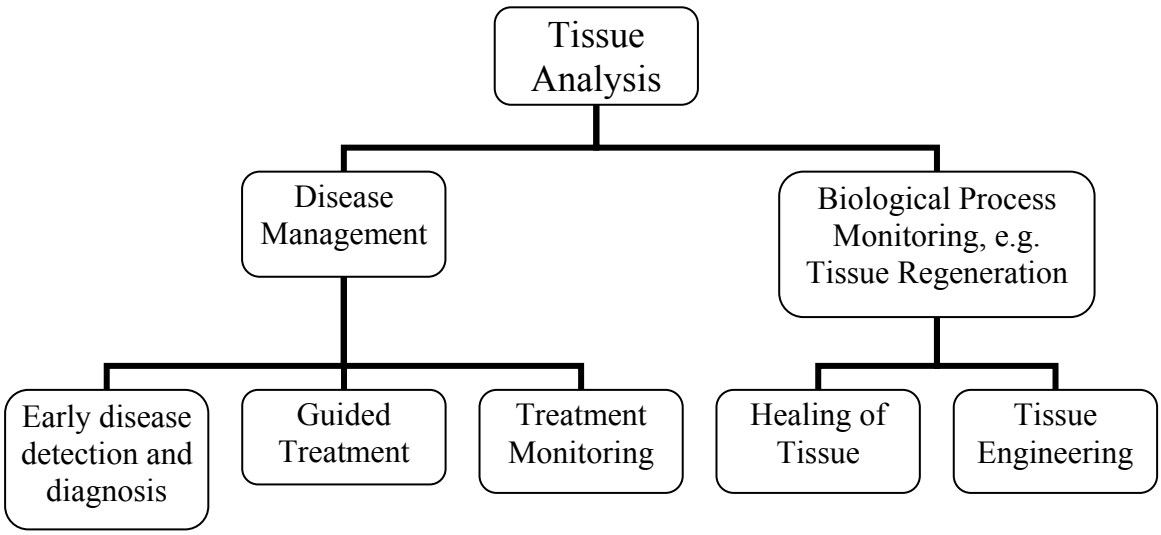

Figure 2-1: Some applications of tissue analysis [1, 21, 26-27, 40-41]

Another important application of tissue analysis is biological process monitoring, comprising the monitoring of tissue regeneration in tissue healing and tissue engineering. Tissue healing includes wound healing from burns [41] and tendon injury caused by loading stress, blunt force trauma, sharp force trauma and infection [40]. Recent developments in the tissue healing strategies involve the use of stem cells for accelerated

healing [21]. In tissue engineering, biological substitutes are created to restore, replace, or regenerate defective tissues and their function. Tissue engineering is a viable alternative option for organ replacement therapy and is the focus of regenerative medicine. Tissue is grown in a three-dimensional (3D) porous scaffold imbedded with stem cells and essential growth factors. Directing this process requires the tissue engineer to have a clear picture of the tissue growth. An accurate assessment of tissue regeneration is therefore essential to optimize the process of cell proliferation, tissue development and implantation [26-27].

The practice of medicine and study of biology have always relied on visualization to study the relationship of anatomic structure to biologic function and to detect and treat disease and trauma. Traditionally, these visualizations have been either direct, via surgery or biopsy, or indirect, requiring extensive mental reconstruction. The revolutionary capabilities of new 3D and four-dimensional (4D) medical-imaging along with computer reconstruction and rendering of multidimensional medical and histologic volume image data, eliminates the need for physical dissection or abstract assembly of anatomy. This provides many new opportunities for medical diagnosis and treatment, as well as for biological investigations [15].

The benefits of using sophisticated non-invasive medical imaging tools are already evident: more accurate and timely diagnosis of disease has translated into improved patient care [1]. However, substantial gaps remain both in our understanding of disease pathogenesis and in the development of even more effective strategies for early diagnosis

and treatment. Advances in biomedical imaging technologies can improve the understanding between the structural and functional relationships of cells and tissues, thereby facilitating the diagnosis and clinical management of disease and their respective responses to therapy.

2.2 Optical Imaging Modalities

The various optical imaging methods are illustrated in Figure 2-2. For bulk tissue or *in vivo* optical imaging, reflection methods are the most suitable as the tissue samples are simply too thick for transmission-based imaging. The reasons for the widespread use of optical imaging for biological tissue include [6, 42-43]:

a) Photons provide non-ionizing and safe radiation for biomedical applications.
b) Results are in real-time.
c) Optical systems can be incorporated into endoscopes via fiber-based systems for *in vivo* imaging.

A comparison of the technical specifications, operational requirements and advantages/disadvantages of the various medical imaging techniques are summarized in Table 2-1.

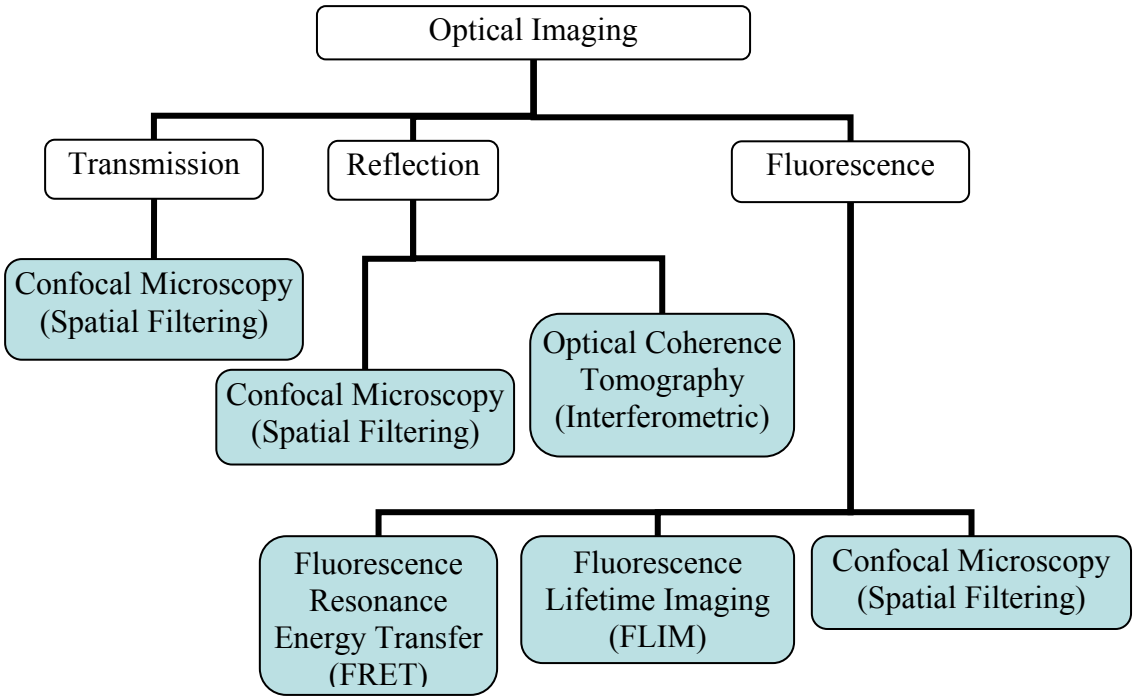

Figure 2-2: Optical methods of imaging [2]. Other optical methods not shown in the figure include multiphoton microscopy [44-48], second harmonic generation microscopy [49-53], diffuse optical tomography [54-55] and photoacoustic imaging [56-57].

Table 2-1: Comparison of technical specifications and operational requirements for biomedical imaging techniques [1-3, 6-9, 15, 43, 58].

Biomedical Imaging Techniques	Imaging Resolution	Imaging Depth	Radioisotope /Fluorescence marker	Advantages	Disadvantages
Confocal Microscopy	1μm	<250μm	Fluorescence marker	1. Highest imaging resolution, suitable for cellular and molecular imaging. 2. Can perform real time imaging. 3. *In vivo* (probe based) and e*x vivo* imaging capability.	1. For *ex vivo* imaging, sample biopsy and preparation needed. 2. Limited imaging depth.
Optical Coherence Tomography	2-15μm	2-3mm	None	1. Ability to perform structural and functional imaging. 2. Imaging resolution is close to confocal, sufficient for cellular imaging. 3. Can perform real time imaging. 4. Able to perform *in vivo* imaging.	1. Imaging depth is limited.
Ultrasound Imaging	150μm (10–150 μm using very high freq. US)	>10cm	None	1. Reasonable depth and good resolution for tissue level imaging. 2. Can perform real time imaging. 3. Contrast agents optional. (E.g. Microbubbles)	1. Imaging depth dependent on frequency used. 2. Contact with conducting medium is needed. 3. Cannot image through air. 4. Inability to distinguish between benign and malignant tumors.
Computed Tomography (X-ray)	300μm	Whole Body	Contrast Dye	1. Can perform whole body and near real time imaging.	1. High dosage of ionizing radiation. Not suitable for young patients. 2. Inadequate contrast of x-ray imaging for dense breasts, to distinguish between benign and malignant tumors.
SPECT Imaging	3mm	Whole Body	Radioisotope	1. Ability to image physiology and function.	1. Harmful radioactivity of radioisotopes.
PET Imaging	3mm	Whole Body	Radioisotope	1. Ability to image physiology and function.	1. Harmful radioactivity of radioisotopes.
MRI	1mm	Whole Body	None	1. Can perform whole body imaging. 2. Excellent soft tissue contrast.	1. No metal objects allowed within patient due to high magnetic field. 2. Inability to provide specific chemical information and any dynamic information like real-time tissue response to treatment or stimulus.

Elastic scattering is the most prevalent form of light interaction with biological tissue, as elastic scattering cross sections are several orders of magnitude larger than fluorescence or inelastic Raman scattering [59]. In a typical measurement, light incident on a sample is elastically scattered in different directions upon interaction with the scatterers in the sample. By measuring the magnitude, phase or wavelength dependency of the scattered light, the tissue structure and even the size of individual scatterers can be known.

Optical imaging provides structural and functional information with high spatial resolution via the following mechanisms [6, 42-43]:

a) Optical scattering spectra provide information about the size distribution of optical scatterers, such as cell nuclei.
b) Optical polarization provides information about structurally anisotropic tissue components, such as collagen and muscle fiber.
c) Optical frequency shifts due to the optical Doppler effect provide information about blood flow.
d) Optical spectra based on absorption, fluorescence, or Raman scattering provide biochemical information because they are related to molecular states.
e) Optical absorption reveals angiogenesis (related to the concentration of hemoglobin) and hypermetabolism (related to the oxygen saturation of hemoglobin), both of which are hallmarks of cancer.
f) Optical properties of targeted contrast agents provide contrast for the molecular imaging of biomarkers.

g) Optical properties or bioluminescence of products from gene expression provide contrast for the molecular imaging of gene activities.
h) Optical spectroscopy permits simultaneous detection of multiple contrast agents.
i) Optical transparency in the eye provides a unique opportunity for high resolution imaging of the retina.

Most optical imaging techniques make use of a microscope, thus the achievable spatial resolution is defined by the objective lens used. The penetration depth of light in tissue is limited due to the strong scattering of optical radiation in tissues. However, in the near-infrared part of the spectrum, soft tissues exhibit an "optical window" due to the fact that their scattering, absorption and fluorescence characteristics are much lower than in the visible band [6]. A brief overview of light microscopy, confocal microscopy and OCT for tissue imaging is presented in the following subsections.

2.2.1 Light Microscopy

The optical layout of a compound microscope is shown in Figure 2-3a. Light from a lamp illuminates a transparent specimen through a substage condenser. The transmitted light is collected by an objective which, together with the built-in tube lens, focuses the image of the specimen to the eyepiece for viewing. At the lowest part of the observation tube in infinity-corrected systems, a tube lens gathers the parallel beams of light emerging from the objective and focuses the resulting image at the plane of the fixed diaphragm of the eyepiece. The eyepiece, together with the curved cornea and lens of the eye, focuses the image on the retina of the observer. The ray diagram in Figure 2-3b shows a simplified

illustration of the image formation path in a microscope. The tube lens is removed from the diagram for clarity. The objective lens forms a real, inverted image (image 1) of an object placed just beyond its focal point. The eyepiece is placed such that image 1 falls inside its focal length, thus rendering a magnified virtual image.

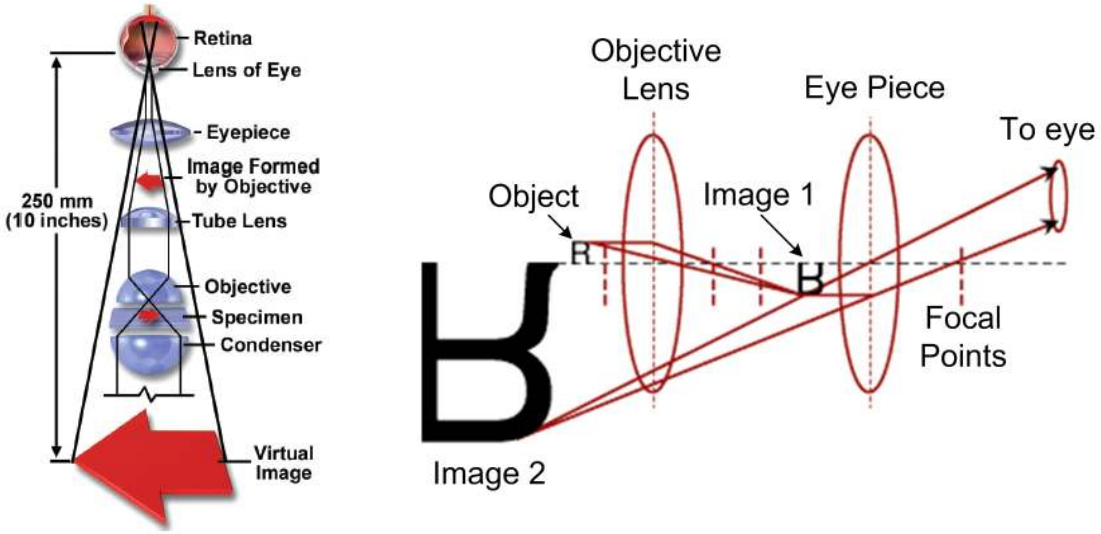

(a) (b)

Figure 2-3: (a) Compound microscope optical layout [60] and (b) ray diagram of the microscope image formation path [61].

The conventional way for sample illumination in light microscopy is through brightfield illumination, where the sample is placed directly in the light path, and contrast in brightfield images are achieved through optical scattering and absorption. The main use for light microscopy in a clinical setting is for histology, the gold standard in clinical tissue analysis and diagnosis [62]. In histology, a piece of tissue is excised from the region of interest in a patient. The tissue is immersed in formalin to extract water so that it can last without decay. The sample is fixed into a wax block where it is held into place on a microtome and cut into thin slices of about 5–10 μm thick. The slices are then

placed onto fresh microscope slides and inserted into a warm bath to melt the wax on the tissue slice before the slides are stained with chemicals to bring out the contrast of specific parts of the tissue under brightfield microscope observation.

One widely used stain for medical diagnosis is the hematoxylin and eosin (H&E) stain [62]. The staining method involves application of the basic dye hematoxylin which colors basophilic structures with blue-purple hue, and alcohol-based acidic eosin which colors eosinophilic structures bright pink, thus increasing contrast for identification and measurement of tissue or cell parameters. The basophilic structures are usually the ones containing nucleic acids, such as the ribosomes and the chromatin-rich cell nucleus, and the cytoplasmatic regions rich in RNA. RNA molecules play an active role in cells by catalyzing biological reactions, controlling gene expression, or sensing and communicating responses to cellular signals. The eosinophilic structures are generally composed of intracellular or extracellular protein. Most of the cytoplasm is eosinophilic. Consequently red blood cells are stained intensely red. Figure 2-4 shows a brightfield microscope image of an H&E stained human palantine tonsil section. Basophilic structures like the lymphoid cells are stained purple to almost black due to the high density of cells. The epithelium is also stained purple due to the presence of epithelial cells. Connective tissue has a low density of cells and consists of mainly elastin and extracellular protein, and is stained a light pink. Blood vessels contain red blood cells and are stained deep pink.

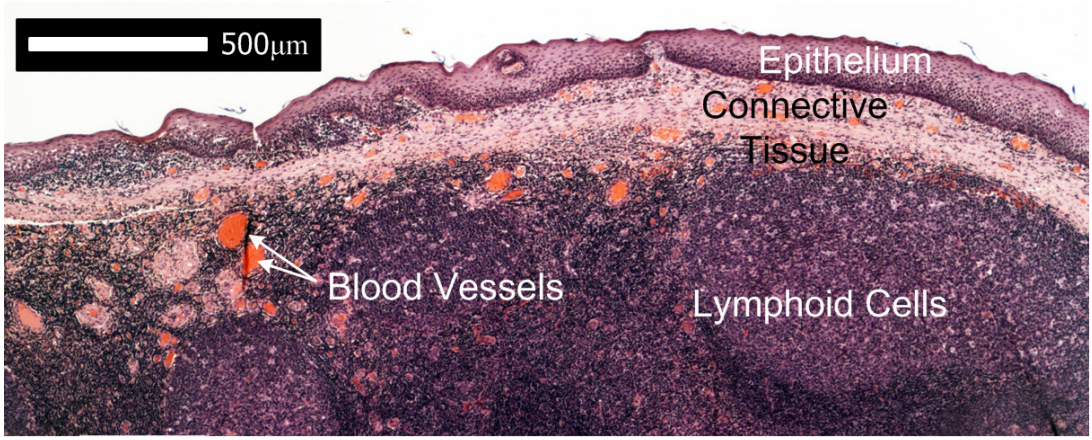

Figure 2-4: Brightfield microscope image of a H&E stained human palantine tonsil section.

2.2.2 Confocal Microscopy

In a conventional wide-field optical microscope, thick specimens produce an image that represents the sum of sharp image details from the in-focus region combined with blurred images from all the out-of-focus regions. This effect does not significantly deteriorate images at low magnification (10× and below) where the depth of field, defined by the distance between the upper and the lower planes of the in-focus region, is large. However, high numerical aperture (NA) objective lenses have a limited depth of field and the region where sharp specimen focus is observed can be 1 μm or less. As a result, a specimen having a thickness greater than 3–5 μm produces an image in which most of the light is contributed by the regions that are not in focus. The contribution from a blurred background reduces the contrast of the in-focus image. This problem is circumvented in confocal microscopy by introducing a confocal aperture, such as a pinhole, in the path of the light beam in front of the detector to reject the out-of-focus contribution [2]. Depending on the microscope objective used and sample properties, depth-resolved images at up to 150 μm depth can be achieved [63]. Measurement of

tissue or cell parameters can be achieved without histological processing, and contrast can be increased via fluorescence techniques [45, 64].

2.2.3 Light Scattering Spectroscopy and Low-Coherence Interferometry

Light scattering spectroscopy (LSS) makes uses of elastic scattering from epithelial cell nuclei to identify cell sizes. The LSS signal, with the diffuse component removed, is caused by photons that were single scattered by the cell nuclei and the frequency of the oscillations observed in the reflected spectra is governed by Mie scattering [65]. The frequency of the oscillations is proportional to the size of the cell nuclei and the amplitude of the signal is proportional to the density of the cells [66]. The main disadvantage of this method is that only cells near the tissue surface can be analyzed as the LSS signal from deeper tissue microstructures is extremely weak due to a high diffuse background.

Low-coherence interferometry (LCI) has been explored as an alternative for LSS in the detection of single scattered light from deep within tissue [67-69]. Angle-resolved LCI was used to obtain structural information by examination of the angular distribution of scattered light [70]. Recently, a new modality combining LSS and LCI called Fourier-domain LCI (fLCI) was reported [69]. In fLCI, depth-resolved structural information is Fourier transformed from the back-scattered light spectrum (similar to FD-OCT), and depth-resolved spectra are acquired from the structural information using a short-time Fourier transform (STFT) [68]. This process is similar to what is done in spectroscopic OCT up to this point for local scattering spectra, however, the two methods differs on how the local spectra is analyzed to retrieve scatterer information. In fLCI, LSS is used to

analyze the local spectra for scatterer sizes, but the accuracy of the sizes obtained is dependent on parameters like particle concentration which affects the SNR of the local spectral modulation and optical dispersion which affects local spectra [38, 68].

2.2.4 Optical Coherence Tomography

OCT obtains sub-surface images by interferometrically measuring optical reflections from within tissue. The reconstruction of the OCT cross-sectional image is based on the optical pathlengths that the back-scattered photons have propagated (Figure 2-5) in the axial direction (*z*-direction) with respect to transverse scanning (*x*-direction). Unlike ultrasound, light backscattered from tissue scatterers cannot be measured electronically due to the high speed associated with the propagation of light [71]. Low-coherence interferometry is used to demodulate the optical delay of light after tissue propagation and back scattering from tissue scatterers.

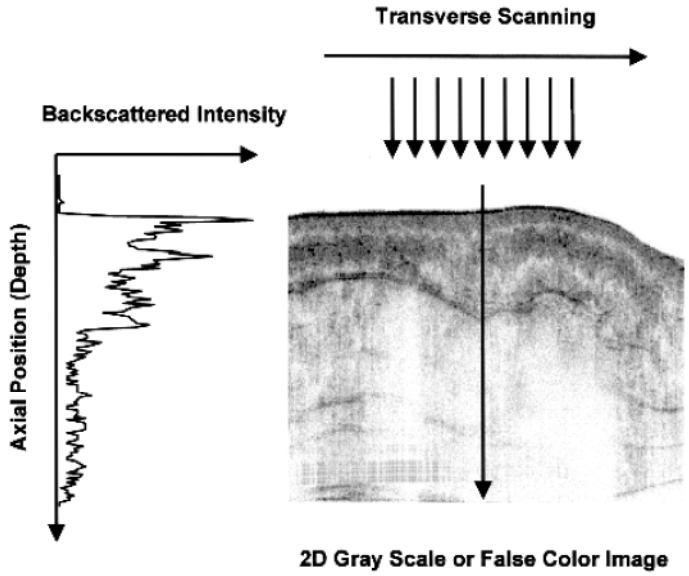

Figure 2-5: Image generation in OCT [35].

There are two main modalities of OCT: time-domain (TD-OCT) and Fourier-domain (FD-OCT). Both modalities are based on low-coherence interferometry but the detection of interference fringes and hence the demodulation of the fringes to give depth-resolved spatial information differs in both techniques. The main functional extensions to OCT are spectroscopic, Doppler and polarization-sensitive OCT and they can be used with TD-OCT or FD-OCT systems (Figure 2-6).

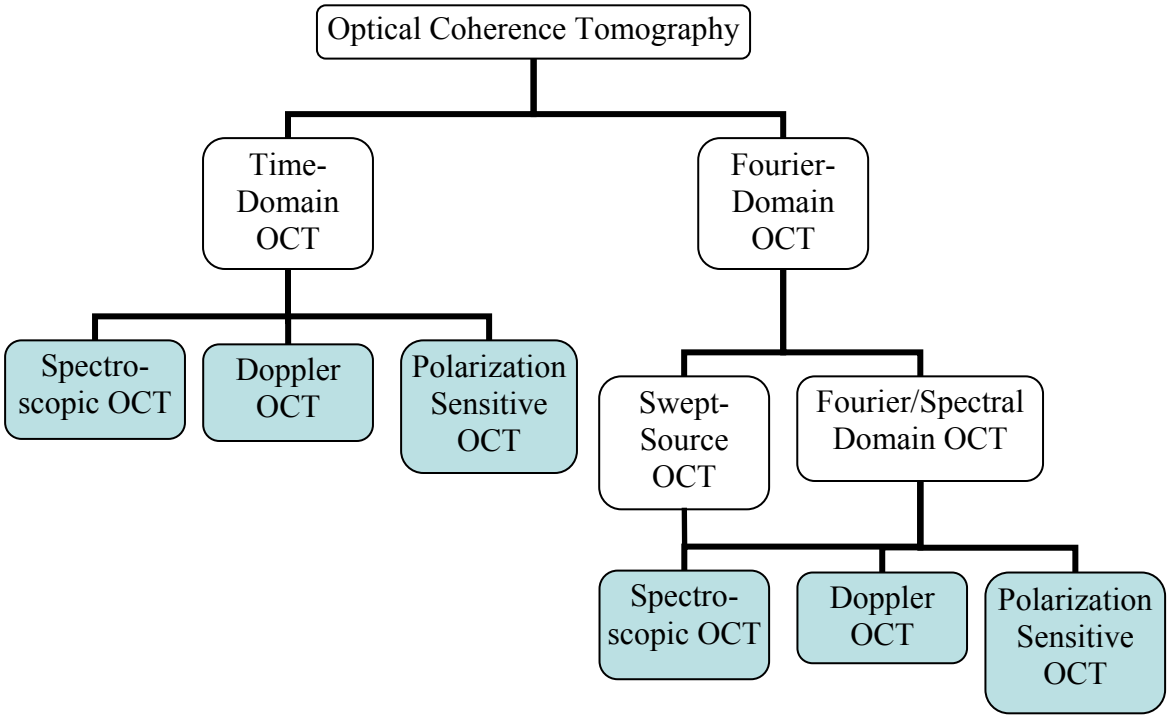

Figure 2-6: OCT modalities and their extensions.

In TD-OCT systems, an interferometer with a reference arm scanning mirror is used. Displacement of the reference beam with a scanning mirror produces the pathlength difference between the reference beam and the backscattered light from the sample [2]. Using a low-coherence source, the interference pattern between the reference beam and

the backscattered beam is produced when their path difference is within the coherence length. At a given location of the reference beam mirror, only a specific depth range (defined by the coherence length) of backscattered light will interfere. By scanning the reference mirror, the axial profile of the sample can be obtained. The limited scan speeds and lower system sensitivity of TD-OCT systems result from the use of the moving reference mirror and the large electronic bandwidth requirement of the single photo-detector [72-76], respectively.

The principle of FD-OCT is based on the Wiener-Khinchin theorem which states that a Fourier relationship exists between the power spectral density and the autocorrelation function of a process [77]. In other words, depth information, which is the autocorrelation of reference and sample arm light fields, can be obtained from the Fourier transform of interference fringes in the spectral domain. The whole depth structure (A-scan) is obtained synchronously with the spectral data and no depth scanning of the reference mirror is necessary. FD-OCT systems obtain depth information by evaluating the spectrum of the interferogram. The Fourier transformation of the spectrum delivers the depth information [78]. Due to the decoupling of reference mirror scanning and electronic detection bandwidth, FD-OCT enables a significant sensitivity advantage that allows increasing the line rate (A-scan rate) without losing imaging performance in comparison to TD-OCT [72-76]. Hence the achievable high speed imaging performance allows 3D tissue visualization and the study of *in vivo* functional tissue properties like perfusion and vessel pulsatility [79].

In comparison with other commonly known clinical imaging modalities like MRI, CT, ultrasound imaging and confocal microscopy, OCT fills a resolution and imaging depth gap between ultrasound and confocal microscopy, as shown in Table 2-1. MRI and CT, though non-invasive and non-destructive in their operation, do not offer the high resolution of OCT [80]. MRI and CT systems are expensive and require highly trained operators for daily operation. In addition, the highly ionizing radiation used in CT imaging is a health concern. While confocal fluorescence imaging requires fluorescent markers to be introduced into a sample as contrast agents, no sample preparation is needed for OCT. Although OCT utilizes the detection of backscattered photons like confocal microscopy, the sensitivity can exceed that of conventional confocal microscopes and signal-to-noise ratio (SNR) of more than 105 dB [76] can be achieved with heterodyne gain detection. Being an optical technique, OCT can also be integrated with a wide range of endoscopic probes that allow imaging during surgical procedures and enhances conventional white-light endoscopy with cross-sectional images [5]. Cellular-level image resolutions as fine as 1 μm have been demonstrated in biological specimens, allowing visualization of the mitotic cycle and tracking cell migration [5].

Structural information of a tissue sample is based on the amount of light backscattered by various tissue structures. Factors like cellular density and refractive index can affect the contrast of OCT images, making the differentiation of tissue microstructures difficult [36, 77]. During the early disease stages, the change in tissue scattering properties between normal and diseased tissue is small and difficult to measure. OCT has been widely used for imaging of human pathologies [32, 71, 81-97], where the utility of OCT for early

cancer detection in epithelial tissue were investigated. One of the greatest challenges for extending the clinical applications of OCT is to identify more contrast mechanisms that can provide physiological information in addition to morphological structure [36]. A number of extensions of OCT capabilities for functional imaging of tissue physiology have been developed. Doppler OCT (DOCT) combines the Doppler principle with OCT to obtain high-resolution tomographic images of tissue structure and blood flow simultaneously [98-103]. Polarization sensitive OCT (PS-OCT) combines polarization sensitive detection with OCT to determine tissue birefringence [104-113]. SOCT makes use of the broadband nature of the OCT light source to obtain the spectrum of backscattered light by depth dependent analysis [38, 114-118]. Spectroscopic differentiation is possible when two or more scatterer types in a sample backscatter differently over the wavelength range of the OCT light source. An example is illustrated in Figure 2-7: small scatterers give rise to low frequency spectral modulations and larger scatterers produce higher frequency spectral modulations. Early cancer detection is dependent on the location and differentiation of dysplastic and neoplastic cells by identifying cell nuclear morphology [28-31, 119-123]. Since the epithelial layers of mucosal and skin tissues are well within the detectable range of OCT, a method like SOCT is clearly important for the purpose of early detection of abnormal cellular changes through the identification and differentiation of tissue scatterer sizes. Furthermore, biological process monitoring like healing and tissue growth can be conducted using SOCT to track cell proliferation in an injury site and also cellular growth by differentiation cells from the surrounding tissue scaffold matrix. DOCT and PS-OCT do not have such capabilities as their strengths lies in other applications, such as the ability

to measure blood flow direction and the imaging of collagen, respectively. Table 2-2 shows the summary of the merits and drawbacks of FD-OCT in comparison to the SOCT functional extension.

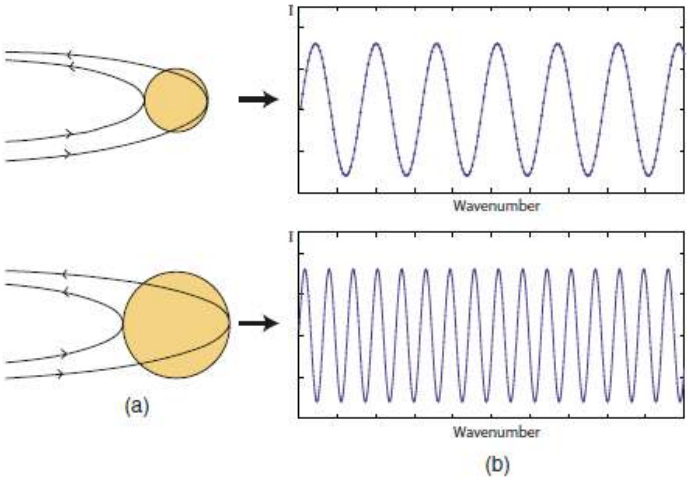

Figure 2-7: (a) Cell nuclei with incident and scattered fields indicated. (b) Interference spectra with wave number–dependent oscillations caused by interference between front and back surface reflections. [117]

Table 2-2: Comparison between the merits and drawbacks of FD-OCT and SOCT [36, 38, 77].

	Fourier-Domain OCT	**Spectroscopic OCT**
Advantages	− Depth-resolved structural imaging. − Non-invasive (no contact with sample needed). − 3D volumetric imaging. − High axial resolution (2–15 μm). − Real time imaging. − Non-ionizing radiation (Near-infrared light). − *Ex vivo* and *in vivo* imaging modalities available.	− Differentiation of scatterer sizes based on spectral analysis of back-scattered light. − Improved contrast of OCT images due to better differentiation of scatterers. − Qualitative and quantitative analysis of scatterers offer better understanding of biological phenomena.
Disadvantages	− Limited imaging depth (<3 mm).	− Extensive computational processing needed.

2.3 Tissue Optics

In order to image biological tissues using optical imaging modalities, it is important to understand their optical properties. Biological tissues are optically inhomogeneous and absorbing media whose average refractive index is higher than that of air. This is responsible for the partial reflection of light at the tissue/air interface (Fresnel reflection), while the remaining part penetrates the tissue. Multiple scattering and absorption are responsible for the broadening and eventual decay of light propagating through a tissue, whereas bulk scattering is a major cause of the dispersion of a large fraction of radiation in the backward direction. Therefore light propagation within a tissue depends on the scattering and absorption properties of its components: cells, cell organelles, and various fiber structures. The size, shape and density of these structures, their refractive index relative to the tissue ground substance and the polarization states of the incident light all play important roles in the propagation of light in tissues. Biological media are often modeled as ensembles of homogeneous spherical particles, since many cells and microorganisms, particularly blood cells, are close in shape to spheres or ellipsoids [124]. The scattering process in a tissue is complex (Figure 2-8), but Mie scattering is more commonly encountered in bulk tissue imaging as the sizes of cells and micro-organisms are comparable or much larger than the wavelength of excitation light [2]. The sizes of cells and tissue structure elements vary in size from a few tenths of nanometers to hundreds of micrometers. Most other mammalian cells have diameters in the range of 5–75 μm. There are a wide variety of structures within cells that determine tissue light scattering. Cell nuclei are on the order of 5–10 μm in diameter; mitochondria, lysosomes, and peroxisomes have dimensions of 1–2 μm; ribosomes are on the order of 20 nm in

diameter; and structures within various organelles can have dimensions of up to a few hundred nanometers. The hollow organs of the body are lined with a thin, highly cellular surface layer of epithelial tissue, which is supported by underlying, relatively acellular connective tissue. In healthy tissues, the epithelium often consists of a single well organized layer of cells with *en face* diameter of 10–20 μm and height of 25 μm [124].

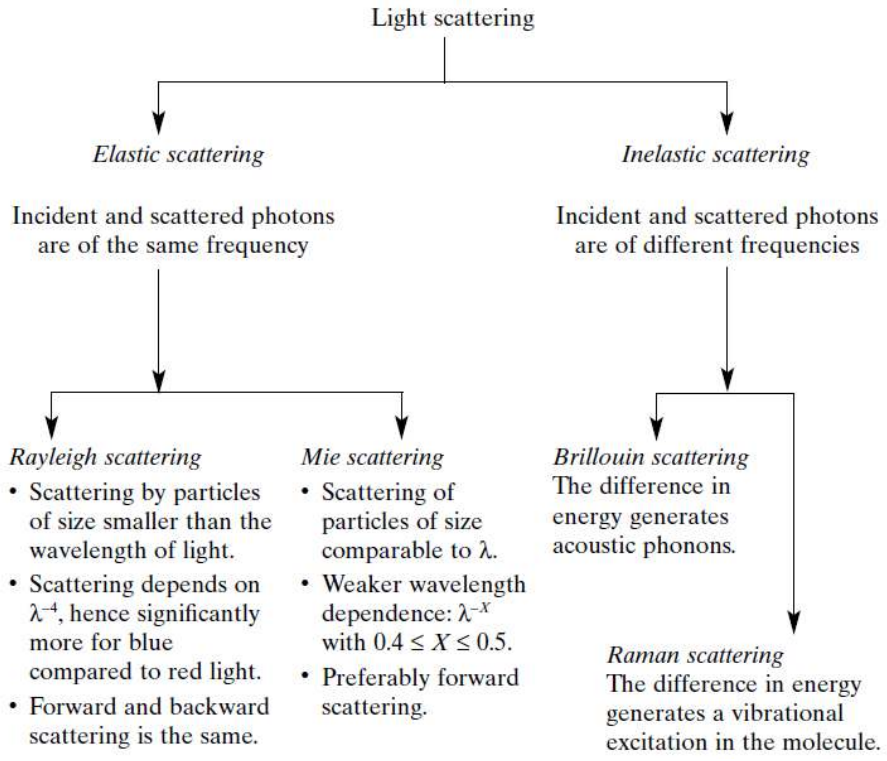

Figure 2-8: Various light scattering processes in tissues [2].

In the ultraviolet (UV) and infrared (IR) ($\lambda \geq 2000$ nm) spectral regions, light is readily absorbed, which accounts for the small contribution of scattering and the inability of radiation to penetrate deep into tissues (only through one or two cell layers). Short wavelength visible light penetrates typical tissues as deep as 0.5–2.5 mm, whereupon it undergoes an exponential decrease of intensity. This is due to the principal tissue

chromophores (hemoglobin and melanin) having high absorption bands at wavelengths shorter than 600 nm, but decreasing in magnitude with increasing wavelength (Figure 2-9) [124-125]. In this case, both scattering and absorption occur, with 15–40% of the incident radiation being reflected.

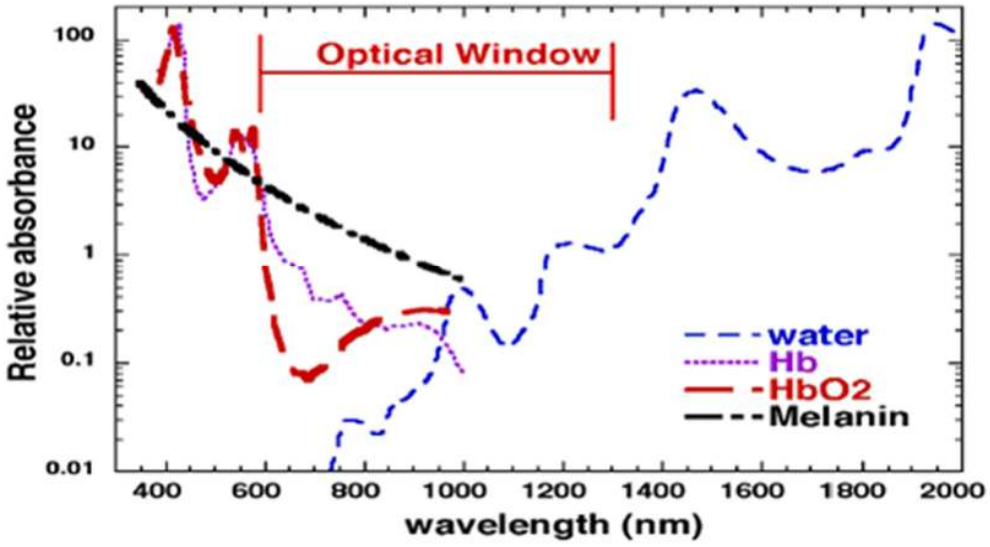

Figure 2-9: Absorption coefficients of primary biological absorbers [125].

At NIR wavelengths greater than 1300 nm, water absorption dominates. Water does not have any bands from UV to near IR, but starts absorbing weakly above 1.3 μm, with more pronounced peaks at wavelengths ≥ 2.9 μm and very strong absorption at 10 μm, the wavelength of a CO_2 laser beam [2]. In the 600–1600 nm wavelength range, scattering prevails over absorption, and light penetrates to a depth of 8–10 mm. At the same time, the intensity of the reflected radiation increases to 35–70% of the total incident light as a result of backscattering. For these reasons, there is a so-called 'optical

window' at red and near-IR wavelengths, between 600–1600 nm, where the effective tissue penetration of light and the backscattering of light is maximal for light imaging.

Chapter 3 OCT Theory

3.1 OCT Theory

The basic optical configuration of OCT is that of a Michelson interferometer, as shown in Figure 3-1. The light beam leaving the optical light source is spilt into two parts, a reference and a sample beam, $\overrightarrow{E_r}$ and $\overrightarrow{E_s}$ respectively. The reference beam is reflected off a mirror M1 at a fixed distance z_r from the beam splitter and the sample beam reflects off a sample, in this case, another mirror at a distance z_s from the beam splitter. Interference occurs when the path lengths of the reference and measurement arms are matched to within the coherence length of the broadband light source. The interference fringes are used to extract depth resolved information.

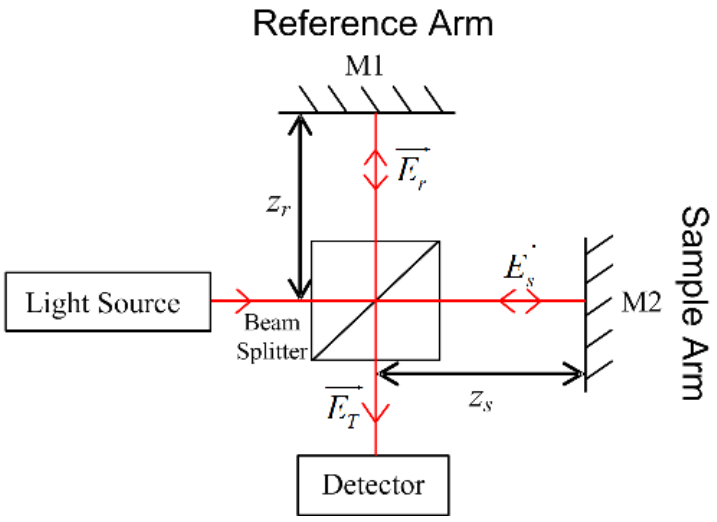

Figure 3-1: Michelson interferometric arrangement [126].

The E-field of a light wave, $\vec{E}(t)$, can be described as [127]:

$$\vec{E}(t) = \left[E_0 e^{-j(\vec{k}\bullet\vec{r}-\omega t)} \right] \cdot \hat{e_r} \tag{3.1}$$

where E_0 is the wave amplitude, $\vec{k}$ is the wave vector, $\vec{r}$ is the position vector, ω is the frequency of the wave and $\hat{e_r}$ is the unit vector in the direction of wave propagation.

The reflected reference arm light wave $\overrightarrow{E_r}$ from mirror M1 can be represented by:

$$\overrightarrow{E_r}(t) = \left[E_r e^{-j(k\bullet 2z_r-\omega t)} \right] \cdot \hat{e_z} \tag{3.2}$$

where $k = \frac{2\pi}{\lambda}$ is the propagation constant, λ is the wavelength of the light source and $\hat{e_z}$ is the unit vector in the z-direction. Similarly, the reflected sample arm light wave $\overrightarrow{E_s}$ from mirror M2 is written as:

$$\overrightarrow{E_s}(t) = \left[E_s e^{-j(k\bullet 2z_s-\omega t)} \right] \cdot \hat{e_z} \tag{3.3}$$

The difference in displacement z' between M1 and M2 is given by:

$$z' = z_s - z_r \tag{3.4}$$

The total electric field $\overrightarrow{E_T}$ at the beam splitter after $\overrightarrow{E_r}$ and $\overrightarrow{E_s}$ interfere is

$$\overrightarrow{E_T}(t) = \overrightarrow{E_r}(t) + \overrightarrow{E_s}(t) = \left[E_r e^{-j(k\bullet 2z_r-\omega t)} + E_s e^{-j(k\bullet 2z_s-\omega t)} \right] \cdot \hat{e_z} \tag{3.5}$$

The intensity detected at the detector can be shown to be [126]:

$$\begin{aligned} I &\propto \mathrm{Re}\left[\overrightarrow{E_T}(t) \bullet \overrightarrow{E_T^*}(t) \right] \\ &= E_r^2 + E_s^2 + 2E_r E_s \cos\left[k\bullet 2(z_s - z_r) \right] \\ &= E_r^2 + E_s^2 + 2E_r E_s \cos(2kz') \end{aligned} \tag{3.6}$$

The two self interference terms E_r^2 and E_s^2 are not used in OCT, but the cross-correlation term $2E_rE_s\cos(2kz')$ describes the interference fringes that occur when z_r and z_s are within the coherence length of the light source. Signal processing is performed on the interference term to obtain the spatial location of tissue layers.

3.2 Time-Domain OCT (TD-OCT)

In TD-OCT, the axial profile $I(z)$ of a sample can be shown to be the sum of the relative amplitudes of the sample arm at various depths z_n' [36]:

$$I(z) \propto 2\sum_{n=1}^{N} E_r(z) E_{s_n}(z) g(z) \cos\left[2k_0\left(z_{s_n} - z_r\right)\right] \quad \textbf{(3.7)}$$

where $k_0 = \frac{2\pi}{\lambda_0}$, λ_0 is the center wavelength of a broadband light source, N is the number of tissue layers and $g(z)$ is defined as the degree of coherence represented by the autocorrelation of the light source spectrum. E_{s_n} represents the back-scattered E-field from interfaces, denoted by n, within the sample. The sample is approximated as a stack of reflecting interfaces to simplify the model, however actual tissue may have scattering sites or specular reflecting sites, apart from layers.

The first OCT system developed was a TD-OCT system for imaging the retina and the coronary artery, two clinically relevant examples that are representative of transparent and turbid tissue [34], respectively. Imaging was performed using a fiber-optic Michelson interferometer with a low coherence length light source (Figure 3-2a). The fiber-optic implementation provides a compact and robust system that can be interfaced to a variety of clinical imaging instruments. Low coherence light can be generated by compact

superluminescent diodes (SLD) or ultrafast laser sources like the Ti:Sapphire lasers [36]. One interferometer arm contains a modular probe that focuses and scans the light on the sample, and also collects the backscattered light. The second interferometer arm is a reference path with a translating mirror or scanning delay line. Figure 3-2b shows the simulated interferogram of a sample with three optical interfaces. Interference occurs when the reference mirror translates to the equivalent position of an optical interface. The interference fringes are detected and demodulated to produce a measurement of the magnitude and echo delay time of light backscattered from structures inside the tissue.

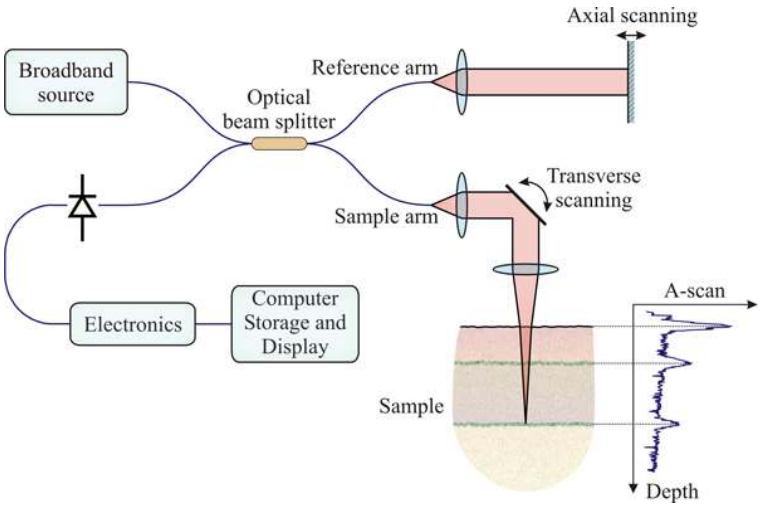

(a)

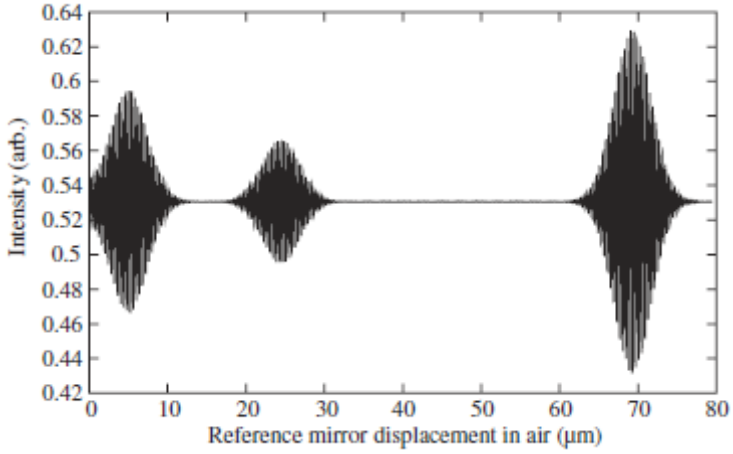

(b)

Figure 3-2 (a) Schematic of a TD-OCT system [58] and (b) the simulated interferogram of a sample with three optical interfaces [126].

Low-coherence interferometry enables femtosecond time resolution of optical echoes corresponding to micron-scale distance measurement, something which direct time-of-flight electronics cannot achieve. In TD-OCT, 2D cross-sectional images of internal tissue microstructure are constructed by scanning the optical beam and performing multiple axial measurements of backscattered light at different transverse positions. The resulting data set is a 2D array that represents the optical backscattering or reflection

within a cross-sectional slice of the tissue specimen. These data can be digitally filtered, processed and displayed as a 2D gray-scale or false-color image.

3.3 Fourier-Domain OCT (FD-OCT)

Fourier domain detection was developed [72-76, 79, 128] in early 2000 where the depth information in an axial scan (A-scan) is obtained simultaneously without mechanical scan of the reference arm. The acquisition speed is only limited by the read-out rate of the CCD array in the spectrometer. FD-OCT therefore has a much higher scan speed over TD-OCT [73, 128]. An ultra high speed FD-OCT system with 312,500 A-scans/s and an adjustable 2D or volumetric frame rate can be achieved [129]. In comparison, the attainable scan speed of a video rate TD-OCT system is only 4,000 A-scan/s at a frame rate of 32 fps [130]. Furthermore FD-OCT has a greater sensitivity of more than 105 dB [76], a 24 dB improvement over that of TD-OCT [131] due to the decoupling of scanning range and electronic detection bandwidth [72, 79], which enables a greater depth imaging of tissue.

A FD-OCT system is depicted in Figure 3-3. The CCD array records the backscattered light intensity as a function of wavelength. Due to the decoupling of reference mirror scanning and electronic detection bandwidth, FD-OCT enables a significant sensitivity advantage that allows increasing the line rate (A-scan rate) without losing imaging performance [72-76]. The achievable high speed imaging performance allows 3D tissue visualization as well as the measurement of *in vivo* functional tissue properties like perfusion and vessel pulsatility [79]. The maximum achievable imaging depth is limited

to the number of detector pixels in a FD-OCT system [77] but practical limitation like sample turbidity plays an important role in limiting imaging depth, even with the high sensitivity of FD-OCT. The main disadvantage of FD-OCT is the limited imaging depth of about 2 mm in bulk tissues [36, 71] due to strong scattering of light by densely packed scatterers.

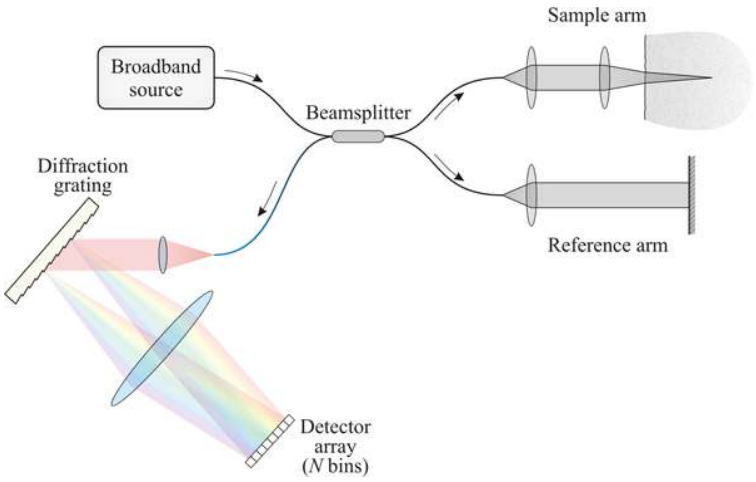

Figure 3-3: Schematic of a FD-OCT system [58].

The interference spectrum obtained from one axial FD-OCT scan of a sample contains all the backscattered spectra of individual interfaces within the sample. The FT of the interference spectrum yields the positions of these interfaces in the spatial domain. Figure 3-4 illustrates the operation of a FD-OCT system. The reference arm mirror is at a fixed position of z_r from the beam splitter and the sample layers are at positions of z_{s_1}, z_{s_2} and z_{s_3} from the beam splitter, respectively. The source light beam is split into two paths at the beam splitter, with the reference arm light wave $\overrightarrow{E_r}$ interfering with back-scattered light waves $\overrightarrow{E_{s_1}}, \overrightarrow{E_{s_2}}, \overrightarrow{E_{s_3}}$ from the three interfaces in the sample. The reference and sample arm light waves interfere at the beam splitter to form $\overrightarrow{E_T}$ and the intensity

interference spectrum is measured by a spectrometer. Unlike the use of a single photodetector in the TD-OCT scheme, the FD-OCT interference spectrum is split into the component wavelengths with a grating and recorded using a CCD array in the spectrometer.

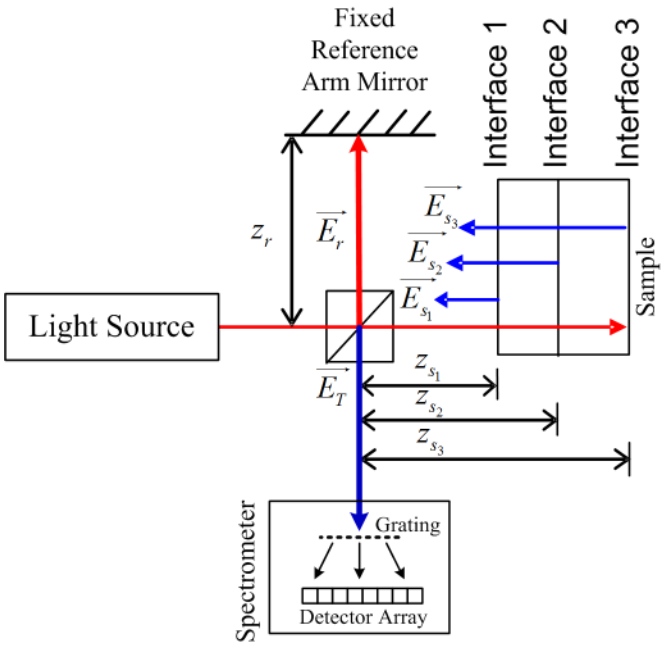

Figure 3-4: FD-OCT setup with a sample comprising three interfaces.

The FD-OCT interference equation is the same as Equation 3.7, except that the interference is evaluated in *k*-space (wavelength domain). The intensity profile $I(k)$ of the interference terms at the spectrometer output can be written as [36]:

$$I(k) \propto \begin{aligned} & S(k)\left[E_r^2(k)+\sum_{n=1}^{N}E_{s_n}^2(k)\right] && \text{“DC Terms”} \\ & +S(k)\left[\sum_{n=1}^{N}E_r(k)E_{s_n}(k)\cos\left(2k\left(z_{s_n}-z_r\right)\right)\right] && \text{“Cross-Correlation Terms”} \\ & +S(k)\left[\sum_{n\neq m=1}^{N}E_{s_n}(k)E_{s_m}(k)\cos\left(2k\left(z_{s_n}-z_{s_m}\right)\right)\right] && \text{“Auto-Correlation Terms”} \end{aligned} \quad \textbf{(3.8)}$$

where S(k) is the power spectrum of the light source, $E_r(k)$ is the reflected reference arm field, $E_{s_n}(k)$ and $E_{s_m}(k)$ are the reflected sample interface fields from different interface layers, z_{s_n}, z_{s_m} and z_r are the spatial positions of the n^{th} and m^{th} sample layer and the reference mirror respectively and N is the total number of interfaces in the sample.

There are three main terms arising from the spectral interferogram, namely the "DC", "cross-correlation" and "auto-correlation" terms. The "DC" components are pathlength independent, and are scaled by the light source wavenumber spectrum with an amplitude proportional to the power reflectivity of the reference arm mirror plus the sum of the sample reflectivities. They are not used in OCT. The "cross-correlation terms" are the desired component for OCT imaging, in which the sample interface positions are identified relative to the reference mirror. The "auto-correlation" terms represent interference occurring between the different sample interfaces, and they typically appear as artifacts in OCT.

The FT of a frequency-domain function $F(f)$ to a time-domain function $f(t)$ is given by [132]:

$$f(t) = \int_{-\infty}^{\infty} F(f) e^{-2\pi ft} df \qquad \textbf{(3.9)}$$

where $e^{-2\pi ft}$ is the FT kernel used to transform functions from one domain to another, f represents frequency and t represents time. To obtain the axial profile, $I(z)$, of the

sample from the spectral profile, $I(k)$, of FD-OCT, FT is performed using a modified kernel obtained from the substitution of factors with the conventional FT kernel [36]:

$$2\pi ft \equiv 2\pi f' t' \tag{3.10}$$

where $f' = \frac{k}{\pi}$ and $t' = z$. The axial profile $I(z)$ can be written as:

$$I(z) = \mathrm{Re} \int_{-\infty}^{\infty} I(k)\, e^{-2\pi\left(\frac{k}{\pi}\right)z}\, dk \tag{3.11}$$

Figure 3-5a shows the results of a simulation performed for a SLD light source spectra with center wavelength at 840 nm and a bandwidth of 40 nm. The sample has three interfaces similar to that shown in Figure 3-4 and their axial distance with respect to the reference mirror positioned at z = 0 mm are 0.1 mm, 0.3 mm and 0.6 mm, respectively. The interference spectrum from each interface overlaid on the source spectrum is shown in Figure 3-5b-d and Figure 3-5e-g depicts the individual interference spectrum with the source spectrum removed. It can be observed that as an interface position in the sample with respect to the reference mirror increases, the frequency of the interference fringe also increases. The actual interference spectra observed by the spectrometer (Figure 3-5h) is given by the sum of the interference spectrum arising from each interface in the sample. The subsequent conversion of the interference spectrum to axial distance (Equation 3.11) is essential for depth representations of FD-OCT signals and the measured interference spectrum has to be converted to *k*-space (wavenumber domain) before FT (Equation 3.8). Since $k = \frac{2\pi}{\lambda}$ and the data is linearly-spaced in the wavelength domain, conversion to *k*-space results in a data set that is non-linearly spaced.

To obtain the axial positions of the sample interfaces, a FT is applied to the interference spectrum of Figure 3-5h after conversion to *k*-space values. This reveals the axial profile in the sample, as shown in Figure 3-5j. The zero order component originates from the FT of the "DC terms" in Equation 3.8 . In actual practice, the source spectrum is removed as shown in Figure 3-5i to minimize the zero order component in the spatial domain. It is difficult to completely remove the source spectrum, thus there is usually a residual zero order component. Depending on the number of lateral scan points, each 2D OCT lateral scan contains many such axial scans. A 2D cross-sectional image of the sample is obtained from combining these axial profiles together. The 2D cross-section is typically depicted as a grayscale or false color image where each pixel in the image represents the intensity value at a location in the sample.

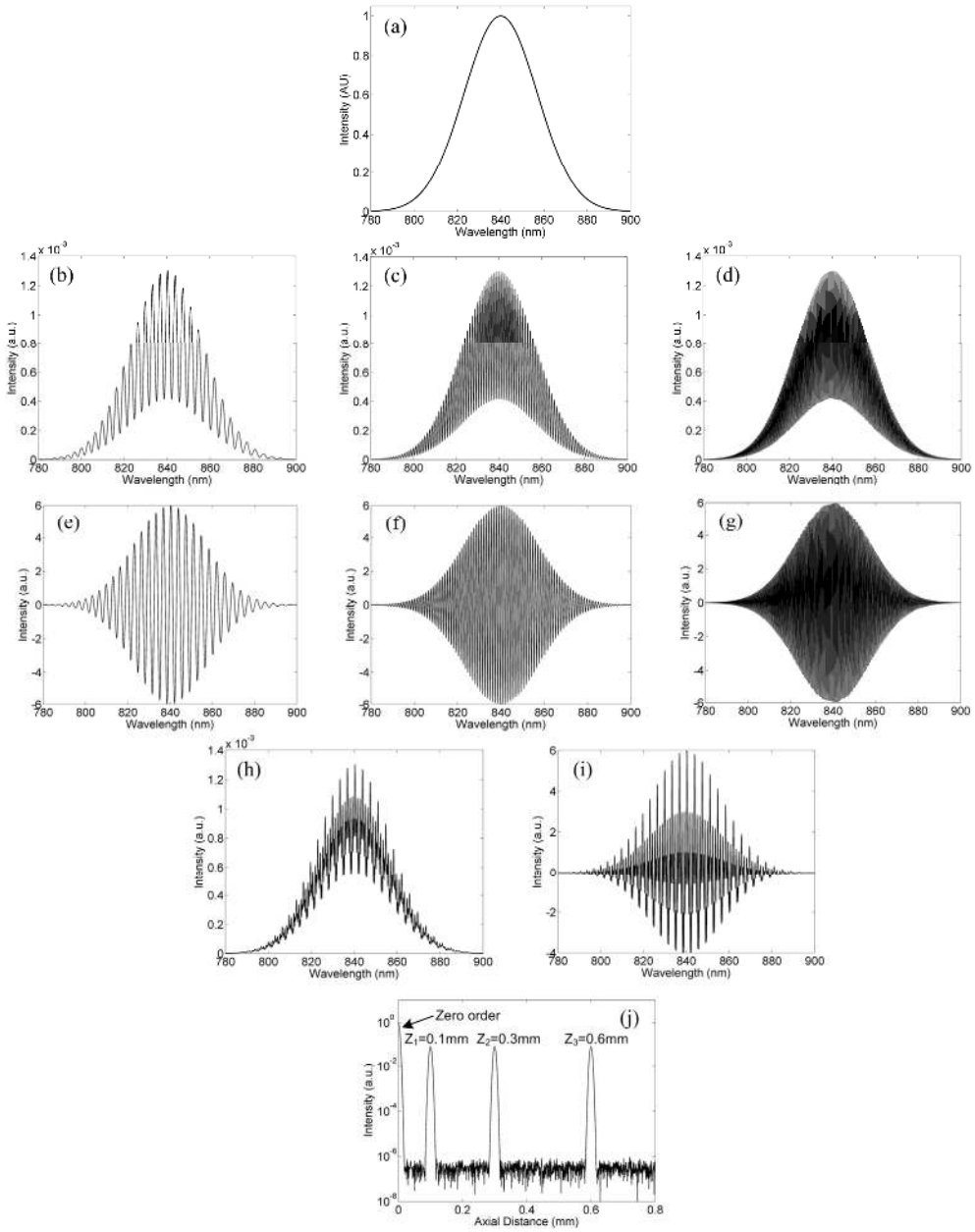

Figure 3-5: Simulation of (a) light source spectrum with center wavelength of 840 nm and a bandwidth of 40 nm. (b)-(d) Spectral fringes of 3 interfaces in a simulated sample located at positions of 0.1, 0.3 and 0.6 mm with respect to the reference mirror. (e)-(f) Spectral fringes with light source spectrum removed. (h) Sum of all interference spectra and the light source spectrum. (i) Sum of all interference spectra with the light source spectrum removed. (j) Axial profile of the three interfaces after FT from (h).

3.4 OCT System Parameters

3.4.1 Axial Resolution

The axial resolution in an OCT system is independent of system optics but is dependent on the coherence length of the light source. The coherence length l_c of a light source is defined as the distance at which the electromagnetic wave can travel while still maintaining phase periodicity, and is given by [127]:

$$l_c = c \cdot t_c \tag{3.12}$$

where c is the speed of light and the coherence time t_c is defined as:

$$t_c = \frac{\lambda^2}{c \cdot \Delta\lambda} \tag{3.13}$$

Here λ is the center wavelength and $\Delta\lambda$ is the bandwidth of the light source. Equations 3.13 and 3.14 can be combined to give:

$$l_c = \frac{\lambda^2}{\Delta\lambda} \tag{3.14}$$

Since light sources in OCT can be generally treated as Gaussian in nature, the axial resolution of an OCT system Δz is commonly represented by the coherence length of a Gaussian light source [35]:

$$\Delta z = \frac{2\ln 2}{\pi}\frac{\lambda^2}{\Delta\lambda} \tag{3.15}$$

Δz is the FWHM value of the temporal degree of coherence, in this case represented by the PSF of the OCT system in spatial domain, an example is shown in Figure 3-5j. In order to achieve high axial resolution, interference should occur over as short a distance as possible. Optical light sources with short coherence lengths are those with large

bandwidths, as indicated in Equation 3.15. Hence a low coherence light source like a SLD will achieve higher axial resolution than a high coherence source like a laser.

The relation between the axial resolution and the coherence length of the light source is illustrated in Figure 3-6, where the back-reflected light from a single sample interface is interfered with light from a scanning reference path in a TD-OCT setup (Figure 3-6a). Interference is observed when the path lengths are matched to within the coherence length of the light source. With a high coherence laser source, interference is observed over a large distance and the sample interface cannot be discerned, as shown in Figure 3-6b. By contrast, the use of a low coherence light source only produces interference over a short distance which clearly reveals the position of the sample interface when the interference is demodulated (Figure 3-6c).

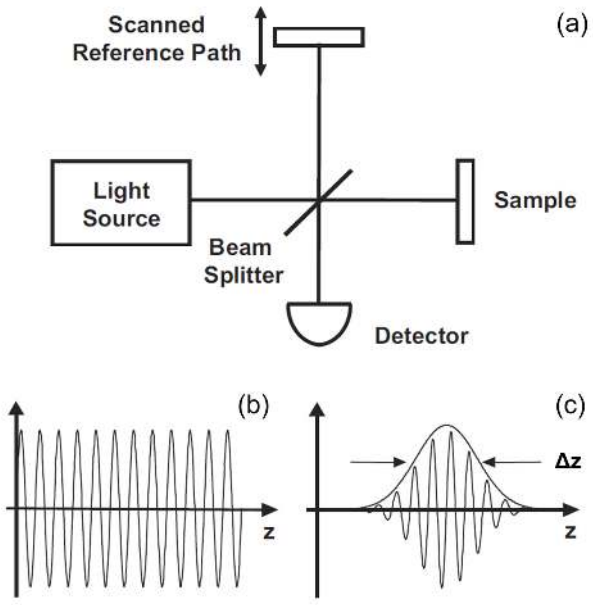

Figure 3-6: Illustration of a (a) TD-OCT setup, and of the relation between the axial resolution and the coherence length of the light source [133] in OCT, with (b) Poor axial resolution with a long coherence length light source, and (c) Better axial resolution with a short coherence length light source.

The maximum axial measurement range, z_{max}, of an FD-OCT system is related to the axial resolution Δz by the following [77]:

$$z_{\max} = \frac{\Delta z}{2} \cdot \frac{N}{2} \tag{3.16}$$

Where N is the number of pixels in the spectrometer. N is divided by two because the Fourier transform of the real spectrum has conjugate symmetry about the zero delay. The pixel spacing is chosen as $\Delta z/2$ according to Nyquist condition. This equation demonstrates that for a given light source bandwidth, the maximum axial depth is determined by the number of detector pixels in the spectrometer.

Figure 3-7 compares the axial resolution of different bandwidth light sources, with center wavelengths of 800, 1,000 and 1,300 nm [36] within the tissue optical window (Section 2.4), computed with Equation 3.15. The axial resolution improves tremendously with a shorter center wavelength and a broad bandwidth light source. However, while the use of a shorter center wavelength light source ensures better resolution, it comes with the compromise of a poorer penetration depth in tissues due to attenuation and scattering. On the other hand, a longer wavelength light penetrates deeper into tissues but gives a poorer axial resolution. In practice the center wavelength of the OCT light source is chosen to optimize both axial resolution and penetration depth.

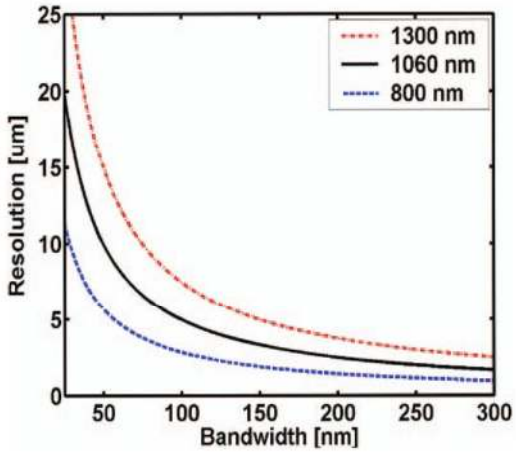

Figure 3-7: Calculated axial resolution versus bandwidth of light sources with center wavelengths of 800, 1,000 and 1,300 nm [36].

3.4.2 Lateral Resolution

The lateral resolution Δx in an OCT system is dependent on the objective lens used and is calculated using [127]:

$$\Delta x = \frac{1.22 f \lambda}{D} = \frac{0.61 \lambda}{\mathrm{NA}} \tag{3.17}$$

where f is the focal length of the lens, λ is the center wavelength of the light source, D is the diameter of lens and NA is the numerical aperture of the lens. NA is given by $n \sin\theta$, where n is the refractive index of the imaging medium or sample and θ is the aperture angle [134]. The lateral resolution of a lens is proportional to its depth of field or the confocal parameter. The confocal parameter refers to the length of the region in the propagation direction within the focused light beam where the cross sectional area of the beam is less than twice the beam waist area. The confocal parameter is twice the Rayleigh range of a Gaussian beam, which is defined as the distance along the propagation of the beam from the beam waist to the point where the cross sectional area is doubled. At this the point, the intensity of the light beam is halved [127]. Most OCT

imaging is performed with low NA focusing where the confocal parameter is much longer than the coherence length. This is done so that most of the energy of the beam is spread deeper into tissue for greater imaging depth. Consequently there is a trade-off between lateral resolution and depth of field.

3.5 Spectroscopic OCT (SOCT)

Standard intensity-based OCT systems represent information about tissue backscattering as a grayscale or false color image. In these systems, the intensity of the backscattered light at each pixel in the image is stored only as a single value. In SOCT, there are in general five steps to the spectroscopic analysis process. While there are other variants reported in literature [38-39, 68, 115-116], the process described here is the preferred approach in this work. The TD-SOCT method is described in greater detail here as it is more intuitive (Figure 3-8). (1) A window is first applied to the full interferometric signal in the axial profile, instead of applying only to the intensity values, to extract depth dependent data. (2) It is possible to calculate a local scattering spectrum for every pixel in the image using time-frequency transform (TFT) such as the short time Fourier transform (STFT) [115]. The STFT is the most basic time-frequency function that can be used for the processing of depth-dependent wavelength scattering in SOCT. The disadvantage of STFT is the tradeoff between spatial and spectral resolution: good resolution in one domain is achieved at the expense of the other [135]. By generating a local scattering spectrum for every axial point in an OCT image, a 4-dimensional (4D) data set is produced. The 4D data set is defined by the transverse and axial coordinates, as well as the wavelength and intensity of the locally scattered light. For ease of interpretation of

such a spectroscopic data set, it is necessary to condense the data to 3D for image display. (3) In order to quantify the local scattering spectrum, an autocorrelation is performed. The spectral modulation present in the local scattering spectrum is considered to be an outcome of a stochastic process, in which the properties of the process are determined by the distribution of sizes and refractive indices of the cellular organelles contained within the imaging volume, as well as the number density of the organelles [115]. The autocorrelation of the local spectra take on distinct shapes as the spectral modulation changes. (4) A metric is needed to quantify the spectral modulation in the local spectrum, which then can be stored as a single value in a spectroscopic map. A commonly used metric is the bandwidth of the autocorrelation function, among others. (5) The spectroscopic map and the intensity OCT image can be combined in a Hue/Saturation/Luminance (HSL) color map with the spectroscopic values mapped to hue in the HSL image and the intensity values mapped to saturation and luminance [115]. In literature, another method for representing spectroscopic data in true-color OCT images has recently been reported [136], where local spectral data is analyzed quantatively and used to assign red, green and blue channels for true-color representation of the samples. In this way, the 4D dataset can be visualized as a 2D structural image with color in the third dimension representing scatterer sizes in the OCT scan. The flowchart of the spectroscopic analysis process is shown in Figure 3-9.

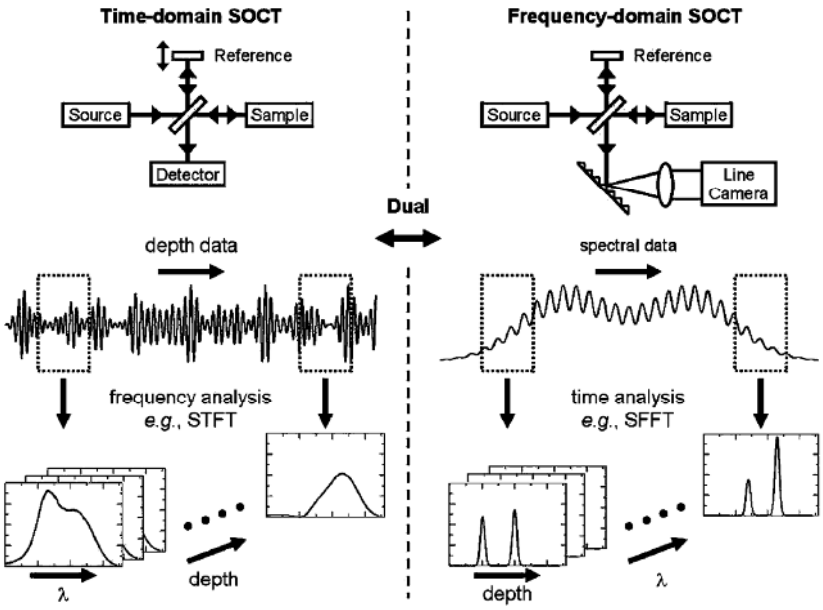

Figure 3-8: SOCT imaging using time domain (left) or frequency domain (right) interferometry. Short time and short frequency FTs are performed on the OCT interferograms to create 2D OCT signals indexed by wavelength and depth respectively in the object [38].

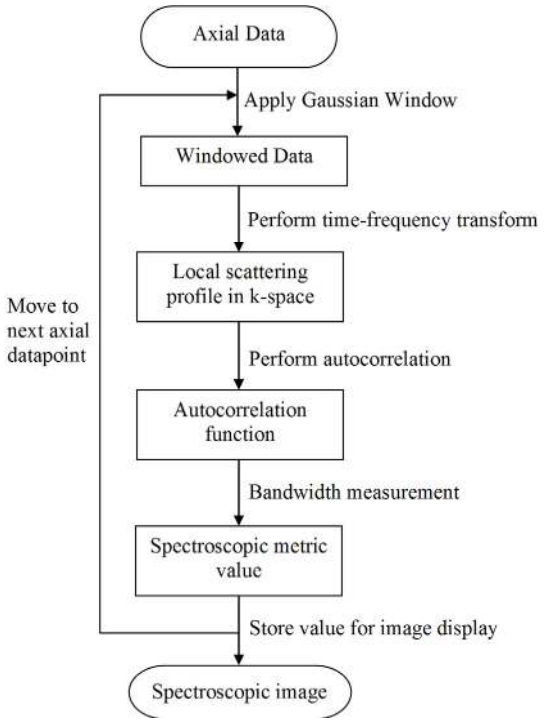

Figure 3-9: Flowchart of spectroscopic analysis process.

The spectroscopic resolution, describing the ability to differentiate scatterer sizes, in a SOCT image is affected by 3 main factors, namely the light source bandwidth, the time-frequency transform used and the choice of spectroscopic metric. A broad bandwidth light source increases the ability of the SOCT system to record low frequency spectral modulations indicative of small particles, thus effectively increasing the spectroscopic resolution [38]. In instances where a non-broadband spectral bandwidth source is used in the OCT system, the spectral resolution of the source spectrum and the detectivity of low frequency spectral modulations can become limited.

3.5.1 Time-Frequency Transformations

Spectroscopic analysis is typically performed in a depth resolved manner by using a windowed time-frequency transform [38, 116, 137-138] like the STFT to form a time-frequency distribution (TFD) of an OCT axial scan. The first time-domain based STFT for spectroscopic OCT analysis was introduced by Morgner [114]. In FD-OCT, spectral data is windowed and transformed using a short frequency Fourier transform (SFFT) to obtain local depth data. The first frequency-domain based SFFT for spectroscopic OCT analysis was implemented by Leitgeb [139]. Both methods are interchangeable, as long as transformed data are retained in the complex form (Figure 3-8) [38]. The TD-OCT method of spectroscopic analysis is more intuitive and this method can be used for FD-OCT data after transformation from spectral to spatial domain.

To avoid undesired artifacts in the spectral response arising from a window with abrupt cut-offs, e.g. rectangular window, a smooth envelope function such as a Gaussian or

Hamming window is typically chosen for h in a STFT transformation of the axial information described by Equation 3.11 [38] and is shown as follows:

$$STFT\left\{\overrightarrow{I(z)}\right\} \equiv I(k, z_0) = \int_{-\infty}^{\infty} \overrightarrow{I(z)} \cdot h(z - z_0) \cdot e^{-j2\pi\left(\frac{k}{\pi}\right)z} dz \qquad \textbf{(3.18)}$$

where $h(z - z_0)$ is an arbitrary window function centered at spatial position z_0. The complex values of $\overrightarrow{I(z)}$ are retained after FT from the spectral data.

STFT is the most basic time-frequency function that can be used for the processing of depth-dependent wavelength scattering in SOCT. The disadvantage of STFT is the tradeoff between spatial and spectral resolution: good resolution in one domain is achieved at the expense of the other. To overcome these limitations, the dual window (DW) TFT technique utilizes two STFT operations such that the standard deviation of the primary window is chosen to be much smaller than the secondary window ($\sigma_{PW} << \sigma_{SW}$) to obtain excellent spatial and spectral resolution. The spectral and spatial resolutions are defined independently by the width of the primary and secondary windows, respectively. The effectiveness of the DW TFT over linear TFTs like STFT and bilinear TFTs like WVD is well documented in the literature [116-117].

The DW function in k-space is defined as [117]:

$$\begin{aligned} DW(k) = &\sum_{z=-\infty}^{\infty} 2E_r(z)\langle E_s(z)\rangle \cos(2nz_{pw}) \exp\left[\frac{(z_{pw} - z)^2}{2\sigma_{pw}^2}\right] \exp(-jz_{pw}k) \\ &\times \sum_{z=-\infty}^{\infty} 2E_r(z)\langle E_s(z)\rangle \cos(2nz_{sw}) \exp\left[\frac{(z_{sw} - z)^2}{2\sigma_{sw}^2}\right] \exp(-jz_{sw}k) \end{aligned} \qquad \textbf{(3.19)}$$

where z_{pw} is the position of the center of the primary window with a standard deviation of σ_{pw}, z_{sw} is the position of the center of the secondary window with a standard deviation of σ_{sw}, and $\langle E_s(z) \rangle$ represents the sum of E-fields from all sample interfaces. The local spectral modulation $DW(k)$ contains modulations of varying frequencies which must be analyzed to obtain the frequency spread.

3.5.2 Autocorrelation Function

The analysis of the local spectral modulations is important as scatterer size information is determined from the analysis. Contrast enhancement of OCT images based on properties in addition to the intensity of the backscattered light was first demonstrated by Morgner *et al.* [114]. Spectral modulation at each axial point was first obtained by applying the Morlet wavelet transform (MWT) on the OCT axial scan. The centroid wavelength of the MWT spectrum at each axial point was utilized to form a spectroscopic metric. The spectroscopic metric and the backscattered OCT intensity are then mapped to the red-green hue and saturation to form a spectroscopic false-color image. It was demonstrated that features which are difficult to identify in conventional intensity-based OCT image become visible in the spectroscopic image [114]. Spectroscopic metrics for describing particle sizes can also be derived from Fourier-domain low-coherence interferometry (fLCI). A correlation method involving the FT of local spectral modulations was used and the peak in the correlation function in spatial domain indicates the average cell nuclear diameter in the region of analysis [39, 67-69, 116-117]. In the work of Robles and Wax [68], a two layer phantom containing polystyrene beads of diameters 4 and 6.98 μm were imaged and analyzed using the DW method for time-frequency transformation

and subsequently LSS and fLCI were used to analyze the spectral information from localized regions in the phantom sample to determine scatterer sizes accurately. Though quite accurate in determining scatterer size, this method suffers from poor peak visibility when there are limited modulations across the light source spectrum [38]. Spectral modulation autocorrelation function has also been used in SOCT imaging as it is insensitive to Doppler shifts as well as dispersion [38, 115]. Oldenburg [38] and Adler [115] proposed the autocorrelation width of the depth-dependent spectral modulation function at 80% and 90% of the peak autocorrelation values, respectively, as suitable spectroscopic metrics. In the work of Adler *et al.* [115], microsphere particles of various sizes were characterized by measuring the associated spectral modulation in the OCT signal. With this information, the color codes obtained from the spectroscopic images of biological samples were correlated to spectral modulation with an inference to particles sizes. Using this approach, Oldenburg [38] and Liang [118] presented spectroscopic images of fibroblasts and macrophages in a tissue scaffold. The color coding of the cells in the spectroscopic images, representing autocorrelation bandwidth extracted from spectral modulation in the OCT signals, gave information of cellular size relative to each other. The autocorrelation method is thus an effective way to analyze the spectral content of local spectral modulations for the dominance of certain spectral frequencies corresponding to specific scatterer sizes. This is performed by autocorrelating the local spectral modulations to obtain the autocorrelation function.

The autocorrelation function gives a measure of the resemblance of a signal to itself when shifted by a certain amount. The autocorrelation function is described by [115]:

$$R_{xx}[m] = \sum_{k=0}^{\infty} \left| DW[k] \right| \left| DW[k-m] \right| \quad \textbf{(3.20)}$$

where $DW[k]$ is the local scattering spectra and m is the amount of shift (lag). Tissue regions containing smaller particles produce less spectral modulation, while regions containing larger particles produce more modulation [115]. The number density of the scattering particles also affects the modulation pattern. Tissue regions with a higher particle density and a wider distribution of sizes produce spectra with more modulation compared to regions with low particle density and a narrower distribution of sizes. The autocorrelation of the local spectrum takes on distinct shape as the spectral modulation pattern changes. Small amplitude, low frequency modulations corresponding to areas with largely small particles produce an autocorrelation shape that falls off slowly around m = 0, with few secondary peaks. Conversely large amplitude, high frequency modulations corresponding to areas with mainly large particles produce an autocorrelation shape that falls off rapidly around m = 0, with many secondary peaks. The bandwidth of the autocorrelation function can be used to provide information about the distribution of scatterer sizes based on the spectral modulation at each point in the SOCT image. The bandwidth value serves as a spectroscopic metric that can be encoded into a HSL color map to represent scatterer size distribution in a sample.

Chapter 4 Biomechanical Characterization of Flexor Tendons with FD-OCT

4.1 Introduction

Flexor tendons in the hand function as a strong and flexible connection between the forearm muscles and the fingers bones. The major constituent of tendons is type I collagen [140], the most abundant protein in the human body [77], and morphologically the tendon is a complex composite material consisting of collagen fibrils embedded in a matrix of proteoglycans. Fibroblasts, the predominant cell type within tendons, are arranged in the spaces between the parallel collagen bundles and are readily observed in histology images as dark rod like structures. When the forearm muscle contracts, the tendon pulls on the finger bones and cause the fingers to bend. The hands are the most frequently used part of the body and flexor tendons are prone to many injuries as they run along the palm side of the hand and are situated near the skin at finger joints [141]. Some common injuries include tendon rupture which can be caused by overloading the finger (e.g. in rock climbing), lacerations from sharp force trauma, crushed tendon due to blunt force trauma and inflammation due to infection.

The current gold standard for the evaluation of injured tendons is a visual examination by a hand surgeon, who will determine the best way to treat the injury. Surgery is usually needed to suture severed tendons back together, as they cannot heal unless the cut ends of the tendons are touching. During the healing process, fibroblasts use raw materials in the surrounding matrix to rebuild the collagenous structures within the tendon. Scar tissue called adhesions may form at the suture site which prevents the smooth gliding of the flexor tendon in the tendon sheath [40]. As a result, the sutured site has to be operated

again to remove the scar tissue. Ultrasonic and MRI imaging techniques can non-invasively monitor healing tendons [16], and they have the advantages of using non-ionizing radiation to probe connective tissues. Ultrasound, though cheap to implement and has good resolution at >150 μm when using high-frequency transducers (40 – 60 MHz) [3, 8], it requires contact with the sample and cannot image through air. While conventional MRI is suitable for whole body imaging, it has poorer resolution (>1 mm) [1, 3], is expensive to use and is not suitable for people with metal implants due to the high magnetic fields employed in the technique. Human flexor tendons (flexor digitorum profundus) are typically 7 mm wide [142] and a higher resolution, depth resolved imaging technique would be required to image them. OCT can potentially fill the need for a robust and high resolution method of imaging the cross-sections of flexor tendons. In particular, OCT imaging of normal and repaired tendons under different loading conditions can provide information that is currently not available to surgeons, allowing them to monitor the state of the tendon repair site during and post- surgery.

The development of a FD-OCT system for characterizing the biomechanical properties of flexor tendons and facilitating the other tissue analysis work carried out in the rest of the thesis is reported in this chapter. The design requirements and the choice of components for the FD-OCT setup are first described. The implementation and characterization of the system are presented and discussed. The FD-OCT system is then used to image normal and repaired flexor tendons under load. The OCT images of normal tendons were first compared and correlated to the corresponding histological images. Biomechanical

characterization of both normal and repaired tendons with the FD-OCT system was carried out by loading the samples with weights of up to 1 kg.

4.2 Materials and Methods

4.2.1 FD-OCT System

4.2.1.1 Design Consideration

Several design parameters of the OCT system have to be considered. Firstly, the axial resolution of the system should be capable of resolving the various tissue microstructures investigated in this work. Normal oral epithelial cells measure on average 7 μm in size and can swell to larger than 10 μm upon cancerous transformation [28-31, 120]. In flexor tendons, the dimensions of collagen crimp patterns are in the order of 50 μm [143-145]. Cell fibroblasts that aggregate at tendon injury sites typically measure about 50 μm in diameter, though when adhered to a surface the thickness of the cell can be reduced to 10–15 μm [38]. In tissue engineering applications, fibroblast cells with sizes similar to those observed in tendons are seeded in tissue scaffolds used for connective tissue reconstruction [80, 118, 146-148]. The axial and lateral resolutions of the OCT system in tissues should therefore be at least 7 μm so that these tissue microstructures can be differentiated.

Secondly, imaging depth plays an important role in tissue imaging as it determines how much subsurface tissue structures can be monitored. Tissue scattering is one of the main factors limiting imaging depth [71, 84-86, 149]. Epithelial tissue up to the basement membrane is considered to be important [33, 89, 92, 117] as most early carcinogenic

changes can be detected when monitoring the basement membrane. The thickness of epithelial layer has been found to increase when cancerous changes occur [33]. Besides changes in epithelial thickness cancer, cells may also destroy the basement membrane, blurring the distinct boundary between the epithelium and lamina propria layers. An imaging depth of at least 1 mm in tissue will be necessary to observe such details. In the case of injured tendons, monitoring of the healing process at the injury site involves observing the proliferation of fibroblast cells. The tendon injury site can be highly scattering due to a high concentration of growth cells, ultimately limiting the imaging depth. The achievable imaging depth for this application is not known due to a lack of OCT data on fibroblast growth cells. In tissue scaffolds, the scaffold material and pockets of seeded cells limits the imaging depth [148]. Imaging depths for blank and seeded scaffold was reported to be 1.2 mm and 0.8 mm respectively, using a 1300 nm TD-OCT system [148]. A large confocal parameter of the objective lens in an OCT system can be selected to increase the imaging depth using a lens with small NA (Section 3.4.2). A confocal parameter of at least 1 mm will be suitable for achieving the necessary imaging depths in the tissues investigated in this thesis.

The choice of the OCT wavelength can also impact the imaging depth. The sample OCT beam is attenuated by scattering and absorption when propagating in and out of the tissue. Such attenuation can be reduced through the use of long wavelength light [150] due to the reduced absorption of primary tissue absorbers like melanin and haemoglobin (Section 2.4). On the other hand, using a long wavelength light will degrade the axial resolution (refer to Equation 3.15). A good compromise between axial resolution and

imaging depth is achieved by selecting an OCT wavelength of 840 nm. This OCT wavelength enables a good size differentiation of individual scatterer moderately deep in tissues through SOCT analysis [115].

The lateral scan distance is subjected to the size of the tissue or samples scanned. For human epithelial tissue [71, 84], in order to observe tissue structures in detail, a scan range of 4–6 mm is sufficient. A larger area than a traditional excisional biopsy (about 1–2 mm) can be visualized in this case. The monitoring of ruptured tendons [113] requires a large section of the tendon to be scanned (about 4 mm) as the rupture can occur over a large area. In addition, human tendons are generally larger than those found in common laboratory animals like mice, rats and rabbits. In the monitoring of cell seeded tissue scaffolds, a scan range of > 5 mm [148] allows for details of scaffold architecture to be observed and studied when studying the proliferation of cells after seeding. Thus, the system lateral scan distance should achieve at least 6 mm.

Over a long lateral scan distance, the flatness of the scan field may vary. Ideally a flat scan field is desired so that the OCT image accurately reflects the sample morphology and not become distorted at the image edges due to spherical aberration of the objective lens. The SNR of the OCT system is also important as the sensitivity of the system can impact the imaging depth [76]. A SNR of up to 105 dB can be achieved in a FD-OCT system [76]. With SNR greater than 100 dB, sample penetration depth of 2–3 mm is possible in most scattering tissues [150]. FD-OCT imaging speeds of up to 312,500 axial scans/s has been reported [129] in the literature where an ultrahigh speed FD-OCT

system is used for retinal imaging. Real time imaging is not needed due to the *ex vivo* nature of OCT imaging performed in this thesis, where the tissue samples are imaged in an external environment with no immediate need to expedite imaging (like during surgical procedures or during eye imaging where the blink reflex of the patient requires imaging to be fast [151]). In addition, biological processes like healing and cell proliferation that are monitored in this work do not occur in a short time. A scan speed of about 50 axial scans/s is sufficient to ensure that imaging is done in a timely manner without changes to the sample when exposed to external environmental conditions.

4.2.1.2 Instrumentation

The FD-OCT system implementation shown in Figure 4-1 utilizes a Michelson interferometric setup similar to the fiber-optic FD-OCT system first reported in [78]. The primary light source used is a superluminescent diode (SLD) from Superlum with a center wavelength of 840 nm and an optical bandwidth of 36 nm. The SLD source has an output power of 7 mW and the optical power incident on the sample is measured to be about 2 mW. The choice of a broader optical bandwidth as compared to [78] results in an improved axial resolution. The light source spectrum and bandwidth determines the point spread function (PSF) of the probe beam and thus the axial resolution of the system [126], as shown by Equation 3.15. System dispersion due to unbalanced reference and sample arms causes broadening of the PSF and this leads to a reduction in the axial resolution. The lateral resolution of the system is related to the center wavelength of the light source as well as the numerical aperture (NA) of the objective lens used, as shown by Equation 3.17. A long focal length objective lens at 100 mm with a small NA was

chosen due to a compromise between a larger lateral spot size and better confocal range to improve imaging depth, to compensate for the choice of a shorter light source center wavelength. The choice of the center wavelength of 840 nm as compared to a less scattered 1300 nm wavelength is made based on the need for better axial and lateral resolution over imaging depth, especially for the spectroscopic analysis of the OCT data performed in the subsequent chapters. The light source selected also has a higher output power, allowing an increased power at focus than in [78]. The spectrometer used has a CCD detector count of 3,648 over the wavelength range of 707.23 – 911.67 nm, resulting in a wavelength resolution of 0.05 nm. The signal processing time depends on the speed of data transfer from the detector in the OCT system. In ultrahigh speed FD-OCT systems, a custom build spectrometer with a line-scan CCD camera (e.g. Basler Sprint) with a data transfer rate of 140 kHz [129] is commonly used. This enables very high axial scan rates of 312,500 axial scans/s, >300 fps for a 1,000 lateral point OCT image, when suitable software is used for data processing.

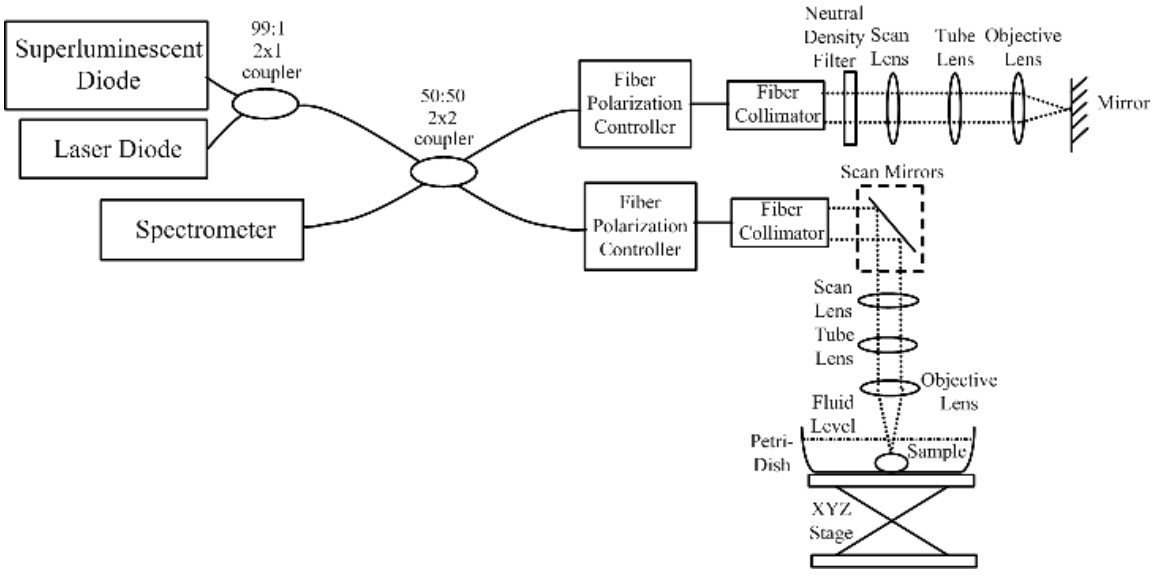

Figure 4-1: FD-OCT system setup.

A 635 nm laser diode is coupled into the light path through a 99:1 coupler to provide a visible guide beam spot on the sample. A 50:50 splitting ratio 2×2 coupler is used to split the incoming light into the reference and sample arms. Fiber polarization controllers (FPC) are used in both the reference and sample arms to adjust the polarization state of light. Interference will only occur when the polarization components of the reference and sample arms are matched [35]. A mismatch in the polarization states will result in a loss of interference fringe contrast, but polarization adjustment can be made by tuning the FPCs. In the reference arm, light is collimated with a fiber collimator and attenuated with a neutral density (ND) filter to avoid saturating the spectrometer. This will also allow the SNR to be improved by increasing the integration time of the spectrometer.

The tube lens and scan lens of 62.9 mm and 100 mm focal lengths, respectively, in the reference arm are used to ensure that the light is always positioned on the back aperture of the objective lens (45 mm fl). This optical arrangement of the tube and scan lens,

known as a telescopic arrangement commonly used in scanning microscopes [152], has two distinct properties. Firstly, the ratio of the focal length of the tube lens to the scan lens gives a magnification of the beam spot size. Here, the beam spot is increased by 1.6 times to fill the back aperture of the objective lens for better lateral resolution. Secondly, when the light beam in the sample arm is laterally scanning across the back aperture of the scan lens by the scan mirrors, this motion is converted to an angle scan of the collimated beam at the focal point of the tube lens. The objective lens is placed at the tube lens focal point to focus the collimated beam to a spot which scans laterally across the sample. The scan and tube lenses are identical in the reference and sample arms to ensure that the dispersion effects in the two arms are matched so as to prevent broadening of the PSF which leads to poorer axial resolution.

In the sample arm, a GSI Lumonics scanning galvanometer comprising VM1000 scan mirrors and SC2000 scan controller is used to raster-scan the optical beam on the sample. The objective lens used in the sample arm is a 100 mm focal length plano-convex lens. This focal length is chosen to achieve the desired confocal parameter. All lenses used in the system are achromat doublets to ensure that chromatic aberration is minimized. This is important due to the broadband nature of the light source used in the OCT system. The spectral interference signal of the returning light from both arms is collected by an Ocean Optics HR4000 spectrometer and subsequently processed by a computer.

The sample position is controlled by a XYZ stage. The Z stage is manually adjusted for sample focusing while the XY stages are used for coarse sample positioning prior to

automated scanning by the galvanometer. The samples are placed in a petri-dish with fluid to maintain hydration throughout the imaging period. This configuration is used for most tissue samples measured in this thesis, e.g. excised epithelial tissue, rest-state flexor tendons and tissue scaffolds. For flexor tendon imaging during stress loading, a modified sample holder illustrated in Figure 4-2 is used to secure and load the tendon whilst allowing a section of the tendon to be imaged by OCT.

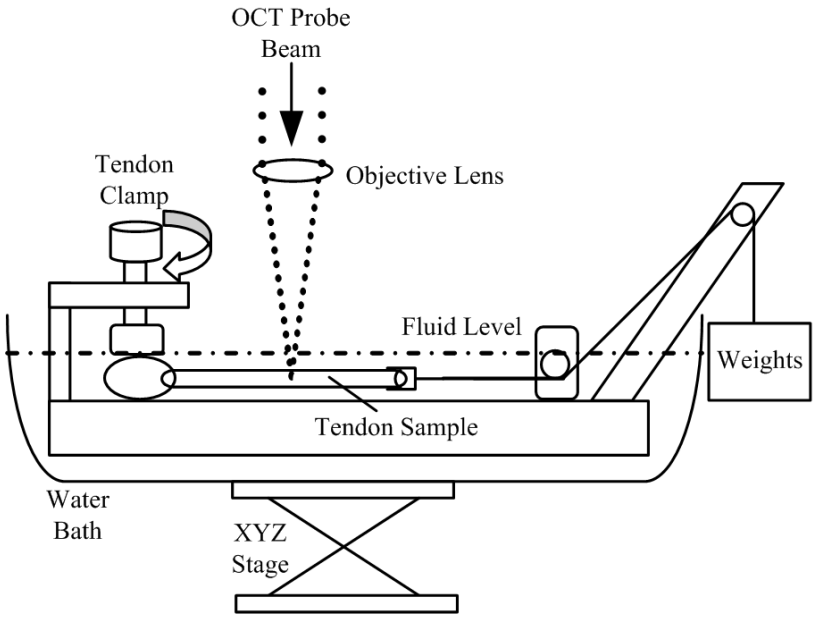

Figure 4-2: Mounting jig used to mechanically load flexor tendon for OCT imaging.

The measured spectrum of the light source, $I(\lambda)$, shown in Figure 4-3a is a set of 3,648 discrete data points corresponding to the intensity value at each pixel in the detector array. Figure 4-3b shows the interference spectrum of an OCT scan of a mirror. The interference fringes arising from the mirror are superimposed onto the measured source spectrum. The conversion of interference spectrum to axial distance (Equation 3.11) is

essential for depth representations of FD-OCT signals and the measured interference spectrum has to be converted to *k*-space (wavenumber domain) before FT (Equation 3.8). Since $k = \frac{2\pi}{\lambda}$ and the data is linearly-spaced in the wavelength domain, conversion to *k*-space results in a data set that is non-linearly spaced. Therefore linear interpolation has to be performed on zero padded wavelength data [153] to obtain linearly-spaced data in *k*-space (Figure 4-3c).

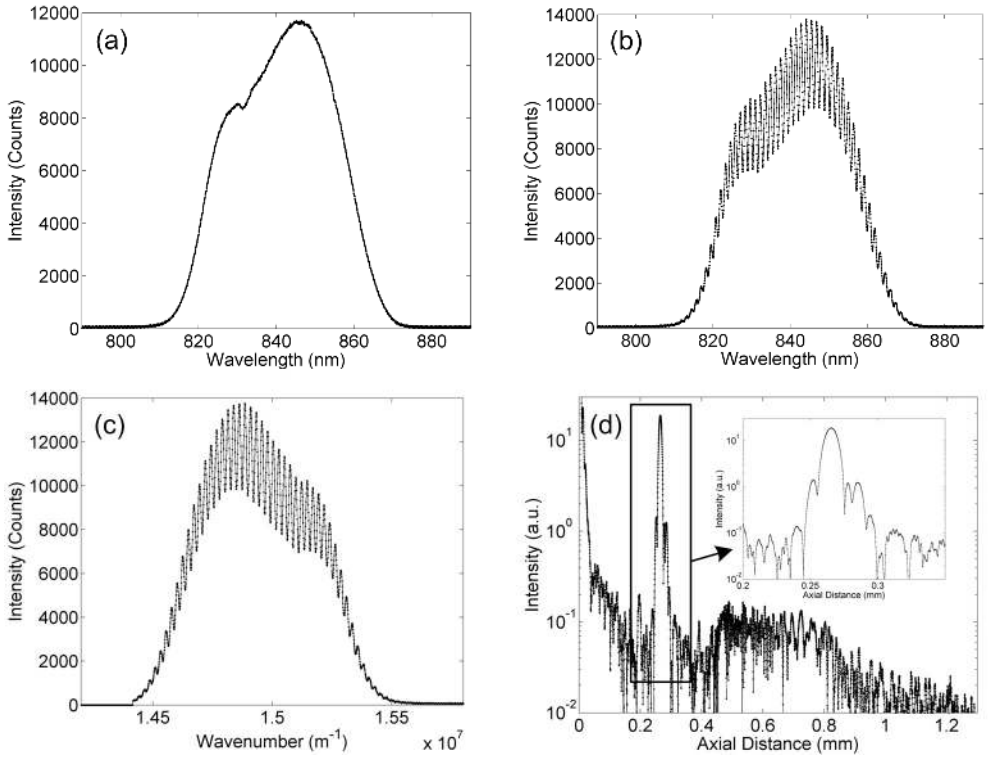

Figure 4-3: (a) Measured SLD source spectrum. (b) Measured OCT interference spectrum from a mirror scan in wavelength domain. (c) Measured OCT interference spectrum in *k*-space. (d) PSF from FT of the measured interference spectrum of a mirror. Inset: Expanded view of PSF.

The maximum achievable axial depth z_{max} is calculated from:

$$z_{\max} = \frac{\pi}{\Delta k} \tag{4.1}$$

where $\Delta k = \frac{2\left(k_{\max} - k_{\min}\right)}{N_{\det}}$ is the normalized k-space step size, $k_{\min} = \frac{2\pi}{\lambda_{\max}}$, $k_{\max} = \frac{2\pi}{\lambda_{\min}}$ and $N_{\det}$ is the number of pixels in the detector array of the spectrometer. Using the values of the parameters shown in Table 4-1, the value of $z_{\max}$ is calculated to be 3.225 mm.

Table 4-1: Calculated spectrometer parameters

Parameter	Value
λ_{min}	707.23 nm
λ_{max}	911.67 nm
k_{min}	17.77×10^6 m^{-1}
k_{max}	13.78×10^6 m^{-1}
N_{det}	4,096
Δk	974.121 m^{-1}

Zero-padding is applied to the k-space interference spectrum before FT to increase the sampling density in the spatial domain [79] since the total available axial data points is halved after FT. If the total zero-padded array has N data points, the resulting spatial step size is given by:

$$\Delta z = \frac{z_{\max}}{\left(\frac{N}{2}\right)} = \frac{\pi}{\Delta k} \cdot \frac{2}{N} \tag{4.2}$$

N is chosen to be $2^{15} = 32,768$ and the corresponding spatial step size is found to be $\Delta z = 0.197$ μm. This is about 50 times the 10 μm axial resolution of the system which provides a good spatial sampling resolution as well as positional sensitivity of < 1 μm

[154]. The zero-padded *k*-space interference spectrum is then FT to give the spatial position of the mirror (Figure 4-3d), which also corresponds to the PSF of the OCT system. The observed shape of the PSF is attributed to the non-Gaussian shape of the light source spectrum.

4.2.1.3 System Characterization

Axial Resolution

The measured SLD spectrum and the corresponding PSF is shown in Figure 4-4. The non-Gaussian spectral shape of the light source spectrum results in side lobes in the PSF. The side lobes can degrade the axial resolution by masking the presence of scatterers that are close together in the axial direction. It should be noted that any asymmetrical changes to the shape of the PSF is a sign of dispersion imbalance or an error in the k-space mapping of the spectral data. The axial resolution given by the FWHM of the PSF is found to be 10 μm and is close to the theoretical value of 8.62 μm (Equation 3.15). The axial resolution in biological tissues with typical refractive indices of 1.395 [124] is calculated to be 7.17 μm.

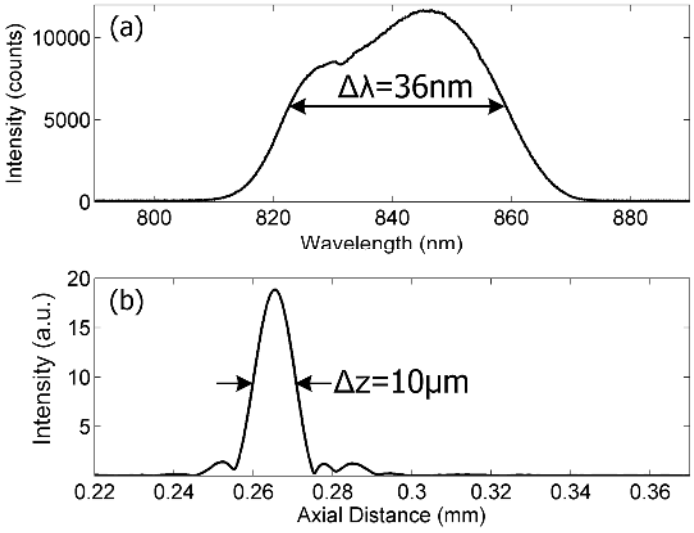

Figure 4-4: (a) Measured SLD wavelength spectrum and (b) PSF of SLD spectrum in the spatial domain.

Confocal Parameter

The achromat lens with 100 mm focal length is characterized to evaluate its confocal parameters. The beam axial intensity profile of the achromat lens is measured by scanning a mirror in the beam propagation direction across the beam focus and recording the back reflected intensity. The confocal parameter of the achromat lens is given by the width of the normalized intensity profile at half the peak value in Figure 4-5. The 100 mm focal length achromat lens offers a large confocal parameter of 1 mm and is therefore suitable for bulk tissue imaging [76].

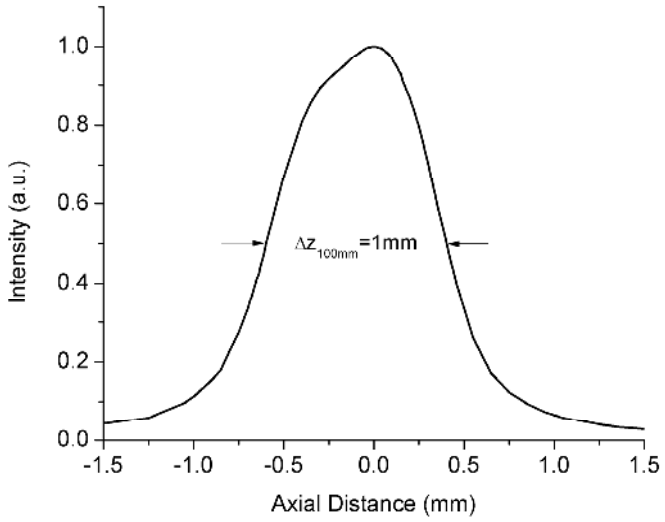

Figure 4-5: Measured confocal parameter of achromat lens with focal length of 100 mm.

Lateral Resolution

The lateral resolution defines the smallest feature that can be imaged in the lateral direction and is found by measuring the focused beam spot diameter of the objective. One common approach to measure the beam spot diameter is the scanning knife-edge technique [155-156]. A cleaved silicon wafer edge is scanned across a beam at the focus and the resultant intensity is recorded. The beam width is measured between two points in the recorded intensity that contain a selected percentage of useful energy. One commonly used beam width reference point for Gaussian beam is the $1/e^2$ value, corresponding to a beam power of 13.5% of the maximum intensity. In our work, the beam spot is calculated from the positions of the scan stage when the measured beam intensity is 13.5% and 86.5%, respectively. The measured beam spot size of the 100 mm focal length achromat lens used in the OCT system is found to be 6.3 μm in air, as shown in Figure 4-6. This is about 2 times the theoretically calculated spot size (Equation 3.17)

and is attributed to the partially filled (half) back aperture of the achromat lens in the OCT setup. The lateral resolution is equivalent to the beam spot size and it is about 4.5 μm in tissues. This is sufficient to image tissue microstructures and epithelial cells.

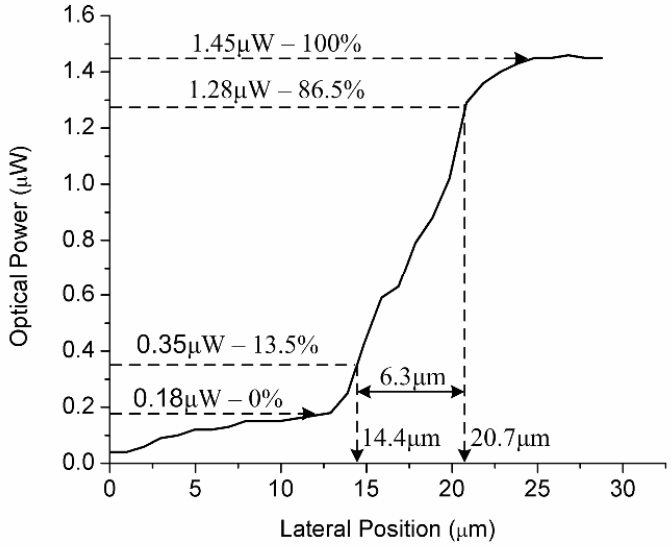

Figure 4-6: Measured lateral beam spot of 100 mm focal length achromat lens using beam power reference points at $1/e^2$ of maximum beam power.

Imaging Depth

The OCT scan depth of the 100 mm achromat lens used is characterized with tissue phantoms of 1% intralipid, which mimics the optical properties of biological tissues [157-159]. 100 scans of an axial position in the intralipid are recorded and averaged. Figure 4-7 shows that the backscattered intensity decay profile stays above the noise floor up to a depth of about 1.05 mm from the specular reflection at the fluid surface (refer to ROI). This is attributed to the large confocal parameter of the achromat lens.

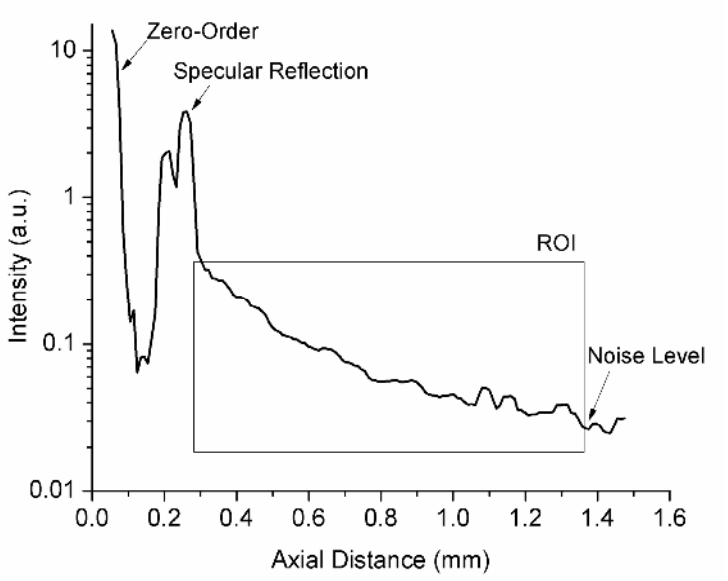

Figure 4-7: Imaging depth characterization of the OCT system with the 100 mm achromat lens using 1% intralipid solution. ROI – Region of interest.

SNR

The sensitivity of the OCT system is an important parameter as OCT is an optical imaging modality in which tiny changes in the intensity of light in one arm of the interferometer can be detected, even when the intensity level is very low. In our system, 26 dB (due to double pass) of attenuation was introduced in the reference arm using ND filters. 60 dB of attenuation was introduced in the sample arm to prevent the spectrometer from saturating. The SNR was characterized by placing a mirror at the sample arm and recording the OCT signal. The SNR obtained from the OCT signal is 20 dB (Figure 4-8) and the total SNR of the FD-OCT system comes to 106 dB after taking into account the attenuations introduced into the reference and sample arms.

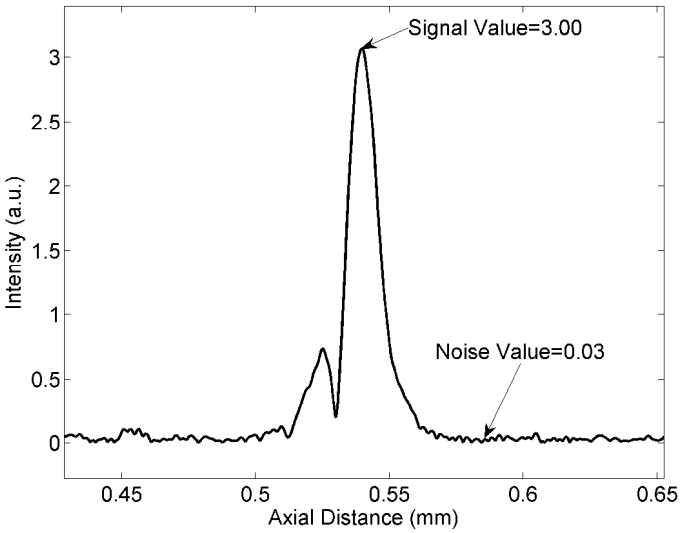

Figure 4-8: Signal to noise of the FD-OCT system.

Scan Field Flatness

A flat surface (a mirror) was imaged to quantify the flatness of the scan field. The front surface flatness of the mirror was specified to be λ/10 at 633 nm. Figure 4-9 shows an OCT image of the mirror. A slight convex curvature of the lateral scan field is observed towards the extreme edges, and this is due to the beam traveling a longer distance at the start and end points of the scan. The deviation of axial distance is measured to be ~50 μm, which is small compared to the whole imaging depth. Consequently no changes are made to correct for this slight curvature.

Figure 4-9: OCT image of a mirror surface.

Scan Speed

The scan speed of the OCT system was measured to be 15 ms per axial scan, or 66 axial scans/s. The scan speed of our FD-OCT system is limited by the USB data transfer rates of the spectrometer and the scanning rate of the galvanometer steering the mirror.

Axial Distance

The axial distance accuracy of the FD-OCT system was characterized by imaging a reference microscope coverslip stacked on top of a reference microscope glass slide of different thicknesses. The OCT axial profile of the measurement is shown in Figure 4-10. The first peak on the left is the zero order, which is obtained when the source spectrum is not totally removed from the spectral interference fringes prior to FT. The zero peak is caused by the DC term in Equation 3.8. This peak does not move when the z-stage is translated. The next three small peaks are due to self-interference from the internal reflections of the coverslip. These peaks are caused by the autocorrelation terms in Equation 3.8. The larger peaks *i* and *ii* come from the reflection of the probe beam from the top and bottom surface of the coverslip. Peaks *iii* and *iv* correspond to the reflection of the probe beam off the top and bottom surface of the glass slide. Since the glass slide is much thicker than the coverslip, photons reflecting off the bottom of the slide and returning through three interfaces are significantly reduced, resulting in a smaller peak. The separation between peaks *ii* and *iii* is attributed to the presence of an air gap between the coverslip and glass slide. The optical thicknesses of the coverslip and glass slide deduced from the OCT axial profile are tabulated in Table 4-2.

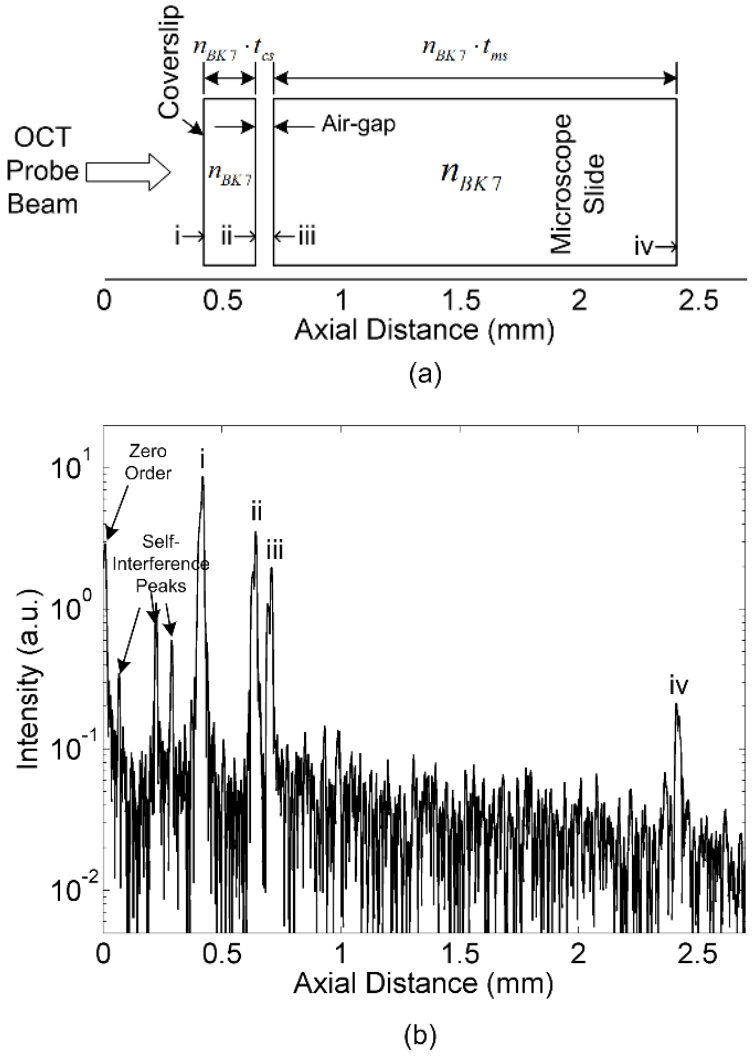

Figure 4-10: (a) Schematic of a microscope cover slip stacked on top of a microscope glass slide. (b) OCT axial profile of the reference setup. *i–iv* corresponds to the sample interfaces indicated in (a).

Table 4-2: Optical thickness measurement of coverslip and glass slide with OCT.

	Measured Physical Thickness, t_m (mm)	Refractive Index of BK7, n_{BK7}, at 840 nm	Optical Thickness, (mm)	
			Calculated $n_{BK7} \cdot t_m$	OCT-measured
Cover Slip	0.15	1.51	0.2265	0.2229
Microscope Slide	1.12	1.51	1.6912	1.7028

For comparison, the physical thicknesses of the coverslip and glass slide were measured using a vernier caliper and multiplied with the refractive index of borosilicate glass (BK7), n_{BK7}, to obtained the corresponding optical thicknesses. The refractive index of BK7 at the OCT wavelength of 840 nm is calculated using the Sellmeier equation [160]:

$$n^2(\lambda) = 1 + \sum_{n}^{N=3}\left[\frac{B_n \lambda^2}{\lambda^2 - C_n}\right] \quad \textbf{(4.3)}$$

where $n(\lambda)$ is the refractive index of the material with respect to wavelength, λ is the wavelength of light, and B_n and C_n are the Sellmeier coefficients of BK7 given in Table 4-3. As shown in Table 4-2, there is good agreement between the calculated and OCT-measured optical thickness and the slight differences are within the 10 μm accuracy of the vernier caliper.

Table 4-3: Sellmeier Coefficients for BK7 Glass [161].

Coefficients	Value
B_1	1.03961212
B_2	0.231792344
B_3	1.01046945
C_1	0.00600069867
C_2	0.0200179144
C_3	103.560653

Lateral Scan Range

The lateral scan range of the OCT system was calibrated using a CCD camera placed at the focus of the objective lens. The scan mirrors were actuated to the extremes of the desired range such that the scanning beam is still within the back aperture of the objective

lens, and the resulting images are captured. Since the pixel count and size of the CCD are known, the lateral scan range can be determine from the start and end pixels of the scanning beam in the images. The lateral scan distance is found to be 6.515 mm and the number of lateral axial scan points is set at 1,000 in the OCT system. The number of lateral scan points was chosen so that each step is close to the beam spot size at 6.3 μm. Each discrete scan step corresponds to about 6.5 μm, which is close agreement to the measured lateral resolution.

4.2.2 Flexor Tendon Specimens

Rabbit flexor tendons were used in this investigation. Freshly excised flexor tendon specimens are obtained from the front and hind paws of New Zealand white rabbits and are stored in saline solution. Some tendons are severed and sutured back together using a 2-strand Kessler stitch. The suture thread used was from Prolene (W8556, Size 5-0), a blue monofilament polypropylene suture. One continuous thread was used for the repair and the thread crosses the severed ends of the tendon twice. The thread is held in place by double loops on each tendon end which act as anchor points. One knot holds the two suture ends together at the joint. The normal, undamaged tendons had their centers marked with a microinjection of dye so that the same points are imaged with OCT. Some tendon samples are placed into a saline-filled petri-dish for rest state scans.

For biomechanical loading tests, OCT imaging was performed on the specimens immersed in saline solution and secured in a custom-made tendon jig. Weights of 10 g, 50 g, 100 g, 150 g, 200 g, 300 g, 400 g, 500 g, 750 g and 1000 g were used to stretch the

tendon. At each loading point, a 6.5×2×1.3 mm^3 imaging volume of the sutured joint for severed tendons or of the marked location on normal tendons was taken. The measurement data was recorded as raw B-scan spectral information and was processed using custom Matlab programs to obtain the OCT images. After imaging, the OCT line scan region of normal tendon was marked with two microinjections of ink before sending it for routine histological processing. Multiple 5 μm thick tissue sections were obtained from the marked region and stained with haemotoxylin and eosin (H&E). Bright field and polarization images of the normal tendon sections were taken digitally using a standard microscope with crossed polarizers. Minor discrepancies between histology and OCT images were attributed to tissue fixation, processing, and sectioning artifacts.

4.3 Results

4.3.1 Rest Sate Normal Flexor Tendon

The rabbit flexor tendon samples are about 40–50 mm in length with an oval cross-section. The muscle end has a width of 2.5–3 mm and a thickness of 1 mm while the width and thickness near the finger end are 2 mm and 1 mm, respectively. The rabbit tendon shown in Figure 4-11a is imaged from right to left starting from the finger end at Section A in the figure. Figure 4-11b shows a typical H&E-stained tendon section with obvious wave-like arrangement of collagen fibers. The internal structures of the tendon section become more obvious when it is observed under a polarization microscope. As shown in Figure 4-11c, the polarized light image reveals a series of bright and dark bands corresponding to the crimp patterns from the highly organized collagen within the tendon.

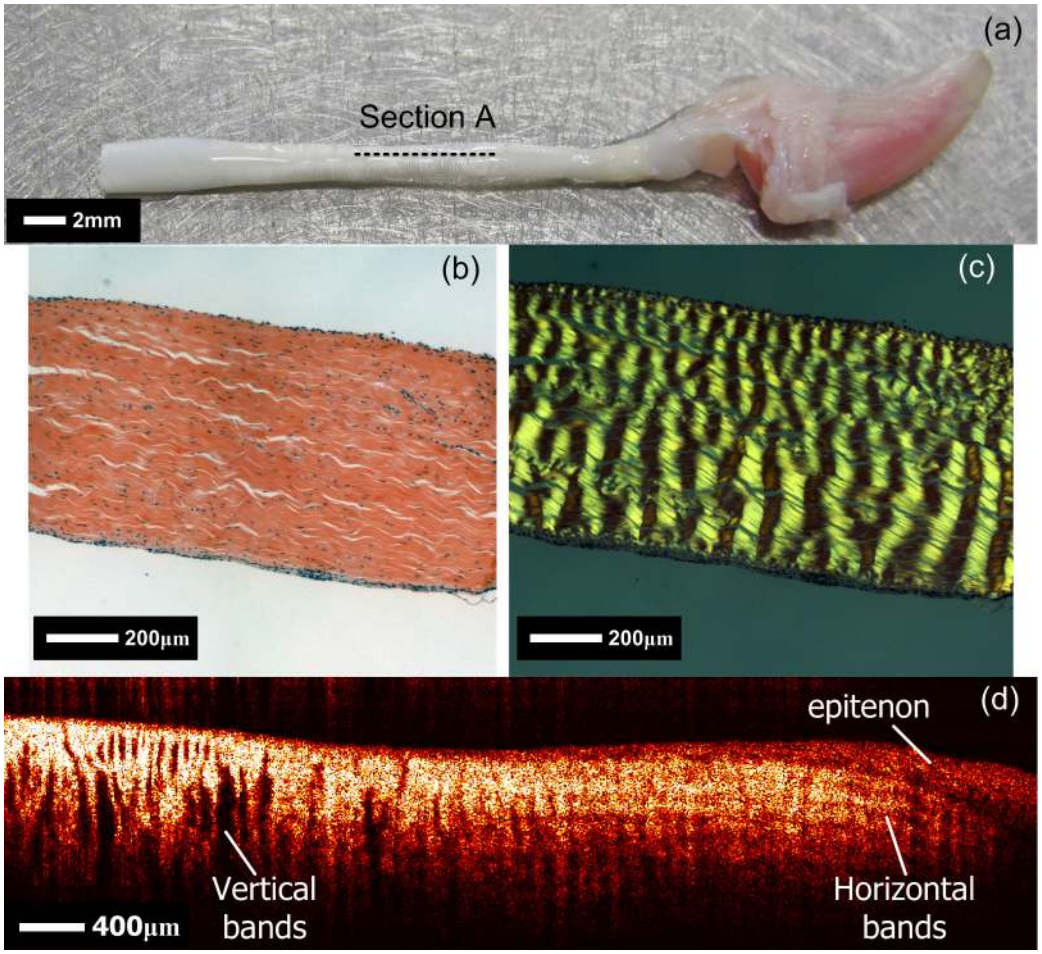

Figure 4-11: Normal tendon rest state imaging. (a) Picture of rabbit flexor tendon with finger attached on right end. Section A indicates the OCT line scan region. (b) Bright field image of H&E stained tendon cross section at section A. (c) Polarization microscope image of tendon cross section at section A. (d) OCT image of flexor tendon at Section A.

The OCT image of the flexor tendon is depicted in Figure 4-11d. A penetration depth of 600–800 μm in the tendon samples is achieved with the FD-OCT system. The epitenon, a protective cover made up of disorganized collagen fibrils surrounding the tendon, is observed as a thin uniformly scattering layer on the tendon surface in the OCT image. By contrast, the underlying collagen within the tendon is highly organized, and the associated vertical and horizontal bands can clearly be discerned. The vertical and

horizontal bands in some samples are observed to overlap one another and the relative strength of either phenomenon can be used to quantify the local conditions of collagen organization in the tendon [143-145].

The polarization of the incident light in the OCT measurements is also varied, by placing a linear polarizer in the light path of the reference and sample arm of the FD-OCT system respectively. The linear polarizer in the reference arm is left in a fixed position and the polarizer in the sample arm is rotated relative to it. **Figure 4-12** shows the OCT images of a tendon sample that was imaged at different polarization positions. **Figure 4-12**a shows the tendon OCT image without the polarizers and the vertical bands are clearly observed. When the polarizers are introduced, the image quality is reduced due to the imbalanced interferometer, leading to dispersion. The main vertical bands are still visible, and the sample arm polarizer was rotated from 0° to 135° (**Figure 4-12**b-e) and the vertical banding is observed to remain largely unchanged. This is consistent with the general consensus that the vertical bands originate from the wavy crimp patterns of the collagen fiber organization in the tendon, which is polarization insensitive [111, 144-145]. The period of the vertical bands in our rabbit tendon is found to vary between 100 – 200 μm. By contrast, the horizontal bands in the OCT images are found to shift when the polarization of the incident light is varied. This is in good agreement with previous studies [111, 162] and indicates that the horizontal bands are induced by collagen birefringence. As the light polarization states in the reference and sample arms of the OCT system are unknown, the actual phase retardation in the birefringent regions of the sample revealed in the OCT images were not extracted in this work.

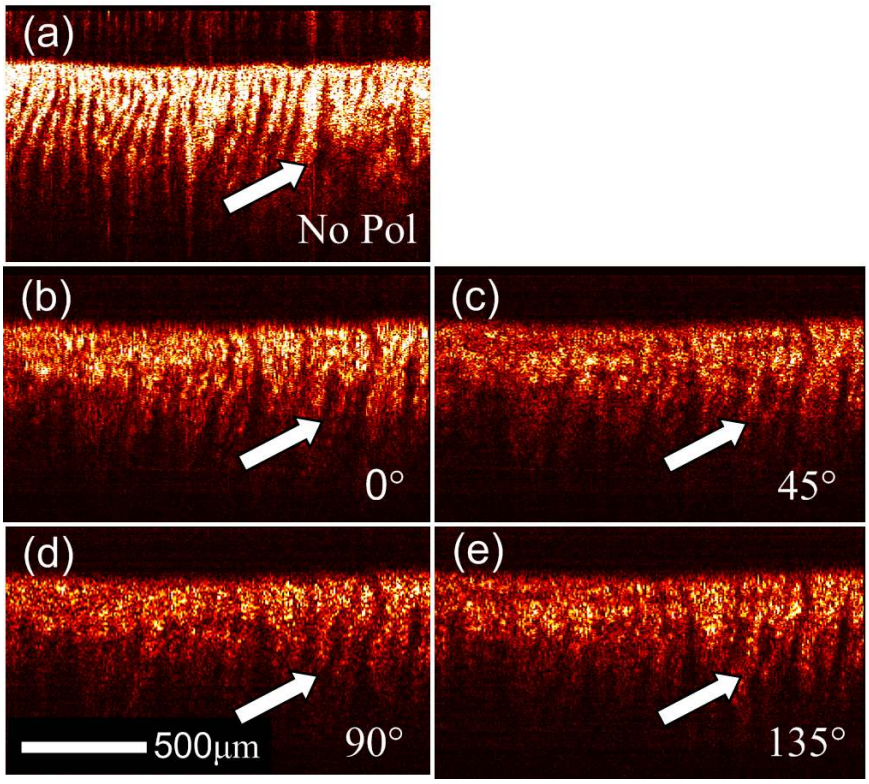

Figure 4-12: Comparison of tendon OCT images with respect to polarization dependence. (a) No polarizers, (b) Sample arm linear polarizer at 0° relative to reference arm polarizer, (c) Sample arm linear polarizer at 45° relative to reference arm polarizer, (d) Sample arm linear polarizer at 90° relative to reference arm polarizer, (e) Sample arm linear polarizer at 135° relative to reference arm polarizer. White arrows in each subsection points to the vertical bands that do not shift when polarization is changed.

4.3.2 Biomechanical Loading of Normal Flexor Tendon

The normal flexor tendon used in the biomechanical testing is mounted in the loading rig for OCT imaging. As seen in Figure 4-13, the vertical bands are clearly visible when there is no tensile load. At 1.0 N load, the bands near the center of the tendon start to become less distinct and take on increased scattering. With increasing tensile load, the bands near the central region of the tendon first disappear and are replaced by a uniform scattering region. This is attributed to the wavy collagen patterns straighten out in a

nonlinear way as the tendon fascicles come under load. The straightened collagen fibrils scatter incoming light in a uniform manner, thus eliminating the vertical bands. The disappearance of the crimp pattern in the OCT images clearly reveals that the first mechanical response of the tendon to load occurs in the central region of the sample [111]. The uniformly scattering region gradually spreads to the tendon extremities as the tensile load increases to 4.0 N. Beyond this load, the uniform scattering intensity in the tendon OCT section is observed to increase.

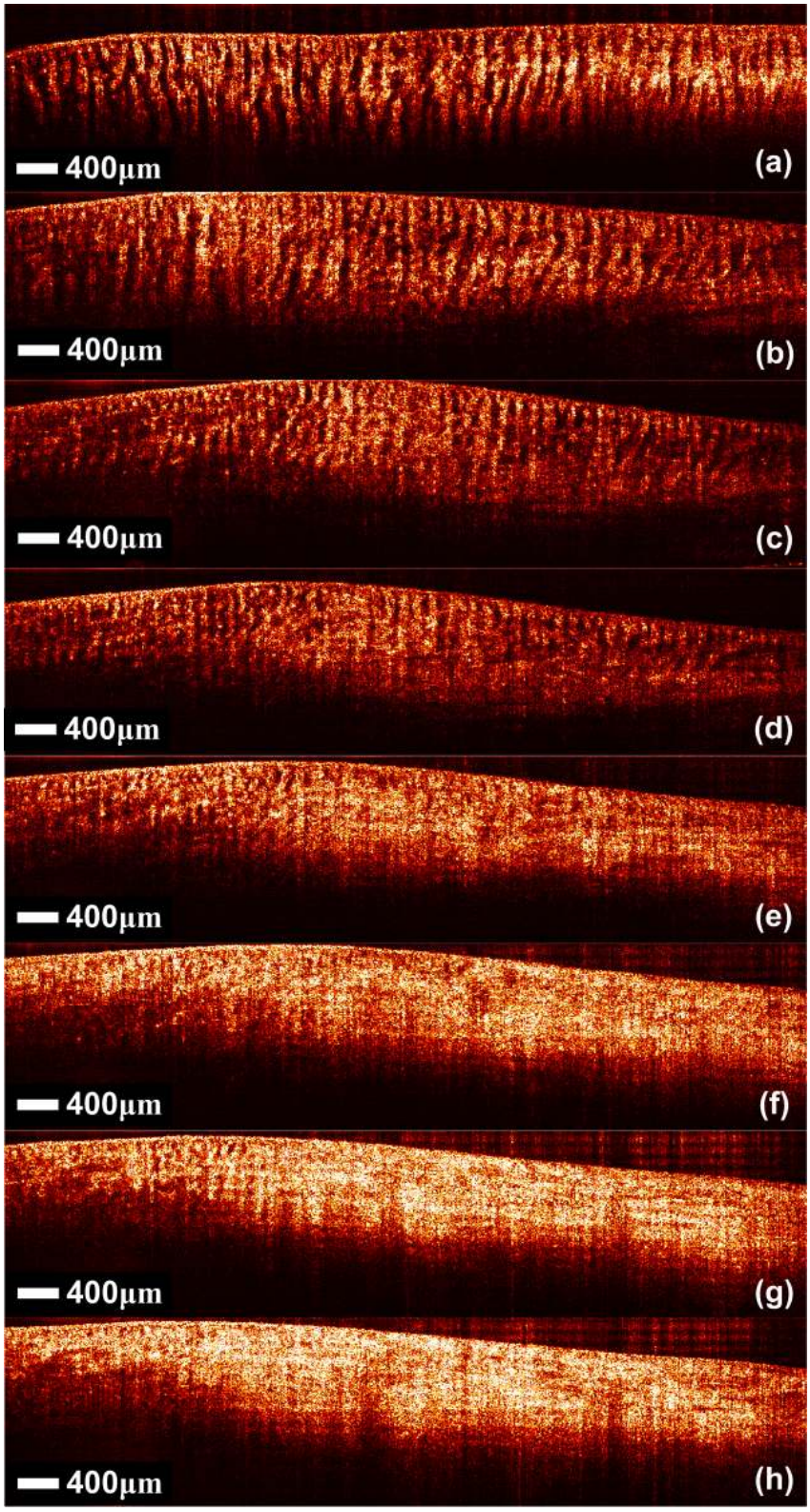

Figure 4-13: OCT images of normal rabbit flexor tendon under loads of (a) 0 N, (b) 1 N, (c) 2 N, (d) 3 N, (e) 4 N, (f) 5 N, (g) 7.5 N, and (h) 10 N.

The OCT image of the flexor tendon after removing the maximum load of 10 N is shown in Figure 4-14. The flexor tendon did not return to its original state after the 10 N load was removed, indicating that it has been stretched beyond the elastic limit. In addition, microtears in the form of horizontal elongated voids cutting across vertical bands in the collagen structure are observed in the OCT image. The length and cross sectional depth of the microtears are 200–400 μm and 50–100 μm, respectively. These microtears in the tendon will lead to a reduced tensile strength and increase the possibility of tendon rupture [163-164].

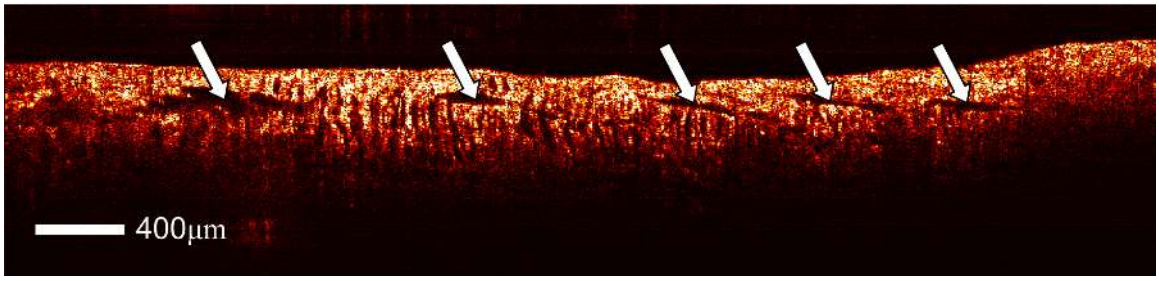

Figure 4-14: OCT image of normal rabbit flexor tendon after the maximum load of 10 N was removed. Arrows marked the microtears observed in the sample.

4.3.3 Biomechanical Loading of Repaired Flexor Tendon

The OCT images at the suture joint of a tendon under loads of 0.1 N to 10 N are shown in Figure 4-15. No visible gap at the suture joint is observed under loads of 0.1 N and 0.5 N. When the load is increased to 1.0 N, a small gap of about 120 μm appears at the suture joint. The gap separation is observed to increase with load of up to 10 N, as depicted in Figure 4-15d–j. It is also noted that the repaired tendon did not return to its original position after the maximum load of 10 N is removed, suggesting that the tendon has been stretched beyond the elastic limit. In other samples tested, some repaired tendons were

observed to rupture at the suture knot when the maximum load is applied. The crimp patterns in the unloaded repaired tendon were observed to be highly scattering due to the compressive stress produced by the suture. When the repaired tendon is stretched, the crimp patterns become more distinct with less scattering as the tensile load counters the compressive stress. The suture gap separation is also found to increase linearly with load before leveling off beyond a load of 5 N. The 2 mm gap force, typically determined in biomechanical testing [165-169] to assess the risk of premature rupture at the repaired tendon joint, corresponds to about 5 N. The ultimate tensile force, a quantitative property used to describe when the sutured joint totally fails, is found to be approximately 10 N from measurements of the OCT images.

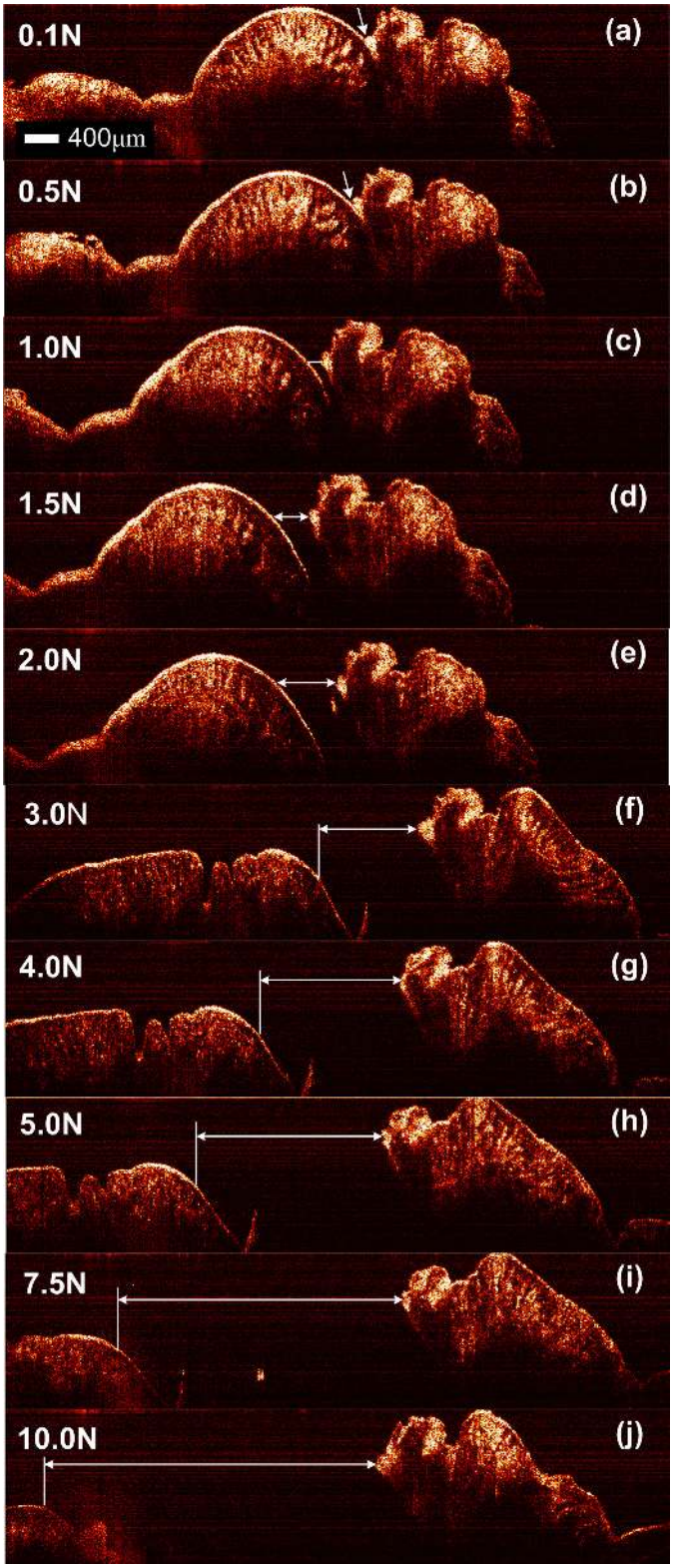

Figure 4-15: (a)-(j) OCT images of the sutured flexor tendon under loads of 0.1−10 N. White arrow in the 0.1 N and 0.5 N images indicates the location of the tendon joint.

4.4 Discussion

Tendons are structurally detailed with bundles of collagen fibers wrapped in a tendon sheath. At rest, the collagen fibers form a wavy crimp pattern which straightens when under loading stress [143-145, 170-171]. The scattering characteristics of crimp patterns in the OCT images of normal and repaired tendons (Figure 4-13 & Figure 4-15) clearly reveal how load is distributed in the tendon samples when load is applied. In some normal tendons tested, the vertical crimps in the OCT images were observed not to disappear at high loads due to uneven load distribution. In studies investigating the early pathophysiologic changes of tendon under cyclic loading [163-164], microtears introduced by repetitive, high force hand activities were found to be the precursors of tendinopathy. It has been shown such cavitation occurs in materials that are on the verge of failure [172] and is a way for the material to dissipate stored energy. The early microstructural changes in the repetitively loaded tendon were quantified by the tear density and mean tear size in the corresponding H&E-stained tendon sections. Histological imaging of microtears is both time consuming and cumbersome. Furthermore, we observed that histological preparation can introduce sample damage which looks like microtears. In this work, microtears forming within tendons after tensile loading of 10 N, while not visible to the naked eye, are clearly seen in the OCT images (Figure 4-14). This shows that OCT can also be used to non-invasively image the microtear characteristics in injured tendons to better quantify and understand the degree of tendon damage.

The 2 mm gap in biomechanical testing is traditionally determined from visual inspection [165, 167], video recordings [169] or the use of vernier calipers [166, 168]. The use of OCT imaging can provide insights to the behavior of the suture joint under load and a more accurate determination of the gap size can be achieved. The 2 mm gap force measured in the repaired rabbit tendon is found to be in broad agreement with other flexor tendon gap forces measured in the same rabbit model [173]. It was found that the gap-load relation at gap separations greater than 2 mm becomes nonlinear and this suggests that the repaired tendon is experiencing inelastic strain conditions. The suture is a rigid and strong monofilament thread that does not stretch under load. Instead, loading on the repaired tendon is transferred to the anchor points of the suture. The resulting tensile stress at the anchor points would be much greater than that in a normal tendon when the same load is applied. Consequently the nonlinear changes in the gap separation (above 2 mm) and the inelastic deformation of the repaired tendon under loads greater than 5 N are possibly due to microtears forming near the suture joint.

In most tendon repair work, 2 or 3 mm gap at the suture joint are typically chosen to study and compare tendon repair techniques [169, 173-174]. It has been shown in clinical studies that gap formation is undesirable as gaps larger than 2 mm were associated with increased adhesion (scar tissue) formation and limited mobility of the repaired joint within the tendon sheath [169, 174]. In particular, gaps of 3 mm or more significantly reduced repair strength that led to increased risk of rupture [166]. The results from this work suggest that a tendon undergoes inelastic deformation when the gap separation is more than 2 mm. This indicates that a 3 mm gap may not be suitable for evaluating the

biomechanical performance of tendon repair techniques. Instead, the risk of premature rupture at the repaired tendon joint under biomechanical testing should be assessed with gap separations of less than 2 mm to ensure elastic deformation in the tendon.

The change from compressive to tensile stress at the suture joint under load is also clearly observed as a reduction in the scattering of crimp patterns in OCT images. The cross-sectional OCT information can be used to ascertain the quality of suture repair techniques, and to monitor the healing process in repaired tendons. In the first stage of tendon healing, fibroblastic proliferation results in both the synthesis and resorption of collagen. Over time, the new collagen becomes more organized to give vertical crimps and horizontal bands. Non-invasive, *in vivo* monitoring of repaired tendon healing can also be achieved by quantifying the crimp patterns in the OCT images.

4.5 Summary

The design, implementation and characterization of a FD-OCT system are described. The FD-OCT system is based on an 840 nm center wavelength SLD source to achieve both good axial resolution and imaging depth. The FD-OCT system is used to investigate the optical characteristics of normal and injured flexor tendons with load. Vertical and horizontal bands were observed in the OCT images of rest state tendon. Biomechanical tests of both normal and repaired tendons were performed by loading the samples with weights of up to 1 kg and imaging them with the FD-OCT system. Images of normal tendon under load show increasing brightness with the gradual disappearance of vertical bands caused by the straightening of the tendon crimp. Microtears, which are not visible

to the naked eye, were observed within the tendon after the maximum load of 10 N was removed. The 2 mm gap force and the ultimate tensile force of flexor tendons were found to be 5 N and 10 N, respectively. The nonlinear changes in the gap separation (above 2 mm) and the inelastic deformation of the repaired tendon under loads greater than 5 N were attributed to microtears forming near the suture joint. The OCT modality is suitable for the non-invasive quantification of tendon biomechanical properties and assessing the quality of suture repair techniques, and has great potential for monitoring the healing process in repaired tendons.

Chapter 5 Dual Window Dual Bandwidth Spectroscopic Metric for Qualitative Scatterer Size Differentiation in Tissues

5.1 Introduction

The broadband nature of the light source used in OCT imaging allows spectral analysis to be performed on the OCT signals to obtain additional information on the properties of scatterers in a sample. SOCT, a natural extension to conventional OCT imaging, allows particle size distribution to be determined from the extracted depth dependent wavelength scattering profile [38, 114-118] in a sample. Spectroscopic differentiation is possible when two or more scatterer types in a sample backscatter differently over the wavelength range of the OCT light source.

The differentiation of scatterer sizes in a SOCT image is affected by three main factors, namely the light source bandwidth, the time-frequency transform used and the choice of spectroscopic metric. A broad bandwidth light source increases the ability of the SOCT system to record low frequency spectral modulations indicative of small particles, thus effectively increasing the spectroscopic resolution [38]. In instances where a non-broadband spectral bandwidth source is used in the OCT system, the spectral resolution of the source spectrum and the detectivity of low frequency spectral modulations can become limited.

Spectroscopic analysis with windowed time-frequency transforms (TFT) suffers from the tradeoff between time and frequency resolutions when linear transformations such as STFT or MWT are used. Bilinear transformations like the Wigner-Ville (WVD)

distribution are a further improvement over linear transformations as they can better reduce the spread in time-frequency transformation [38, 175]. However, WVDs suffer from cross-term effects due to the self-interference of the signal. To overcome these limitations, the DW method developed by Robles *et al.* [116-117] for reconstructing TFDs applies a narrow and wide Gaussian window simultaneously to spatial domain data (Equation 3.19). The transformed data from each window is then multiplied together to achieve a local spectral scattering profile, or spectral modulation, with concurrently high spectral and temporal resolutions.

A spectroscopic metric used to describe particle sizes in an SOCT image is generally based on the degree of depth-dependent spectral modulation encountered at specific depths in a sample. Among the many spectroscopic metrics reported in the literature, the bandwidth of the depth-dependent spectral modulation autocorrelation function is the most promising due to its insensitivity to Doppler shifts and depth-dependent frequency chirp caused by dispersion in SOCT measurements [115]. While the DW method has significant advantages over the commonly used STFT and CWT methods [116-117], there has not been a systematic study of the spectral modulation autocorrelation bandwidths to determine an optimal spectroscopic metric that has the best sensitivity to scatterer size.

This chapter investigates how various DW spectral modulation autocorrelation bandwidths change with scatterer size and identify an optimal metric for quantifying scatterer sizes in SOCT images obtained from the FD-OCT system developed in Chapter

4. The spectroscopic analysis of the OCT axial profile is based on the DW method with comparisons to the conventional STFT approach. Microspheres of varying sizes were first characterized with the DW-SOCT technique to determine a suitable spectroscopic metric and its correlation to scatterer size. Simulation was also performed to verify the results and to understand the factors affecting the spectrometric metric. The contrast enhancement in scatterer size differentiation using the proposed approach is demonstrated in the SOCT images of microsphere control and tonsil tissue samples.

5.2 Materials and Methods

5.2.1 Microsphere Specimens

Polystyrene microspheres with sizes of 0.5, 1.0, 10, 25, 45 μm in solution were used for identifying an optimal spectroscopic metric for quantifying scatterer size. The 0.5, 1 μm microspheres are from Fluka, and the 10, 25, 45 μm microspheres are from Polysciences. The refractive index of the spheres is 1.59 at 589 nm. 1,000 OCT axial scans at the same location for each microsphere solution are recorded and analyzed. The concentrations (particles/ml) of the microsphere solutions are shown in Table 5-1. The microspheres used in this work are in bold and the other particle sizes are used as comparison to explain the choice of the microsphere sizes used for this work. The inter-particle spacing values were calculated using a simple model as the particle sizes and the concentration values are known, and the basic assumption was that all the particles are equally spaced from each other. The implications of the relationship between the microsphere concentration and inter-particle spacing on the spectroscopic metric are discussed in a later section.

Table 5-1: Microsphere sizes and their corresponding concentration and calculated inter-particle spacing. Microspheres used in this work are in bold and the other microsphere sizes are included for comparison.

Particle Size (μm)	Particle Concentration (particles/ml)	Inter-particle Spacing (m)
0.1	3.1×10^{13}	4.04×10^{-6}
0.2	4.6×10^{12}	6.79×10^{-6}
0.5	**3.2×10^{11}**	**1.56×10^{-5}**
1	**2.3×10^{10}**	**5.47×10^{-5}**
2	5.6×10^{9}	5.55×10^{-5}
10	**1.82×10^{7}**	**6.93×10^{-4}**
25	**1.16×10^{6}**	**1.74×10^{-3}**
45	**5.17×10^{5}**	**1.19×10^{-3}**

5.2.2 Dual Window Spectroscopic OCT Analysis

The DW method, with significant advantages over the STFT and CWT methods [116-117], is used for TFT in this work. An autocorrelation is taken of the spectral modulation obtained from the DW method and the bandwidth of the resulting autocorrelation function is used as the spectroscopic metric. This parameter quantifies the local spectral modulation obtained from backscattered light associated with scatterer sizes encountered at specific depths in a sample.

The process of spectroscopic analysis of an OCT axial data is illustrated in Figure 5-1. The primary and secondary windows are applied to the measured axial profile with the center of the windows located at the depth-of-interest (Figure 5-1a). The axial profile has a total of $2^{15}/2 = 16384$ data points due to the zero-padding performed prior to FT. The large number of data points provides good sampling resolution for the windowed data as

well as enhancing positional sensitivity [154]. The windows are translated along the axial direction, and the primary and secondary windowed profiles at a particular depth are shown in Figure 5-1b-c. The resulting *k*-space scattering profiles depicted in Figure 5-1d-e are obtained from the FT of these local windowed profiles. The size of the primary and secondary windows used in this work are 512 and 4096 pixels, respectively, and are chosen to ensure that the conditions of $\sigma_{PW} << \sigma_{SW}$ are met. These correspond to spatial resolutions of 47 μm and 380 μm, respectively, and to spectral resolutions of 7.5 nm and 0.93 nm, respectively, when evaluating the FWHM of the Gaussian windows.

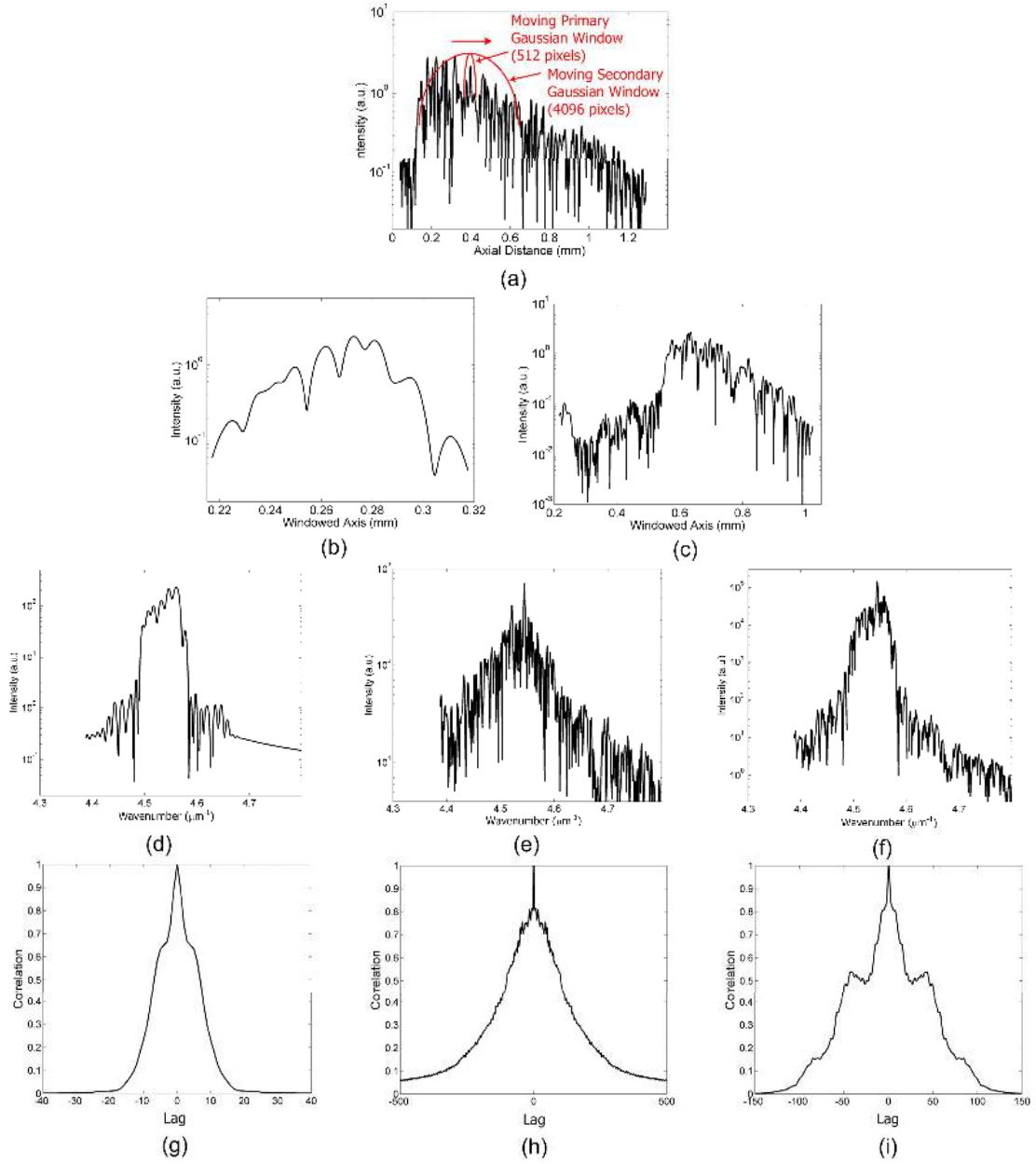

Figure 5-1: Illustration of the spectroscopic analysis of OCT axial data. (a) Applying primary and secondary Gaussian windows to an OCT axial profile. (b)-(c) Primary and secondary windowed data sections at a particular depth. (d)-(e) Primary and secondary windowed *k*-space local scattering profiles. (f) DW *k*-space scattering profile. (g)-(h) Primary and secondary windowed autocorrelation functions. (i) DW autocorrelation function.

The resulting DW *k*-space scattering profile (Figure 5-1f) is obtained from the product of the primary (Figure 5-1d) and secondary scattering profiles (Figure 5-1e). The degree of

spectral modulation and the autocorrelation shape of the local spectra are of interest here as they can be used to extract information about the distribution of scattering particles [115]. This is determined by performing a standard autocorrelation operation on the DW scattering profile to obtain a DW autocorrelation function (Figure 5-1i). The autocorrelation functions of the primary and secondary windowed scattering profiles are shown in Figure 5-1g-h for comparison. The autocorrelation is performed in *k*-space and the unit of the lag-axis is the same as that of wavenumber. In this analysis the lag values are expressed in terms of pixel number since only the magnitude of the autocorrelation bandwidth values is of concern [115]. The shape of the autocorrelation function is related to the size of the scatterers in the sample, as the degree of spectral modulation is directly dependent on the diameter and refractive index of the scatterer. Large scatterers will produce a high modulation frequency while small scatterers will give rise to low modulation frequency [176].

A spectroscopic images is created from combining the structural (represented by OCT intensity) and spectroscopic (represented by spectroscopic metric) information together in a single color image [115]. The Hue/Saturation/Luminance (HSL) color map [115] is used to represent spectroscopic information at each image pixel, where the hue parameter encodes the spectroscopic information and the OCT intensity is assigned to both the saturation and luminance parameters. Representation of OCT intensity by both saturation and luminance gave better structural contrast and more vivid colors in the spectroscopic images. A hue range of 0 to 0.6 is used to ensure that spectroscopic metrics mapped to the minimum and maximum hue values do not have the same color. The values of

saturation and luminance can range from 0 to 1 [115]. The resulting HSL image is finally converted to a color RGB image for visualization and quantitative analysis of scatterer sizes and distribution.

5.2.3 Tonsil Tissue Specimens

The spectroscopic metric developed in this work is evaluated with human palatine tonsils. The palatine tonsils are lymphoid organs and are situated behind the base of the tongue and guard the entrance to the upper respiratory and gastrointestinal tracts. Human palatine tonsils, as part of the immune system in the head and neck region, prevent infection from exogenous material entering the body. The palatine tonsils are covered by stratified squamous epithelium, which are flattened cells arranged in layers on top of the basement membrane. The epithelium extends into crypts which penetrate the lymphoid tissue deeply [62]. The crypts are like fissures in the epithelium of the tonsil and they greatly increase the contact surface between the external environment and lymphoid tissue. Under the stratified squamous epithelium, the dense lymphoid tissue contains germinal centers which produce lymphocytes.

Freshly excised palatine tonsil specimens are obtained from patients in the National University Hospital (Singapore) with approval under DSRB Study Protocol OCT_B/07/025. The specimens are placed in a petri-dish with formalin levels above the top of the specimen and OCT imaging is performed *ex vivo*. A $6.5\times1\times2$ mm^3 imaging volume of each tonsil sample is taken using the FD-OCT system described in Section 4.2.1. The measurement data was recorded as raw B-scan spectral information and is

processed using custom Matlab programs to obtain the OCT and spectroscopic images. After OCT imaging, the line scan region is marked with two microinjections of ink and the tissue is placed into a tube of 10% neutral buffered formalin before sending it for routine histological processing. Multiple 5 μm thick tissue sections are obtained from the OCT imaging planes and stained with tissue stains haemotoxylin and eosin (H&E) to highlight cellular features. Histology images were taken digitally using a standard microscope and compared with the OCT images. Minor discrepancies between histology and OCT images are attributed to tissue fixation, processing, and sectioning artifacts.

5.3 Results

5.3.1 Spectral Autocorrelation of Polystyrene Microspheres

The autocorrelation functions of microspheres obtained from local spectral modulations processed with a narrow and a wide STFT window are shown in Figure 5-2a and Figure 5-2b, respectively. There is limited content of spectral modulations when a narrow STFT window is used, and the autocorrelation functions show little variation. The use of a narrow STFT window in spatial domain achieves good spatial resolution but poor spectral resolution. By contrast, the use of a wide STFT window in spatial domain results in poor spatial resolution but good spectral resolution, as evidenced by the large base of the autocorrelation functions.

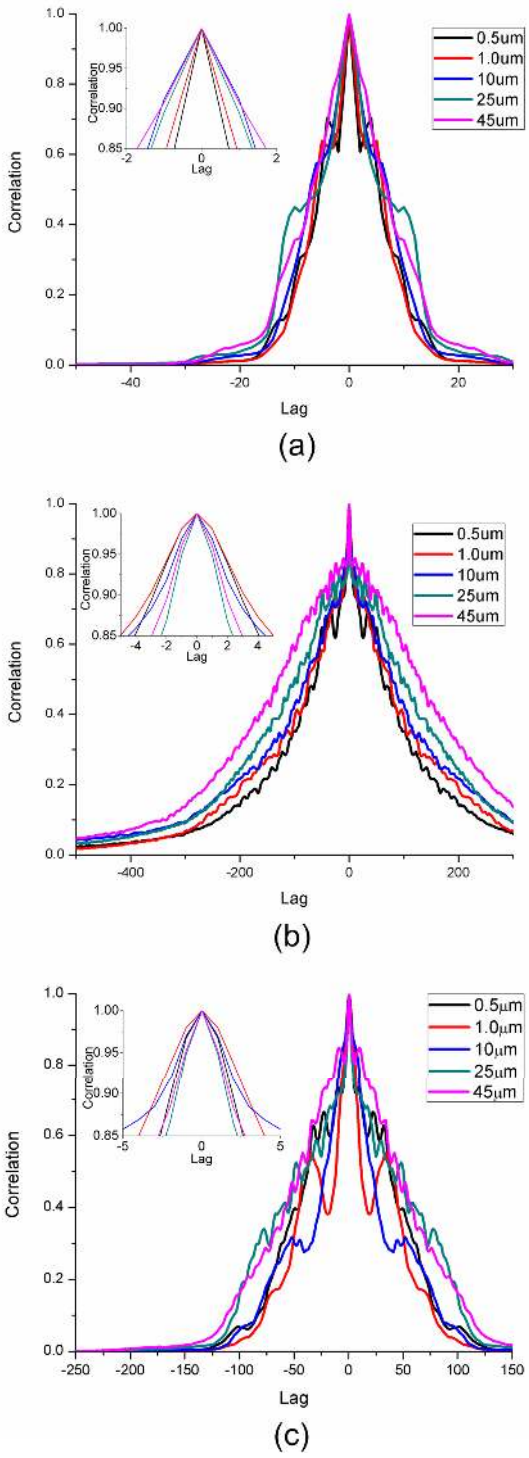

Figure 5-2: Autocorrelation functions of local spectral modulations obtained from microspheres with differing sizes. (a) Narrow STFT window autocorrelation functions. (b) Wide STFT window autocorrelation functions. (c) DW autocorrelation functions. Insets: Enlarged view of the autocorrelation functions near their peak values.

The DW autocorrelation functions of microspheres with varying sizes are presented in Figure 5-2c. The horizontal range (lag) of the DW autocorrelation functions are smaller than those reported by Adler *et al.* [115] due to the smaller light source bandwidth used in this work. Despite the smaller range of lag, a richer content of spectral modulations are observed in these autocorrelation functions as a result of the concurrently high spectral and temporal resolutions provided by the DW technique. As shown in Figure 5-2c, the large 25 μm and 45 μm microspheres exhibit high modulation frequency while the smaller 1 μm and 10 μm microspheres gave low modulation frequency consistent with theoretical predictions [176]. The high modulation frequency detected in the smallest 0.5 μm microspheres is attributed to multiple particle scattering within the imaging volume [115].

As shown in the inset of Figure 5-2c, the curvature at the peak of the DW autocorrelation function generally decreases as the microsphere size decreases from 45 μm to 1 μm. This is in broad agreement with the trend observed by Adler *et al.* [115]. The larger curvature at the peak of the DW autocorrelation function of the smallest 0.5 μm microspheres is possibly due to multiple particle scattering effects. Other than near the peak of the DW autocorrelation function, it is interesting to note from Figure 5-2c that the bandwidth of the DW autocorrelation function of different sized microspheres changes differently at other heights. To quantify these changes, the DW autocorrelation bandwidths at 10% to 90% of the peak value in 10% steps are plotted as a function of microsphere size in Figure 5-3. The error bars are obtained from the standard deviation of the 1,000 A-scans obtained for each sample.

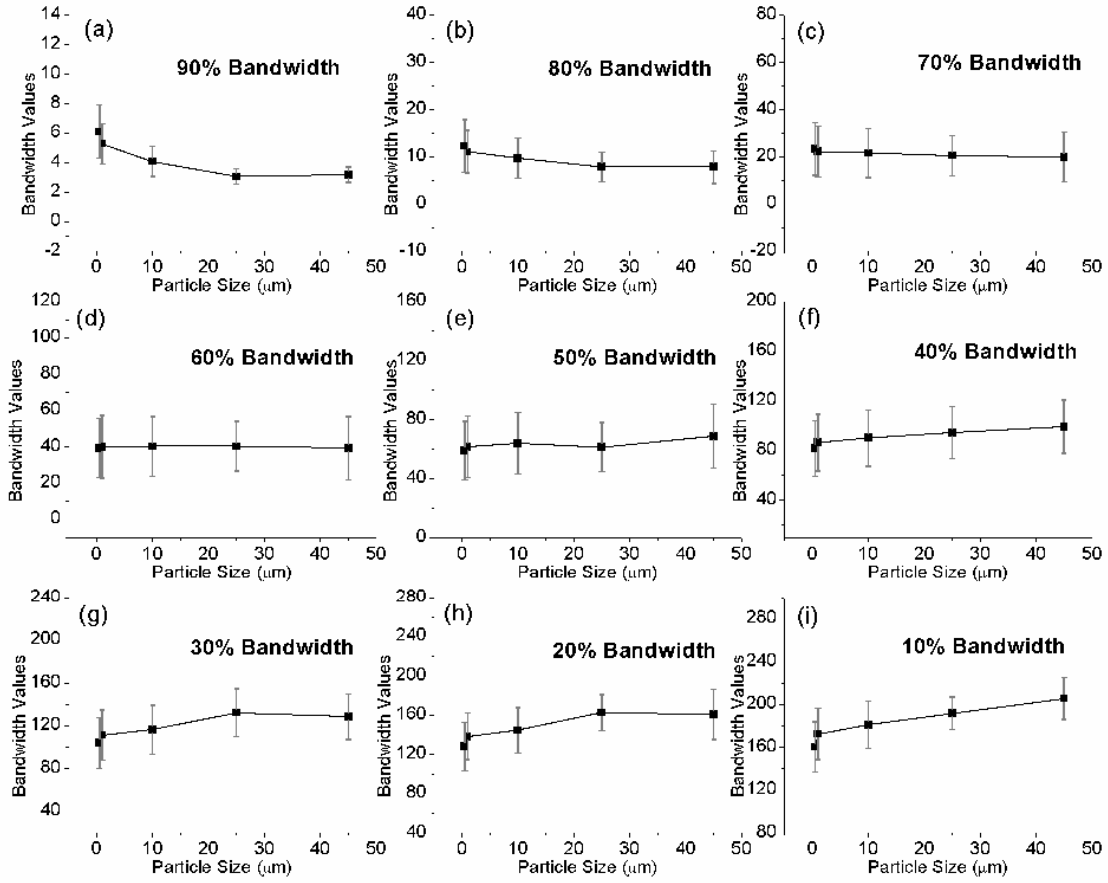

Figure 5-3: DW autocorrelation bandwidths at 10% to 90% (a)-(i) of the peak value plotted as a function of microsphere size. Error bars represent ±1σ.

It can be seen in Figure 5-3 that the 90% bandwidth, m_{90}, exhibits the largest change in values with microsphere size, confirming that this commonly used metric provides good spectroscopic contrast [115]. The value of m_{90} is also observed to level off for microsphere size larger than 25 μm, indicating that the metric is only sensitive to scatterer size smaller than 25 μm. Besides the 90% bandwidth, the 10% bandwidth, m_{10}, also has appreciable monotonic change with microsphere size. This is attributed to the higher modulation frequency in the DW *k*-space scattering profile of large microspheres which

broadens the base of the corresponding autocorrelation function. A dual bandwidth (DB) metric, m_{DB}, incorporating the monotonically increasing 10% bandwidth and the monotonically decreasing 90% bandwidth can be defined as:

$$m_{DB} = \frac{m_{10}}{m_{90}} \tag{5.1}$$

The sensitivity of m_{DB} to changes in scatterer size using the DW- and the STFT-calculated (Figure 5-2a) autocorrelation functions are illustrated in Figure 5-4. A Gaussian window size of 512 pixels, corresponding to a spatial resolution of 47 μm, is used to calculate the STFT autocorrelation functions. The commonly used 90% bandwidths are also plotted in Figure 5-4 for comparison.

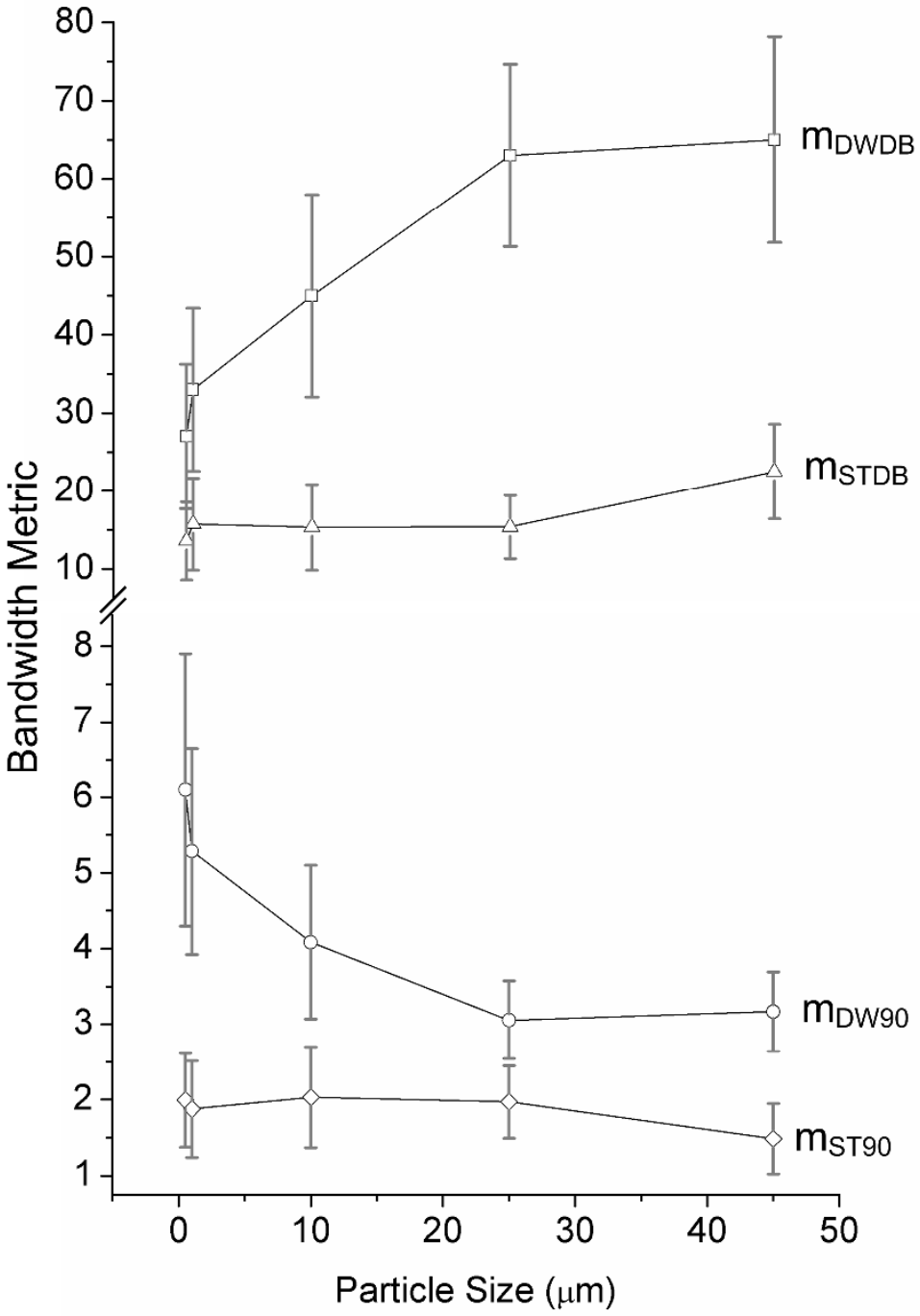

Figure 5-4: Comparison between the STFT-calculated dual bandwidth, m_{STDB} (–△–), the STFT-calculated 90% bandwidth, m_{ST90} (–◇–), the DW-calculated dual bandwidth, m_{DWDB} (–□–), and the DW-calculated 90% bandwidth, m_{DW90} (–○–). The STFT Gaussian window size used is 512 pixels, which corresponds to a spatial resolution of 47 μm. Error bars represent ±1σ.

It can be seen in Figure 5-4 that m_{ST90} is the least sensitive to changing scatterer size. The resulting 90% bandwidth metric based on the DW method, m_{DW90}, is found to change more significantly when the scatterer size varies from 0.5 μm to 45 μm. By contrast the use of the DB metric defined in Equation 5.1 greatly improves the spectroscopic contrast between the small and large scatterers. While the value of m_{DW90} levels off for scatterer size larger than 25 μm (Figure 5-3), an appreciable change is still observed in both the DW-calculated and STFT-calculated dual bandwidths, m_{DWDB} and m_{STDB}, respectively. This is obviously due to the use of the 10% bandwidth in these dual bandwidth metrics, which continues to increase with scatterer size larger than 25 μm. As evident in Figure 5-4, the best spectroscopic contrast is obtained with m_{DWDB}.

To test the DWDB metric, spectroscopic images of the 0.5 μm and 45 μm microspheres are generated using m_{DWDB} for comparison. The spectroscopic image is created from a HSL colour map where m_{DWDB} is mapped to the hue value while the OCT intensity is mapped to both the saturation and luminance parameters. The linear trend of the measured DWDB value with respect to particle sizes between 1 – 25 μm allows it to be mapped linearly to the hue value. For ease of visualization, four unique hues corresponding to blue, green, orange and red are used to represent m_{DWDB} corresponding to tissue scatterer sizes of less than 3.5 μm, 3.5–7 μm, 7–10.5 μm and more than 10.5 μm, respectively. The resulting spectroscopic images for the 0.5 μm and 45 μm microspheres are shown in Figure 5-5.

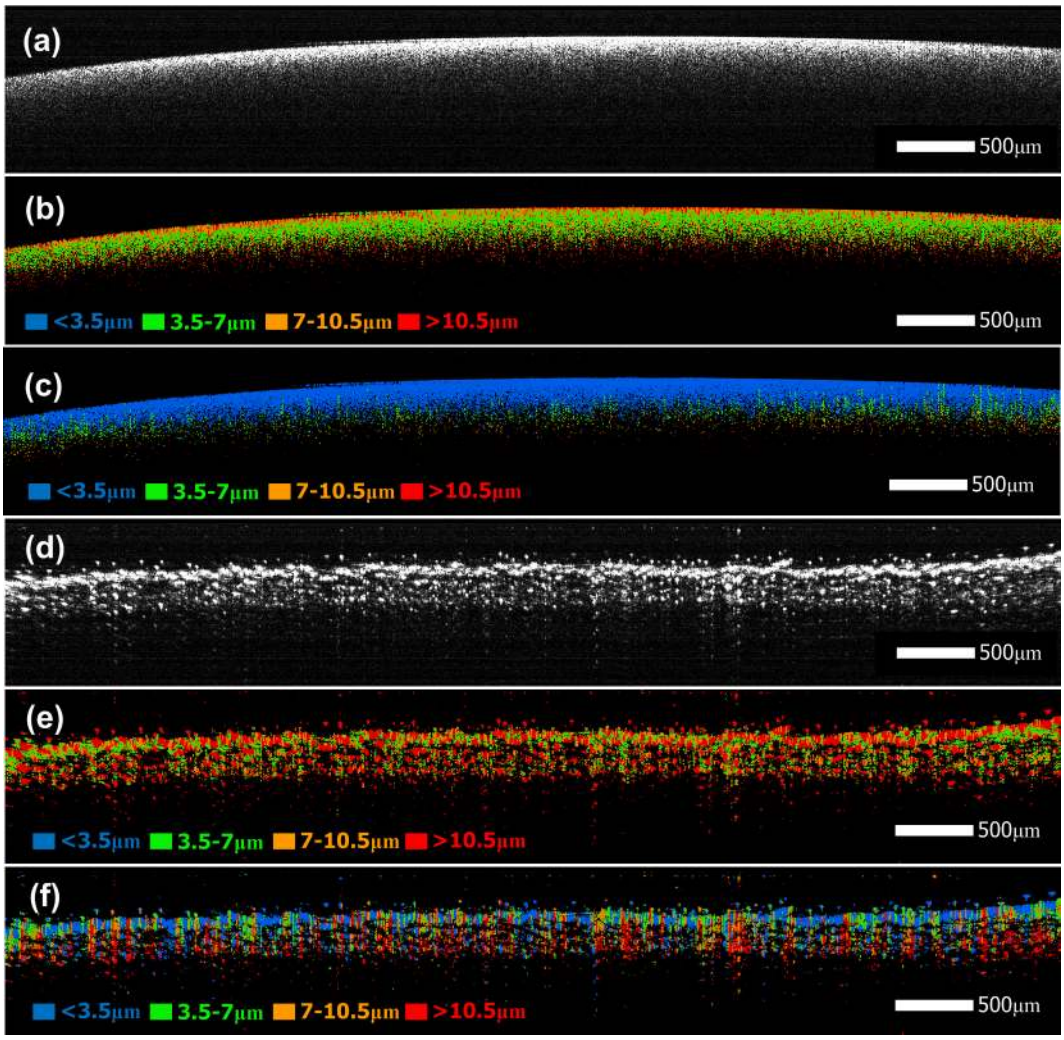

Figure 5-5: (a, d) Conventional intensity-based OCT, (b, e) STFT spectroscopic images, and (c, f) DWDB spectroscopic images of (a, b, c) 0.5 μm and (d, e, f) 45 μm microspheres in solution.

The conventional intensity-based OCT image of 0.5 μm microspheres in Figure 5-5a reveals a uniformly scattering cross-section whose intensity diminishes with depth in the sample. In the case of the 45 μm microspheres, the particles settle to the bottom of the solution quickly and stack up due to their large size. Consequently, the corresponding intensity-based OCT image of the 45 μm microspheres (Figure 5-5d) shows a similarly uniform scattering region with significant granularity. It is also noted that the OCT

signals from the 45 μm microspheres are weaker than those from the 0.5 μm microspheres. This is due to the much smaller concentration of the 45 μm microspheres as compared to the small microspheres, rendering the strength of the scattered signals to be significantly lower. The high reflectivity layers at the surface of the samples are due to specular reflection. As seen in Figure 5-5b, , the STFT spectroscopic image of the 0.5 μm microspheres is colored in green and this is not consistent with the small sized scatterers at <3.5 μm present in the sample. This is not accurate as the sample comprises of 0.5 μm microspheres. For the 45 μm microspheres, the STFT spectroscopic image in Figure 5-5e shows a largely red and green hue which is indicative of large sized scatterers >10.5 μm in size. The DWDB spectroscopic image in Figure 5-5f showed largely red hue which is indicative of the large scatterers (> 10.5 μm) in the sample. The blue and green hues present in Figure 5-5f is attributed to specular reflection and interparticle scattering due to the space between the microspheres, which manifest as small scatterers in the spectroscopic image. The resulting spectroscopic images between the two microsphere control samples can clearly be distinguished using m_{DWDB} .

5.3.2 Spectroscopic Imaging of Human Palatine Tonsils

The DWDB spectroscopic metric was evaluated with *ex vivo* imaging of human palatine tonsil samples to compare its performance with conventional approach. Figure 5-6a shows the histological section of a tonsil sample diagnosed with chronic tonsillitis. Chronic tonsillitis is a condition in which recurring viral or bacterial infections of the tonsils lead to constant inflammation and soreness. When the tonsils are chronically inflamed, they swell and lead to significant, persistent pain in the throat and jaw. Surgery

is necessary in most cases of chronic tonsillitis to relieve symptoms and help prevent future throat infections.

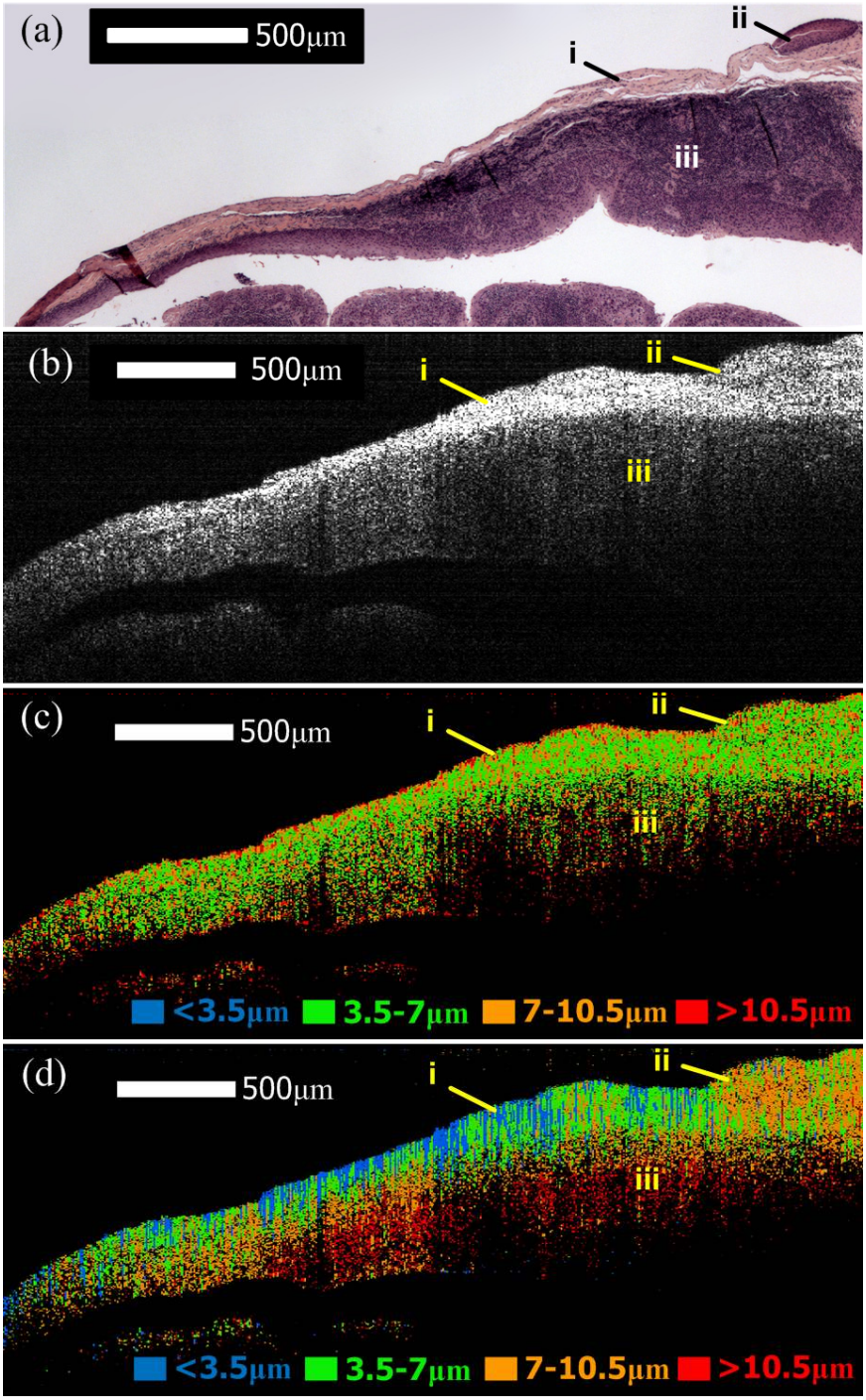

Figure 5-6: Images of human palatine tonsil with chronic tonsilitis: (a) H&E-stained histological section, (b) conventional intensity-based OCT image, (c) spectroscopic image based on STFT-calculated 90% bandwidth metric, and (d) spectroscopic image based on DWDB metric. In (c) and (d), tissue scatterer sizes of < 3.5 μm, 3.5–7 μm, 7–10.5 μm and > 10.5 μm are mapped to the blue, green, orange and red hue, respectively, for clarity. Regions *i*, *ii* and *iii* are loose connective tissue, squamous epithelium and lymphoid tissue, respectively.

The intensity-based OCT image of the tonsil sample shown in Figure 5-6b barely reveals several identifiable regions observed in the corresponding histological section. Region *i* is identified as loose connective tissue comprising collagen and elastin. This tissue is optically highly scattering as compared to the underlying lymphoid tissue, and very good contrast is obtained in the intensity-based OCT image. A section of squamous epithelium marked as region *ii* is found embedded in the highly scattering loose connective tissue. The size of the epithelial cells, as measured from histology and after accounting for cell shrinkage of about 15% post histological preparation [177], is greater than 7 μm. Region *iii* contains lymphoid tissue, which makes up the bulk of tonsil tissue. The lymphoid tissue is very dense and the OCT contrast is much reduced due to this tissue property. The lymphoid cells are found to have an average cell size of about 7 μm from histological measurement. The tonsil tissue structures observed in the intensity-based OCT image can be broadly correlated with the histological image.

The spectroscopic images of the tonsil tissue based on the STFT-calculated 90% bandwidth metric and the DWDB metric are depicted in Figure 5-6c and Figure 5-6d, respectively. These spectroscopic images are created using the same color scheme as as that of the microsphere controls (Figure 5-5b and 5-5d), where the relevant spectroscopic metric is mapped to one of the 4 hues (blue, green, orange and red) in the HSL colour map. As shown in Figure 5-6c, the different sized cells in regions *i*, *ii* and *iii* are not differentiable due to the poor sensitivity of the STFT-calculated metric to particle size. By contrast, the DWDB spectroscopic image in Figure 5-6d clearly differentiates the different sized cells in the sample. Both the larger epithelial and lymphoid cells in regions

ii and *iii* are correctly assigned the orange and red hue while the connective tissues are represented in blue and green. These are in broad agreement with histological observations.

The images of another tonsil sample diagnosed with chronic tonsillitis and reactive hyperplasia are shown in Figure 5-7. Reactive hyperplasia is a condition in which the number of cells in a tissue increases in response to the presence of a pathogen. In the histological image of Figure 5-7a, regions *x* and *y* are identified as the upper epithelium and the basal cell layer, respectively. The upper layer of the epithelium is sparsely populated with cells as compared to the basal layer and comprises squamous cells of less than 7 μm in size from histological measurement. The cells in the basal layer are found to be larger than 8 μm in size. These layers are barely identifiable in the intensity-based OCT image of Figure 5-7b due to the poor contrast. The epithelium layer is relatively thick and light does not penetrate sufficiently into the lymphoid tissue. Consequently, the lower lymphoid tissue is not visible in Figure 5-7b. Using the same spectroscopic color scheme, the spectroscopic images computed based on the STFT-calculated 90% bandwidth metric and the DWDB metric are shown in Figure 5-7c and Figure 5-7d, respectively. The upper epithelium and basal layer are not distinguishable in the STFT-calculated 90% bandwidth spectroscopic image. On the other hand, the cells in the upper epithelium are represented by blue and green whereas the cells in the basal layer are represented by orange, giving clear contrast to cellular size differences. The cellular sizes identified in the DWDB-SOCT image are also in broad agreement with histological observations.

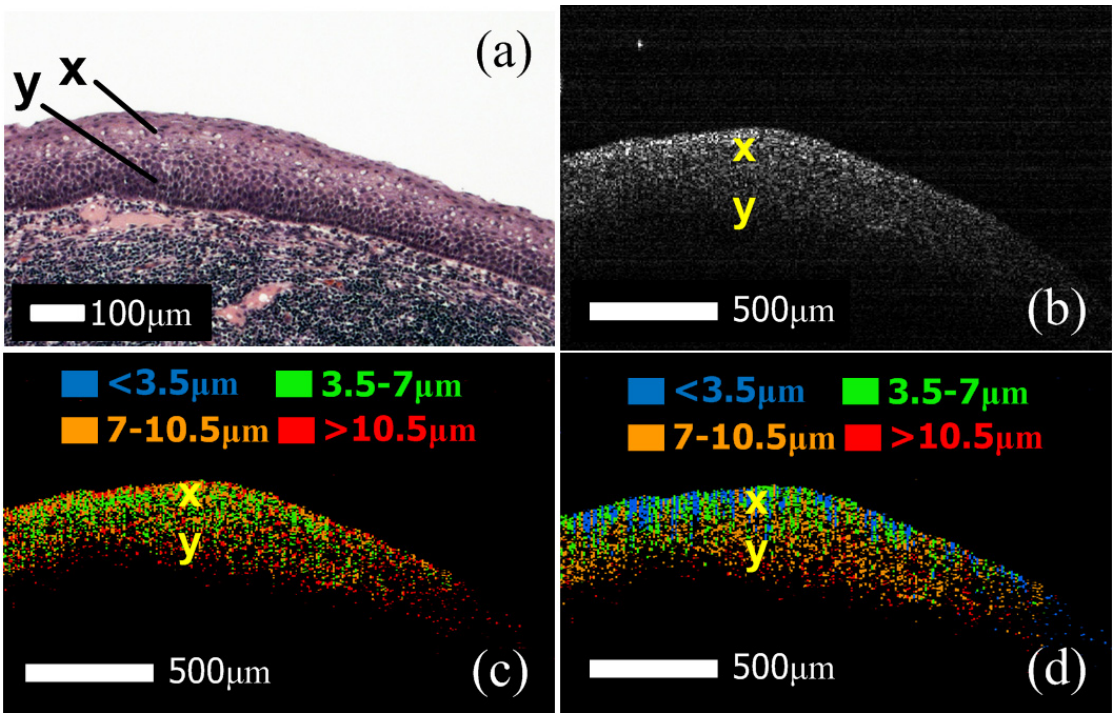

Figure 5-7: Images of human palatine tonsil with chronic tonsilitis and reactive hyperplasia: (a) H&E-stained histological section, (b) conventional intensity-based OCT image, (c) spectroscopic image based on STFT-calculated 90% bandwidth metric, and (d) spectroscopic image based on DWDB metric. In (c) and (d), tissue scatterer sizes of < 3.5 μm, 3.5–7 μm, 7–10.5 μm and > 10.5 μm are mapped to the blue, green, orange and red hue, respectively . Regions *x* and *y* are the upper epithelium and the basal cell layer, respectively.

5.4 Discussion

The DW spectroscopic analysis of OCT signals from the characterization of different-sized microspheres reveals two autocorrelation bandwidth parameters, m_{90} and m_{10}, that have significant monotonic change with scatterer size. A DB metric defined as the ratio of these two parameters (Equation 5.1) gives an optimal DWDB spectroscopic metric that can be correlated to scatterer size. The error bars associated with the measured bandwidth values in Figure 5-3 and Figure 5-4 arise from several factors. Firstly, the measurement of microspheres in solution represents a dynamic system in which the particles are always

moving. Immobilizing the microspheres in a gel would narrow the error bars. This is generally not a concern when imaging tissues since the tissue scatterers are generally immobile. The other factor is related to the Michelson configuration of the OCT system. The presence of a reference arm is found to introduce fluctuations into the measurements. Test measurements on the microspheres are carried out with an improvised common path OCT configuration using a microscope coverslip as the reference surface and the standard deviation of the metric values is greatly reduced (results not shown). Consequently the limit in spectroscopic resolution imposed by this factor can be minimized through the use of an appropriate OCT detection scheme.

Scatterer concentration is a sample parameter which affects the spectroscopic metric, and this is observed from the microsphere calibration experiments. Higher particle concentrations affect the spectroscopic metric adversely due to the limited inter-particle distance that is usually below the axial resolution limit of the OCT system (Table 5-1). The DWDB metric becomes inaccurate in relating to particle sizes when this happens. We observed in the spectroscopic metric calibration experiments that when using particles smaller than 0.5 μm, the metric values become more indicative of larger particles, similar to the results that Adler et al. reported [115]. However, we observed a threshold inter-particle spacing value that corresponds to stable spectroscopic metric values which occurs when particle concentrations are sufficiently low to have inter-particle distances that is above the axial resolution of the OCT system. In this work, particles that fall into this category are above 0.5 μm in size. This is part of the reason

why the particle sizes of 0.5, 1, 10, 25 and 45 μm were used to calibrate the spectroscopic metrics shown in this work.

Simulation of the spectral interference fringes resulting from various scatterer sizes was performed to verify and understand the microsphere results. The spectral interference fringes obtained for microsphere sizes of 0.5–45 μm using a 840 nm center wavelength light source with 40 nm bandwidth are shown in Figure 5-8a. It can be seen in Figure 5-8a that the frequency of the interference fringes increases with scatterer size. Scatterer sizes that are smaller than the theoretical axial resolution of about 10 μm do not exhibit interference fringes due to the limited spectral bandwidth of the light source. The calculated autocorrelation functions of the spectral interference fringes for various scatterer sizes are depicted in Figure 5-8b. It can be observed that the autocorrelation functions of large scatterers exhibit oscillatory features near the peak positions. This can cause the DB metric values to change in a nonlinear manner with scatterer size.

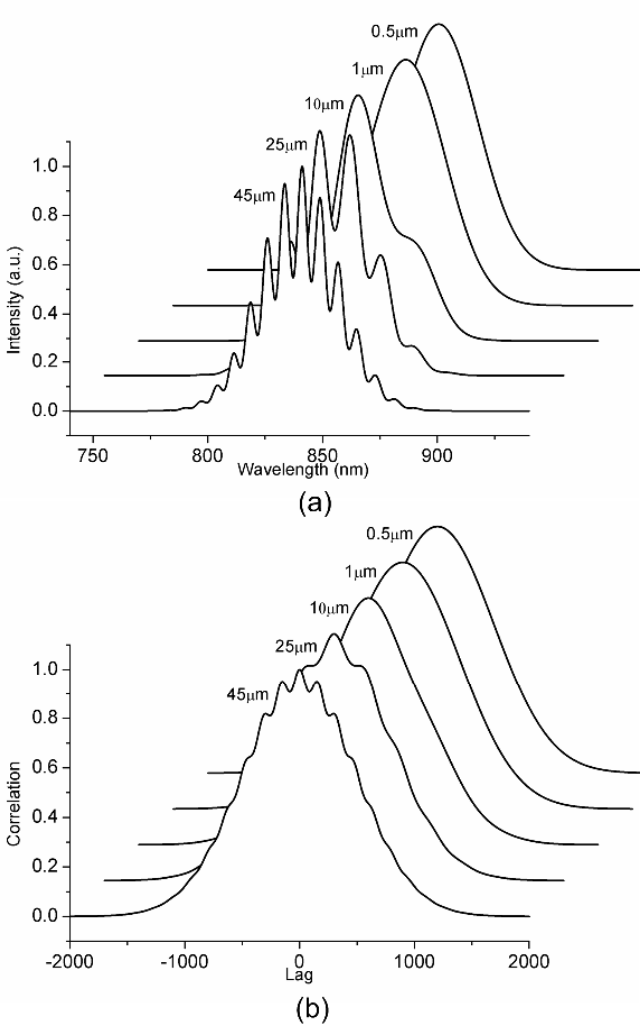

Figure 5-8: Simulated (a) OCT spectral profiles and (b) autocorrelation functions for scatterer sizes of 0.5–45 μm. The center wavelength and bandwidth of the light source are 840 nm and 40 nm, respectively.

The simulated DWDB metric values for the 840 nm center wavelength, 40 nm bandwidth light source are presented in Figure 5-9a. White Gaussian noise with SNR of 15 dB is added to the wavelength scattering spectra to mimic the experimental measurement conditions. A linear relation is observed for scatterer sizes in the range of 5–32 μm. Beyond a scatterer size of ~32 μm, the simulated DWDB metric is found to dip before leveling off a constant value. The simulated DWDB metric also did not show any

noticeable change for scatterer sizes below 5 μm due to limited bandwidth of the light source. This indicates that subtle changes in the spectral modulation are still detectable via the DWDB metric for scatterer sizes down to half the axial resolution. The smallest resolvable scatterer size in tissue with the DWDB metric is therefore 3.57 μm using the FD-OCT system developed in this work. The experimentally measured DWDB metric, included in Figure 5-9a for comparison, is found to be in broad agreement with the simulated results. The dip in the metric value at a scatterer size of ~35 μm was not experimentally observed since microsphere around this size was not measured.

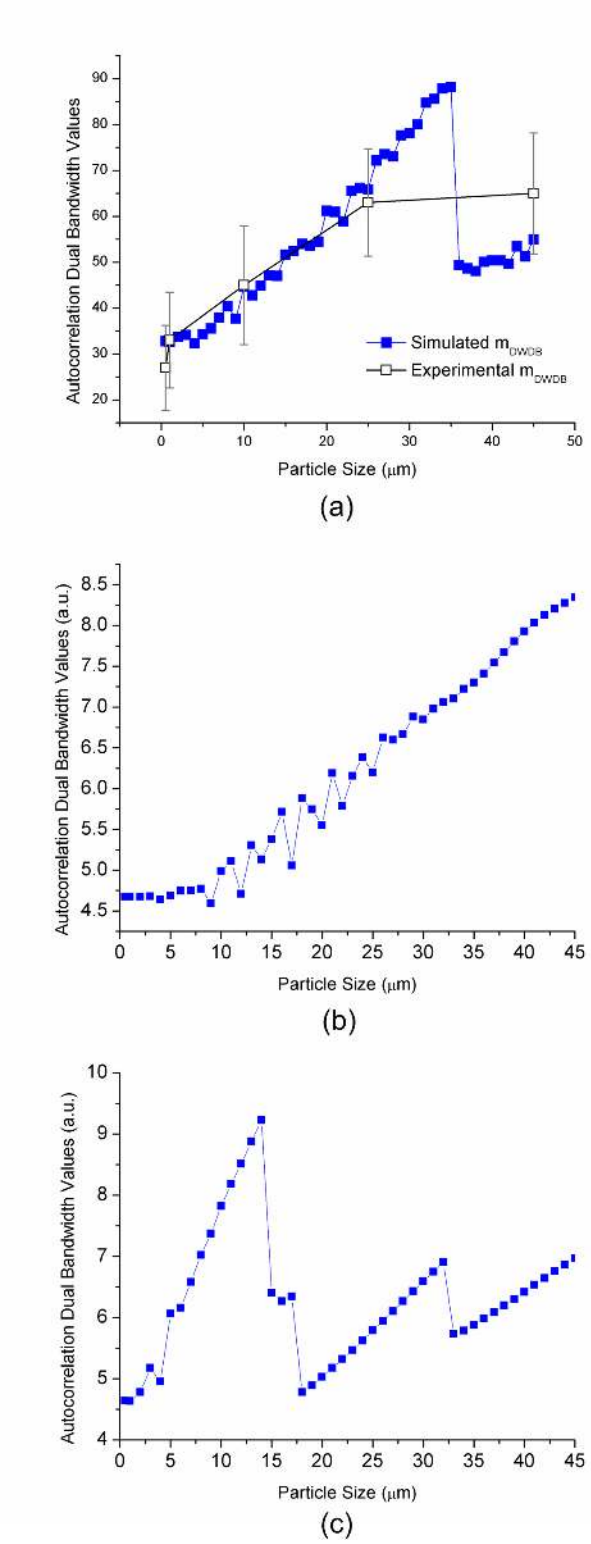

Figure 5-9: Simulated DWDB values for 840 nm center wavelength light sources with bandwidth of (a) 40 nm, (b) 20 nm and (c) 80 nm. The measured DWDB values are included in (a) for comparison.

To appreciate the influence of the light source bandwidth, DWDB metric values from 840 nm center wavelength light sources with bandwidths of 20 nm and 80 nm are also calculated and shown in Figure 5-9b and Figure 5-9c, respectively. With the smaller bandwidth light source, the DWDB metric did not exhibit any change for scatterer size of less than ~10 μm although the linear change is found to extend to the largest simulated scatterer size of 45 μm. For the 80 nm bandwidth light source, the smallest detectable scatterer size improves to 2 μm but the linearity with scatterer size is limited to a maximum scatter size of ~14 μm. The DWDB metric is observed to undergo sawtooth oscillations beyond a scatter size of 14 μm. This is attributed to the appearance of high frequency side-lobes in the spectral autocorrelation profiles of large scatterers which can affect the linearity of the metric values. These simulation results show that there is a trade-off between the smallest detectable scatterer size and the maximum scatterer size in the linear range of the DWDB metric. Consequently the OCT light source has to be appropriately selected to suit specific SOCT applications. Alternatively this trade-off can potentially be overcome by using a suitably large bandwidth light source to detect the smallest scatterer size and subsequently digitally limiting the light source bandwidth to achieve the desired linear monotonic range for quantifying the large scatterers.

The DWDB spectroscopic metric was evaluated by imaging two tonsil tissue samples and differences in scatterer size in the samples are clearly differentiated in the corresponding spectroscopic images. The enhanced contrast in scatterer size differentiation achieved in the DWDB spectroscopic images is attributed to the use of an optimized DB metric determined from DW autocorrelation profiles with concurrently good spatial and spectral

resolutions. The improved contrast enhancement achieved with the DWDB technique has potential applications in the identification of abnormal changes in bulk material or tissue. For instance, oral carcinogenesis is accompanied by normal cells undergoing cellular changes where the cell nucleus expands by almost 50% with little to no cytoplasm remaining [28-31] and malignant cells multiplying in the basal membrane of the mucosal tissue [32-33] between the epithelium and lamina propria, a thin layer of loose connective tissue beneath the epithelium. The morphometric parameters of basal cell in different oral carcinogenesis stages was investigated using histological methods and the basal cell nuclear diameters of normal and squamous cell carcinoma (SCC) were found to be 7.17±0.73 μm and 10.28±0.9 μm, respectively, an increase of about 40% [30]. Normal and cancerous rat colon cell nuclear diameters were found to be 5.15±0.05 μm and 7.23±1.21 μm, respectively [39], a similar increase of about 40%. Such abnormalities in the form of an enlarged cell nucleus or abnormal dense cluster compared to the surrounding cells can easily be detected using the proposed DWDB technique.

The relative sizes of the primary and secondary window for the DW method affects scatterer size differentiation. The ratio of secondary to primary window size used in literature is of a value of 14–16 [117, 135]. The primary and secondary window sizes were varied and a ratio of 8 is found to significantly reduce computation time while achieving reasonably good scatterer size differentiation. The choice of the secondary window size is important, especially in multi-layered tissue media. If the secondary window is too large, the resulting local spectral modulations extracted could contain scatterer information from multiple layers, thereby reducing the spatial resolution.

Therefore a suitably selected secondary window size is necessary to maintain good spatial resolution.

5.5 Summary

The autocorrelation bandwidths of DW *k*-space OCT scattering profile of 0.5 μm to 45 μm microspheres and their correlation to scatterer size were investigated. A DB spectroscopic metric defined as the ratio of the 10% to 90% autocorrelation bandwidths gave the best contrast enhancement for scatterer size differentiation in the resulting spectroscopic image. The DWDB metric is found to exhibit a monotonic change with microsphere size. Simulation of the DWDB metric supports the experimental results and revealed a trade-off between the smallest detectable scatterer size and the maximum scatterer size in the linearity range of the DWDB metric, which depends on the choice of the light source optical bandwidth. Spectroscopic images of polystyrene microspheres and tonsil tissue samples based on the proposed DWDB metric showed clear differentiation between different-sized scatterers as compared to those determined with conventional STFT-calculated metric. Differences between connective tissue, epithelial and lymphoid cells, as well as between the upper and lower epithelium cells, of tonsil tissues are clearly observed in the SOCT images. The DWDB metric greatly improves the contrast in SOCT imaging and can aid the visualization of abnormal cell distribution in biological tissues and samples. Potential applications include the early detection of cell nuclear changes in tissue carcinogenesis, the monitoring of healing tendons and cell proliferation in tissue scaffolds.

Chapter 6 Monitoring the Effect of Bone Marrow-Derived Mesenchymal Stem Cells on Flexor Tendon Healing with SOCT

6.1 Introduction

6.1.1 Background

Morphologically, the tendon is a complex composite material consisting of collagen fibrils embedded in an extra-cellular matrix (ECM) of proteoglycans. Proteoglycans are proteins that form a major component of mammalian ECM which can be used as raw material to form collagen. The collagen fibrils are closely packed, highly ordered parallel bundles (Figure 6-1a). Collagen is a birefringent biological material due to its molecular structure [49], which shows up as bright bands in polarization microscope images (Figure 6-1b). Tendons have a relatively low concentration of cells. Fibroblasts, the predominant cell type within tendons, are arranged in the spaces between the parallel collagen bundles. As shown in Figure 6-1c, the cell bodies are rod- or spindle-shaped and oriented in rows when seen microscopically in a longitudinally derived section. Fibroblasts when not engulfed by tissue have a branched cytoplasm surrounding an elliptical nucleus. Human fibroblast cell nuclei have a transverse size of about 50 μm and an axial size of about 20 μm [178], as depicted in Figure 6-2.

The major constituent of tendon is type I collagen (86% fat-free dry weight). Collagen molecules are made up of 3 collagen chains in a triple-helix structure. In this way, collagen molecules combine to form ordered units of microfibrils (5 collagen molecules), subfibrils, and fibrils (Figure 6-3). These units are arranged in closely packed, highly ordered parallel bundles that are oriented in a distinct longitudinal pattern, with

proteoglycans in association with water incorporated in an ECM, binding the fibrils together to form fascicles. At the fascicle level, the collagen bundles form a distinctive wavy- pattern called crimps.

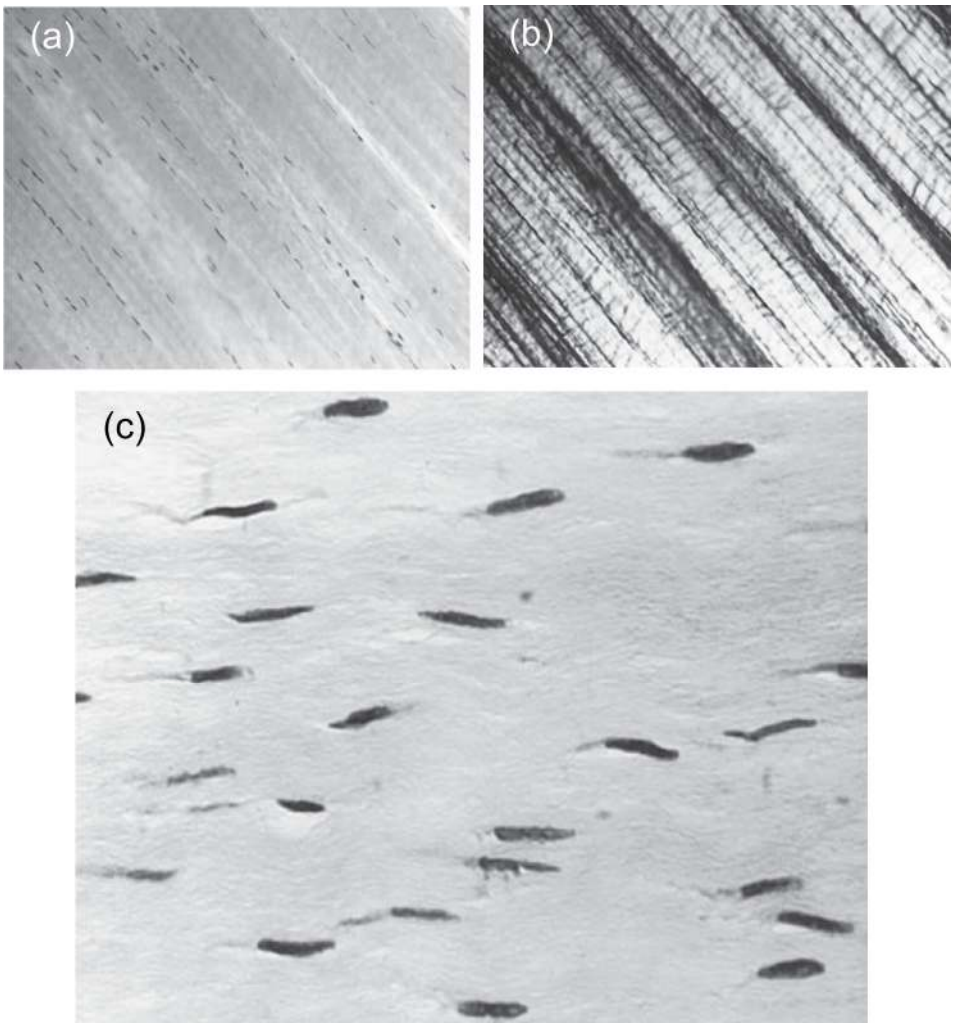

Figure 6-1: H&E stained histological section of a human flexor tendon. (a) Brightfield and (b) polarization microscope images reveal parallel rows of fibroblasts lying between collagen bundles (100× magnification). (c) Magnified section showing the spindle-shaped fibroblasts (250× magnification) [140].

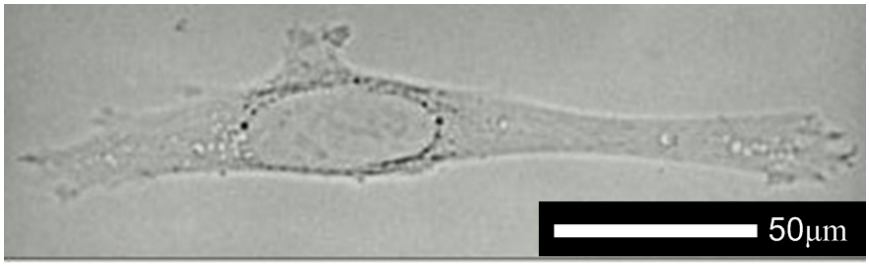

Figure 6-2: Bright-field microscope image of a human fibroblast cell [178].

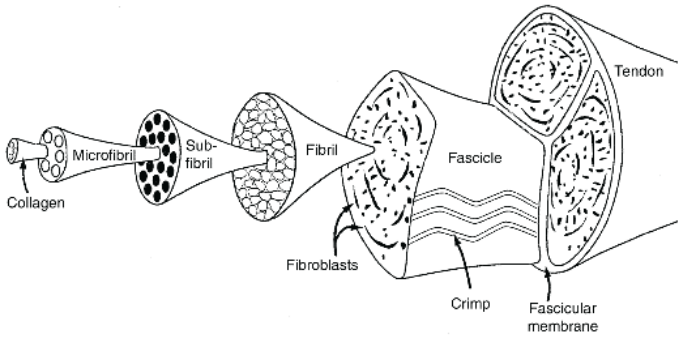

Figure 6-3: Schematic representation of the micro-architecture of a tendon [140].

The fascicles within the tendon are bound together by loose connective tissue, the endotenon, which permits longitudinal movement of collagen fascicles and supports blood vessels, lymphatics and nerves. Tendons typically carry tensile forces. Tendons that bend sharply, such as flexor tendons of the hand, are enclosed by a tendon sheath that acts as a pulley and directs the path of the tendon. A protective layer of disorganized collagen called the epitenon covers the surface of the tendon and the sliding of the tendon is assisted by synovial fluid.

Surgery is usually needed to suture severed tendons back together, as they cannot heal unless the cut ends of the tendons are touching. During the healing process, fibroblasts

use raw materials in the surrounding matrix to rebuild the collagenous structures within the tendon. Tendon healing involves an inflammatory phase from 48 to 72 hours after suture repair, a fibroblastic- or collagen-producing phase from 5 days to 4 weeks, and a remodeling phase that continues until approximately 112 days (16 weeks). During the inflammatory phase of tendon healing (week 1) (Figure 6-4) the strength of the repair is almost entirely imparted by the suture itself with a modest contribution from the fibrin clot between the tendon ends. The laceration site is filled with cells that originate from extrinsic tissue, the epitenon, and the endotenon. The cells proliferate, and their function is largely to devour cell debris and the synthesis of new collagen. At 3 weeks (Figure 6-4) there is marked fibroblastic proliferation from the endotenon and epitenon, and these fibroblasts participate in both synthesis and resorption of collagen. The fibroblasts and collagen are in a plane perpendicular to the long axis of the tendon and revascularization (formation of blood vessels) increases at the repair site, including penetration of the former non-vascularized zones by a new vessels. At 8 weeks (Figure 6-4) the collagen is mature and realigned in a linear fashion. Adhesions are stimulated both by the initial trauma to the tendon and sheath, and by immobilization.

Many studies have been conducted to improve tendon healing and accelerate the rate of recovery. Research include tendon tissue scaffolds for seeding of tenocytes and eventual implantation [146-147], acellularized (removal of cells) and reseeded tendon constructs to increase mechanical strength and biocompatibility [179], addition of growth factors to assist in tenocyte proliferation [180] and the use of mesenchymal stem cells (MSCs) to

increase tendon healing rate [22, 181-182]. Many adult tissues contain populations of stem cells that have the capacity for renewal after trauma, disease or aging [183].

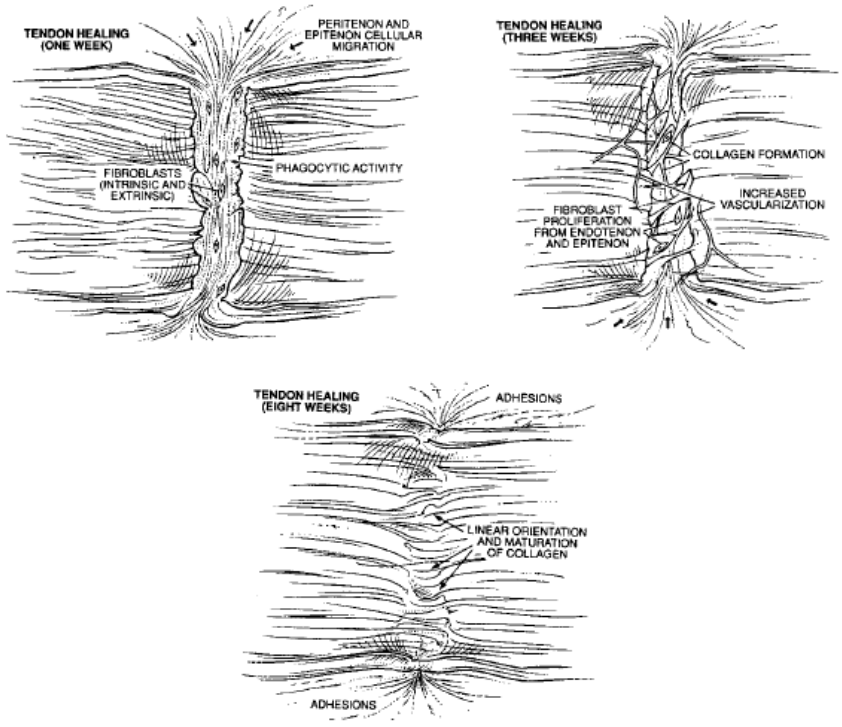

Figure 6-4: The biological sequence of tendon healing [171]. (Top left) Tendon healing at 1 week. (Top right) Tendon healing at 3 weeks. (Bottom) Tendon healing at 8 weeks.

The adult bone marrow contains MSCs which contribute to the regeneration of mesenchymal tissues such as bone, cartilage, muscle, ligament, tendon, adipose and stroma (Figure 6-5). MSCs can be derived from the host (autologous) or derived from external donors of the same species (allogeneic). Allogeneic MSCs have been found to perform similarly to autologous MSCs [184], and most importantly, no adverse host immune response was detected after implantation [185-186]. The significance of this is that an allogeneic MSCs can be isolated from any donor, grown, and cryopreserved, providing a readily available source of cells for clinical use. Furthermore, the allogeneic

MSCs can be introduced into another host without the use of immunosuppressive therapy.

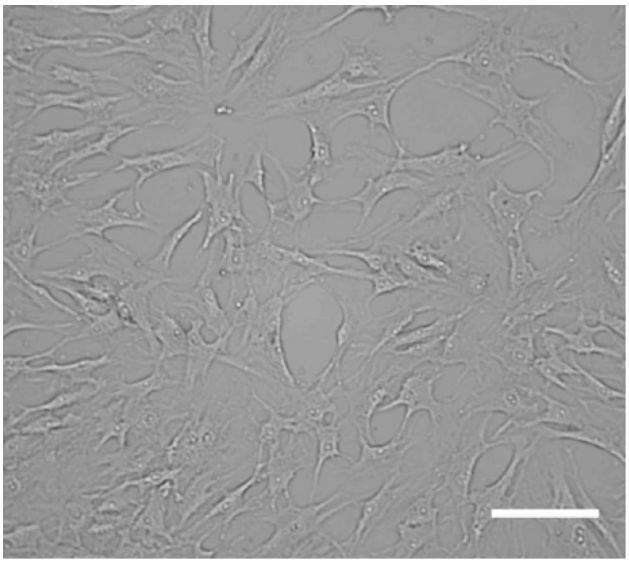

Figure 6-5: Phase contrast light microscope image of human MSCs, which are spindle shaped, fibroblast-like cells [186]. Scale bar represents 50 μm.

In clinical practice, tendon rupture or laceration requiring primary surgical repair is more commonly encountered than defects requiring grafting of a tissue-engineered construct [22]. Thus, the direct control of tendon healing rate at the injury site is important, and the direct introduction of MSCs to the injured tendon is efficacious in terms of tendon healing rate and high proliferation speed in culture without senescence (biological aging) [22, 181-182]. In MSC assisted tendon healing studies, bright-field microscopy is used for imaging tissue sections [22]. Cellular morphology and tissue features can be observed clearly, aided by appropriate tissue stains. However, the histological assessment process is time consuming and above all, destructive. As such, the monitoring of the healing process of the same tendon over a certain time period is not possible.

6.1.2 Motivation

In early tendon imaging, conventional OCT has been used to study the optical characteristics of tendons [144-145, 162]. Vertical and horizontal banding patterns were observed from TD-OCT images of sheep tendons [162]. The horizontal bands in the OCT images were observed to be polarization-dependent and they were attributed to collagen birefringence due to the crimp of the fibril. The vertical banding was attributed to the structural organization of the tendon and the vertical crimps were found to gradually disappear when strain is applied to the tendons. In a subsequent work, TD-OCT [144] was used to visualize and determine how crimp period changes as a function of applied tensile strain in rat tail tendon fascicles. The vertical crimp period was found to increase nonlinearly with strain. The physical origin of the crimp pattern was suggested to be strong reflections from the crests and troughs of the crimp waveform in the tendon. Tissue microstructure and birefringence in pig tendons, when monitored with conventional OCT, also show up as horizontal and vertical bands in the OCT images [145].

The most recent research focuses on PS-OCT to extract phase information from birefringent tissue samples like tendons or ligaments [106-107, 111, 147, 187]. Optical properties of the sample such as phase retardation, birefringence, Stokes vector and Jones vector, can be extracted from careful measurement of vertical and horizontal polarization states of backscattered light from a sample. Human tendons were imaged in a study using a PS-OCT system [111] and normal tendons with organized collagen were found to exhibit birefringence bands. All ruptured tendons were found to be highly scattering

while some do not exhibit birefringence bands. Vertical crimp patterns observed in the OCT images were found to be insensitive to input polarization. This was also attributed to changes in the scattering angles generated by the micro-structural wavy shape of the collagen bundles. By contrast, there has not been any work done on monitoring the recovery phase in tendon healing using OCT or SOCT. The DWDB-SOCT technique developed in chapter 5 can potentially be used to monitor the tendon healing process over a time period with cell type differentiation.

The monitoring of the effect of bone marrow derived mesenchymal stem cells (BMSCs) on healing flexor tendons in a rabbit model using the DWDB-SOCT technique is presented in this chapter. BMSCs possess spindle-shape morphology similar to fibroblasts [11], making it very difficult to tell them apart even through histology, except when immunohistochemistry is used. SOCT can provide additional information on the distribution of fibroblast cells and BMSCs within the injured tendon region based on the differentiation of cell nuclei sizes and the surrounding collagen matrix. Four different tendon seeding groups based on the types and quantity of stem cells introduced to the injury site, namely TISSEEL control (fibrin glue), 1 million (1M) autologous BMSCs, 1M allogeneic BMSCs and 4 million (4M) allogeneic BMSCs, are established for comparison. The distribution of fibroblasts at the injury site for flexor tendons at 3 and 8 weeks healing time points were observed in the DWDB-SOCT images. These time points are chosen to coincide with the fibroblastic proliferation and the collagen remodeling phases of the healing process, respectively. Histological images of a healing tendon at 3 weeks are also presented to highlight important details. Quantitative analysis of fibroblast

concentration at the injury site were performed and the results showed that the BMSCs are effective at promoting tendon healing in the early stages.

6.2 Materials and Methods

6.2.1 Bone Marrow-Derived Mesenchymal Stem Cells

BMSCs are obtained from anesthetized rabbits by means of bone marrow aspiration from the iliac crest, and processing is performed as described by Chong *et al.* [22]. The aspirate is mixed with bone marrow-derived mesenchymal stem cell growth medium (ratio, 1:2) consisting of Dulbecco's modified Eagle medium (DMEM; Sigma, St Louis, Missouri), 1% penicillin-streptomycin (Sigma) and 10% fetal bovine serum (HyClone, Logan, Utah). The samples are washed twice with medium and were centrifuged at 2000 rpm for five minutes. The supernatant is discarded, and the resulting cell pellet is resuspended with medium to make up 15 mL and was subsequently plated onto T-75 culture flasks. Cells are grown in an incubator at 37°C, humidified with 5% CO_2. After five days, the contents of the flask are removed and washed with medium, leaving behind BMSCs that adhered to the bottom of the flask. Once confluent, the BMSCs are detached using trypsin and serially subcultured. Second passage cells are used for implantation. Cells isolated with this technique have a fibroblast-like appearance and have been shown to be capable of multipotent differentiation [183, 188].

6.2.2 Rabbit Model

Female New Zealand white rabbits (weight of 2.5–3 kg) are used under the guidance of the Institutional Animal Care and Use Committee and with approval of our institutional

review board. The animals are anesthetized with a combination of an intramuscular ketamine (50 mg/kg) and xylazine (10 mg/kg). 2.5 ml 1% xylocaine was administered on both rear paws as local anesthesia. Under aseptic condition, a small longitudinal incision is made over the index finger and ring finger of the paws. The skin and subcutaneous tissues are retracted to expose the flexor tendons. The flexor digitorum profundus equivalent tendon in the middle of zone II is completely divided using a surgical blade. Both tendons are repaired with a Prolene 5/0 suture under loupe magnification using a modified Kessler's repair, as shown in Figure 6-6a. Proximally, the tendon is divided at the common tendon origin to unload the repair. One of the two digits is randomly assigned to receive BMSC treatment with 100 µl TISSEEL (Baxter, Singapore) as mounting medium and the remaining digit serves as control with just TISSEEL. In order to monitor the effect of BMSCs on flexor tendon healing, 4 different seeding groups based on the types and quantity of stem cells introduced to the injury site, namely fibrin glue control, 1M autologous BMSCs, 1M allogeneic BMSCs and 4M allogeneic BMSCs are used for comparison. The infusion of the BMSC solution to the tendon repair site is illustrated in Figure 6-6b. The BMSC solution is left to set for two minutes in the repair site before wound closure (Figure 6-6c). The tendon sheath is left unclosed and the skin wound is closed. After surgery, the animals are allowed to move around unhindered within the cage and fed *ad libitum*.

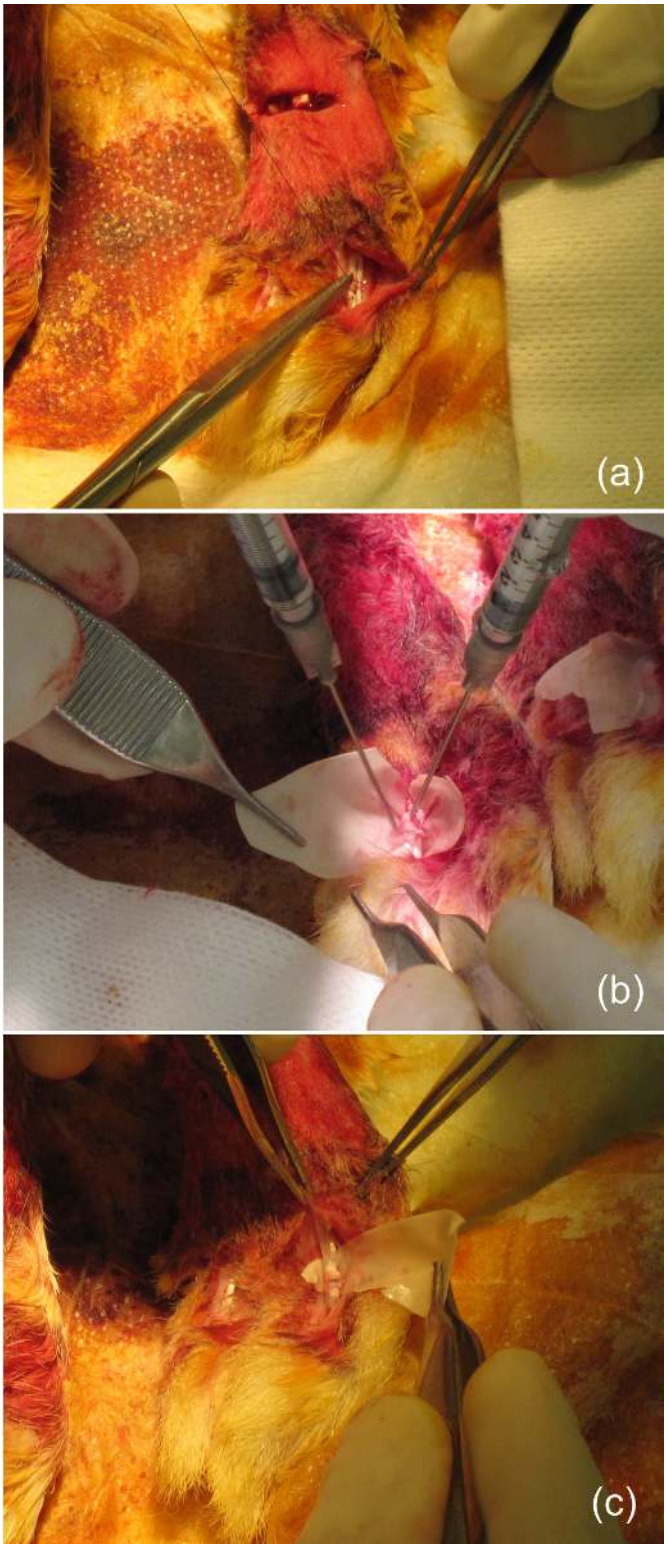

Figure 6-6: Flexor tendon surgery. (a) Suturing of an injured tendon on a rabbit's paw. (b) Infusion of BMSC solution to tendon repair site. (c) Post-infusion of BMSC solution, prior to closure of wound.

6.2.3 Tendon Imaging

There are two time points for harvesting the rabbit flexor tendons for *ex vivo* imaging, one at 3 weeks and the other at 8 weeks. These time points are chosen to coincide with the fibroblastic proliferation and the collagen remodeling phases of the healing process respectively. At each time point, the rabbits were sacrificed and the flexor tendons were surgically excised for analysis. A normal flexor tendon with the finger attached on the right side is shown in Figure 6-7a. A repaired flexor tendon surgically sutured back together is shown in Figure 6-7b, where the blue suture thread compresses the severed ends together. Figure 6-7c shows a BMSC seeded flexor tendon at 3 weeks and a translucent tissue covering the injury site is observed. At 8 weeks, the translucent tissue is still present but the section is not clearly visible when the tendon is wet (Figure 6-7d).

A $6.5\times1\times2$ mm^3 imaging volume of the sutured joint is taken *ex vivo* with the FD-OCT system described in chapter 4. The measurement data is recorded as raw B-scan spectral information and is processed using custom Matlab programs to obtain both OCT and spectroscopic images. After imaging, the OCT line scan region of a normal tendon is marked with two microinjections of ink before sending it for routine histological processing. Multiple 5 μm thick tissue sections are obtained from the marked region and stained with H&E. Bright field and polarization images of the normal tendon sections are taken digitally using a standard microscope with crossed polarizers. Minor discrepancies between histology and OCT images are attributed to tissue fixation, processing, and sectioning artifacts.

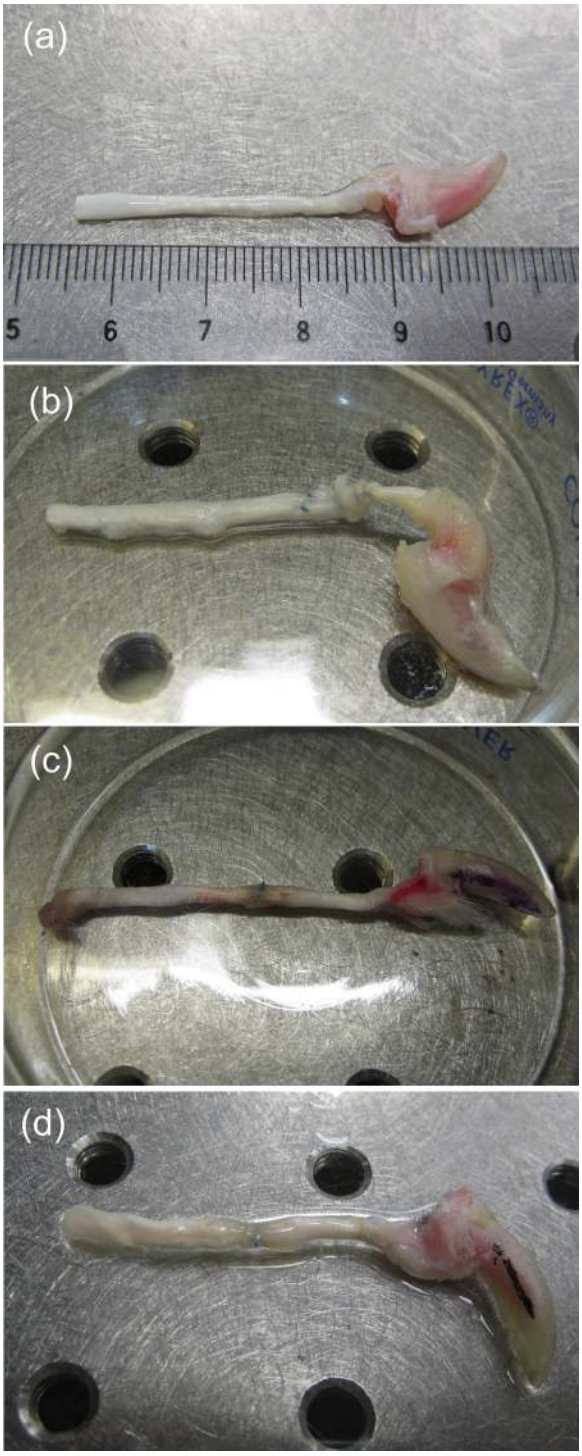

Figure 6-7: (a) Normal flexor tendon. (b) Repaired flexor tendon with no cell seeding. (c) BMSC seeded healing flexor tendon at 3 weeks. (d) BMSC seeded healing flexor tendon at 8 weeks.

6.3 Results

6.3.1 Repaired Flexor Tendon Histology

The H&E stained bright-field and polarization images of the healing flexor tendon sample at the 3 week time point are shown in Figure 6-8. Figure 6-8a shows the bright-field image of the H&E stained tendon section. The center portion of the tendon was injured and healing took place in region *i*. The healing tendon section in region *i* shows up as predominantly blue-purple in the bright-field image due to the high concentration of fibroblasts, whose nuclei are stained by haemotoxylin. The interface between the healing and normal tendon sections is marked as region *ii*. Region *iii* comprises of organized collagen, stained pink, in the uninjured part of the tendon. The holes in the tendon caused by the suture thread holes show up as oval puncture voids in the histological section.

The corresponding polarization image of the tendon section is depicted in Figure 6-8b. A marked difference between the normal and healing sections is observed. The highly organized collagen in the normal section shows up as light and dark bands in the polarization image due to their optical anisotropy. By contrast, the healing section is rich in fibroblasts but deficient in organized collagen. Consequently, this section appears as a dark region in the polarization image.

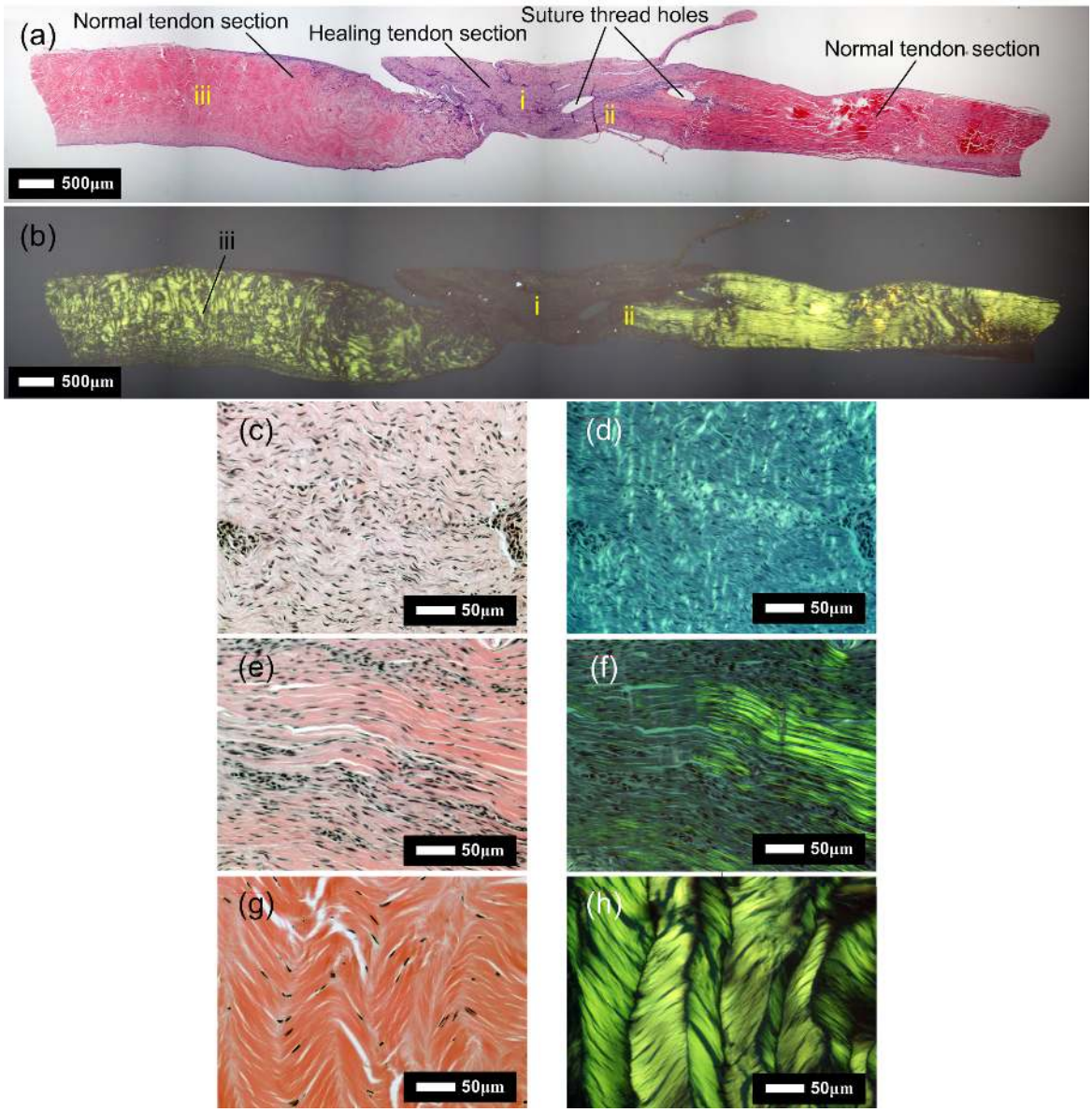

Figure 6-8: Flexor tendon histology at 3 week healing time period. (a) Bright-field image of flexor tendon section. Regions *i–iii* are the healing, healing interface and normal tendon sections respectively. (b) Polarization image of flexor tendon section. (c) Bright-field and (d) polarization images of healing tendon section in region *i*. (e) Bright-field and (f) polarization images of healing interface tendon section in region *ii*. (g) Bright-field and (h) polarization images of normal tendon section in region *iii*.

Normal tendons typically contain a very low concentration of fibroblast cells. In the early stages of tendon healing after injury, the density of fibroblast cells is the highest at the injured region and the number drops significantly during the collagen remodeling phase.

Figure 6-8c, e and g show the magnified bright-field H&E stained tendon sections at regions *i*, *ii* and *iii*, respectively, while the corresponding polarization images are depicted in Figure 6-8d, f and h. It can be seen in Figure 6-8c that fibroblast proliferation is dominant and there is a high cell concentration at the healing site synthesizing and re-absorbing collagen. The fibroblast cells are spindle-shaped with an elliptical nucleus, and the cell nuclei have transverse sizes of 7–20 μm and axial sizes of 4–7 μm. There are local pockets of collagenous organization (small bright regions in Figure 6-8d) but the concentration remains low.

The collagen remodeling and reorganization phase shows moderately high concentrations of fibroblasts in certain bands of the tendon (Figure 6-8e). The center band in the bright-field image is observed to have a much lower cell concentration and the corresponding location in the polarization image of Figure 6-8f shows up as a bright band. This indicates that the center band has completed the remodeling of collagen. The normal tendon section in region *iii* (Figure 6-8g) has highly organized collagen forming a wavy crimp pattern which shows up clearly in both the bright-field and polarization images. Only a very small number of fibroblasts are found between the collagen fibrils of normal tendon.

6.3.2 Spectroscopic Imaging of Repaired Flexor Tendon without Cell Seeding

OCT and DWDB-SOCT images of a normal flexor tendon in Figure 6-9 is obtained to compare the features. Tendon crimp patterns of bright and dark bands are clearly observed in the OCT image in Figure 6-9a, showing the organization of the collagen in the tendon fascicle. The epitenon sheath comprising of unorganized collagen shows up as

a distinct thin layer on the tendon surface. The bundled collagen fibrils that make up the tendon form the "scaffold" that provides the mechanical support for the ECM and the fibroblast cells that reside within the tendon. The other biological scatterer of interest is the fibroblasts present in the tendon at the injury site. The size of rabbit fibroblast nuclei measured from histology ranges from 7–20 μm in length and 4–7 μm in thickness.

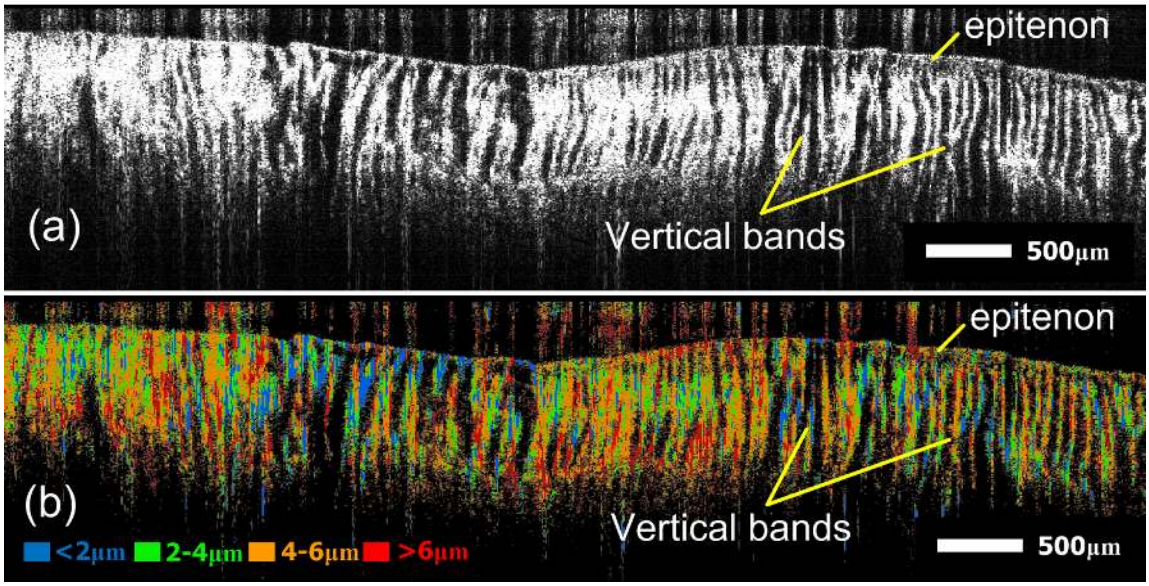

Figure 6-9: (a) Conventional intensity-based OCT and (b) DWDB-SOCT images of a normal flexor tendon at rest.

The DWDB-SOCT image shown in Figure 6-9b is obtained by setting the scatterer differentiation threshold such that scatterers with size of <2 μm, between 2–4 μm, between 4–6 μm and >6 μm are colored blue, green, orange and red, respectively. Scatterers larger than 4 μm in size (orange and red pixels) are considered large scatterers while small scatterers refer to those with a size of less than 4 μm (blue and green pixels). Since the tendons are imaged axially, the thickness of the fibroblast nuclei will determine

its scatterer sizing and a reference size value of 4 μm is used to differentiate fibroblasts (large scatterers) from collagen (small scatterers).

The DWDB-SOCT image shows a mix of mostly orange and red hues in Figure 6-9b, indicating the presence of large scatterers. This is a surprising result as the collagen within a normal tendon should show up as small scatterers in the SOCT image due to the low concentration of fibroblasts. This can be attributed to the dense packing of the collagen fibrils within the tendon to give high mechanical strength. In densely scattering samples, high particle/scatterer concentrations affect the spectroscopic metric adversely when the inter-particle spacing is less than the axial resolution of the OCT system. In such cases, multiple hues are observed in the SOCT image and this is possibly the effect of multiple scattering due to densely packed collagen fibers. Spectroscopic analysis should be excluded from these sections.

A sutured flexor tendon at 0 weeks without cell seeding is imaged and shown in Figure 6-10a. Vertical bands are clearly seen on the left tendon section of the suture joint. A good suture repair ensures that the two severed ends of the tendons are in contact for compression on the suture joint. The vertical bands in the intensity-based OCT image reveal the direction of the compression force. The DWDB-SOCT image in Figure 6-10b shows that the distribution of large scatterers (>4 μm) is similar to that of normal tendon (Figure 6-9b). The epitenon layer is made up of unorganized collagen and is not densely packed. Therefore it appears as blue in the spectroscopic image, signifying small scatterers of <4 μm in size. In order to analyze the healing sections of repaired tendons, it

is necessary to set boundary conditions to exclude normal collagen external of the healing region and only analyze the scatterers within the healing region.

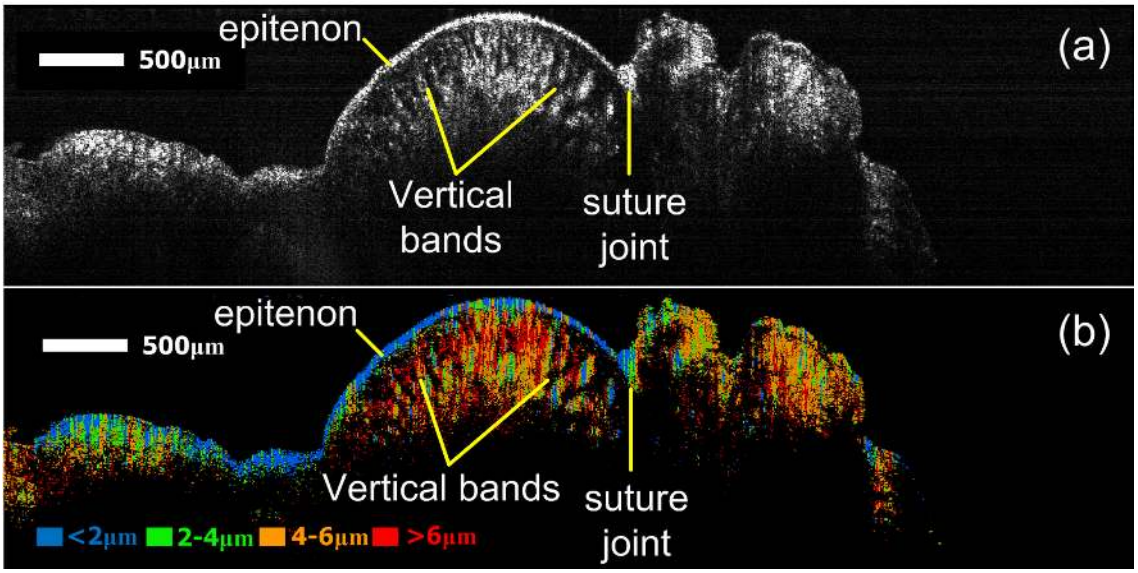

Figure 6-10: (a) Conventional intensity-based OCT and (b) DWDB-SOCT images of a repaired flexor tendon at 0 weeks with no seeding.

6.3.3 Spectroscopic Imaging of BMSC Seeded Flexor Tendons

A four million cell (4M) BMSC culture was grown, extracted and centrifuged to obtain a concentrated sample to serve as a control for spectroscopic imaging. The OCT image of the control in Figure 6-11a shows a uniformly scattering sample. The bright region on the sample surface is specular reflection from the scan beam. The DWDB-SOCT image in Figure 6-11b shows that the BMSC sample contains large scatterers of size >4 μm. The blue hue is an artifact caused by specular reflection off the sample. The size classifications of the stem cells are consistent with the axial size of the cell nuclei observed in histology.

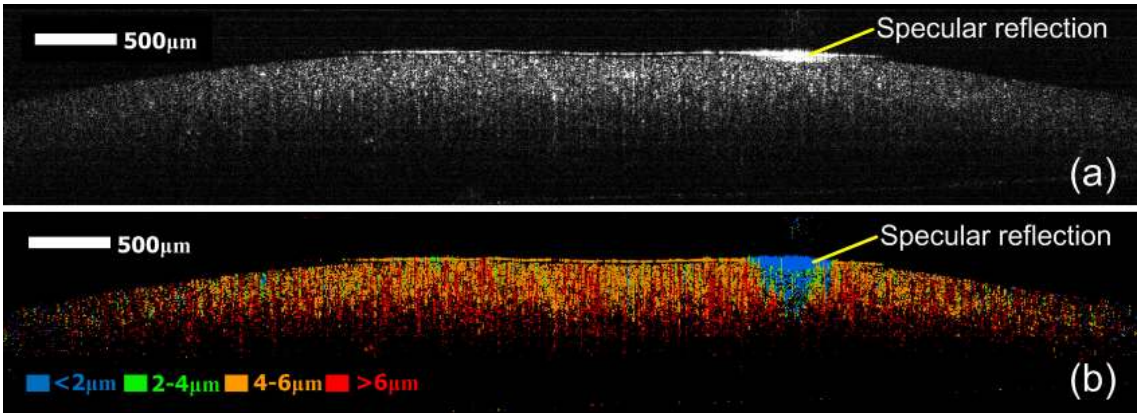

Figure 6-11: A concentrated sample of 4M BMSC (a) OCT image. (b) DWDB SOCT image.

Samples from each tendon seeding group at 3 weeks are imaged, and the intensity-based OCT and DWDB-SOCT images are presented in Figure 6-12 and Figure 6-13, respectively. The tendons are in the fibroblastic phase of healing when they are excised for imaging. The injury site is generally located in the center of the OCT image. The healing regions surrounding the injury sites are highlighted by yellow boxes in the images. Normal tendon sections are situated to the left and right sides of the healing region. The focus is on the healing region and the relevant section from each image is extracted and analyzed for the quantity of fibroblasts and BMSCs (represented by large scatterers of size >4 μm), and the quantity of remodeled collagen (represented by small scatterers of size <4 μm). At 3 weeks, there is significant fibroblastic proliferation at the injury site as well as collagen synthesis and resorption. A high concentration of large scatterers is therefore expected at the healing region, since synthesized collagen has not yet been organized to form dense bundles of collagen fibrils.

In the OCT images shown in Figure 6-12, organized collagen in normal regions gives a strong backscattered OCT signal compared to healing regions comprising new and unorganized collagen. Morphologically, the tendon images from each seeding group do not differ significantly in the OCT images. By contrast, the DWDB-SOCT images of each tendon seeding group in Figure 6-13 shows details like the formation of new collagen (blue and green, small scatterers) and the presence of fibroblast cells and BMSCs (orange and red, large scatterers). It is obvious that the healing region of each repaired tendon has substantial orange and red hue, suggesting significant fibroblastic activity.

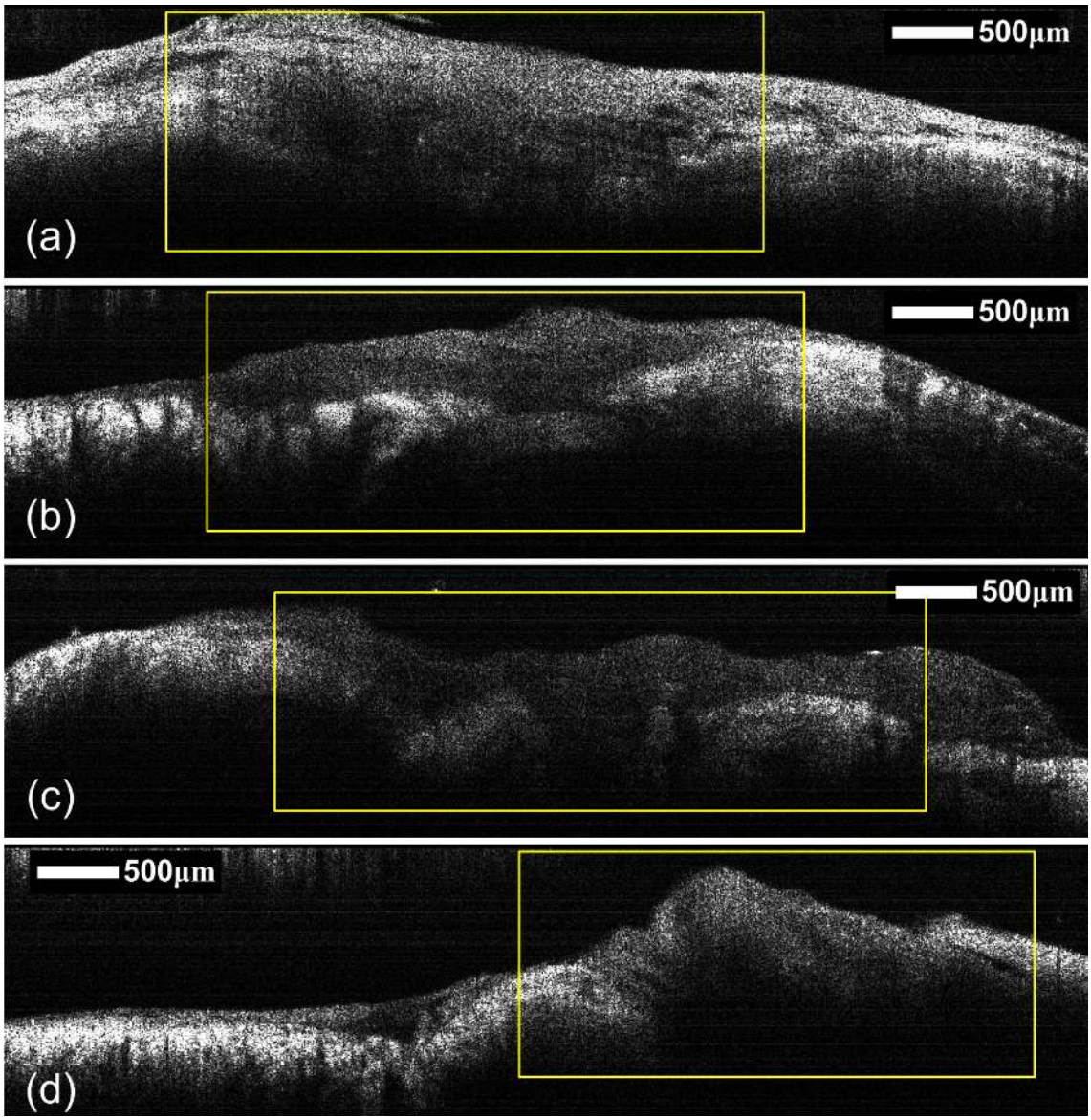

Figure 6-12: Intensity-based OCT images of (a) fibrin glue control, (b) 1M autologous BMSC seeded, (c) 1M allogeneic BMSC seeded and (d) 4M allogeneic BMSC seeded flexor tendons at the 3 weeks time point. Yellow boxes indicate tendon healing regions.

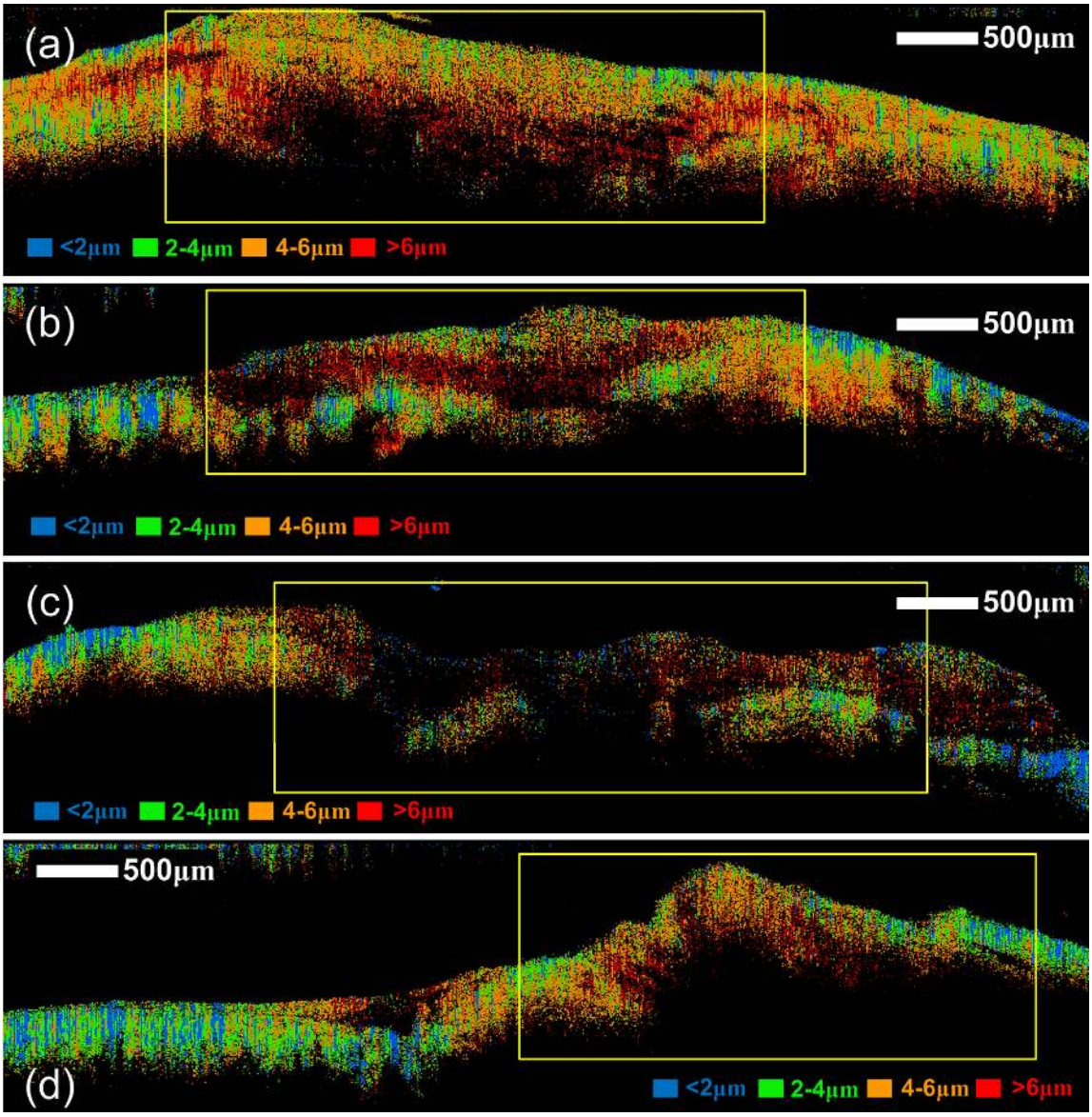

Figure 6-13: DWDB-SOCT images of (a) fibrin glue control, (b) 1M autologous BMSC seeded, (c) 1M allogeneic BMSC seeded and (d) 4M allogeneic BMSC seeded flexor tendons at the 3 weeks time point. Yellow boxes indicate tendon healing regions.

Samples from each tendon seeding group at 8 weeks are imaged, and the intensity-based OCT and DWDB-SOCT images are presented in Figure 6-14 and Figure 6-15, respectively. The tendons are in the collagen remodelling phase of healing when they are excised for imaging. During the collagen remodeling phase, the collagen produced in the previous phase is used to create large, organized bundles of collagen fibers. Thus, the

number of large scatterers (fibroblasts and stem cells) is expected to drop slightly or remain stable while the quantity of small scatterers (collagen fibrils) increases. Morphologically, no significant difference between the intensity-based OCT images of tendons at the 3 and 8 weeks and from among the tendon seeding groups at 8 weeks was observed. The DWDB-SOCT images in Figure 6-15, on the other hand, shows distributions of large scatterers (orange and red) within the healing region (yellow box) of each tendon seeding group corresponding to significant fibroblastic activity.

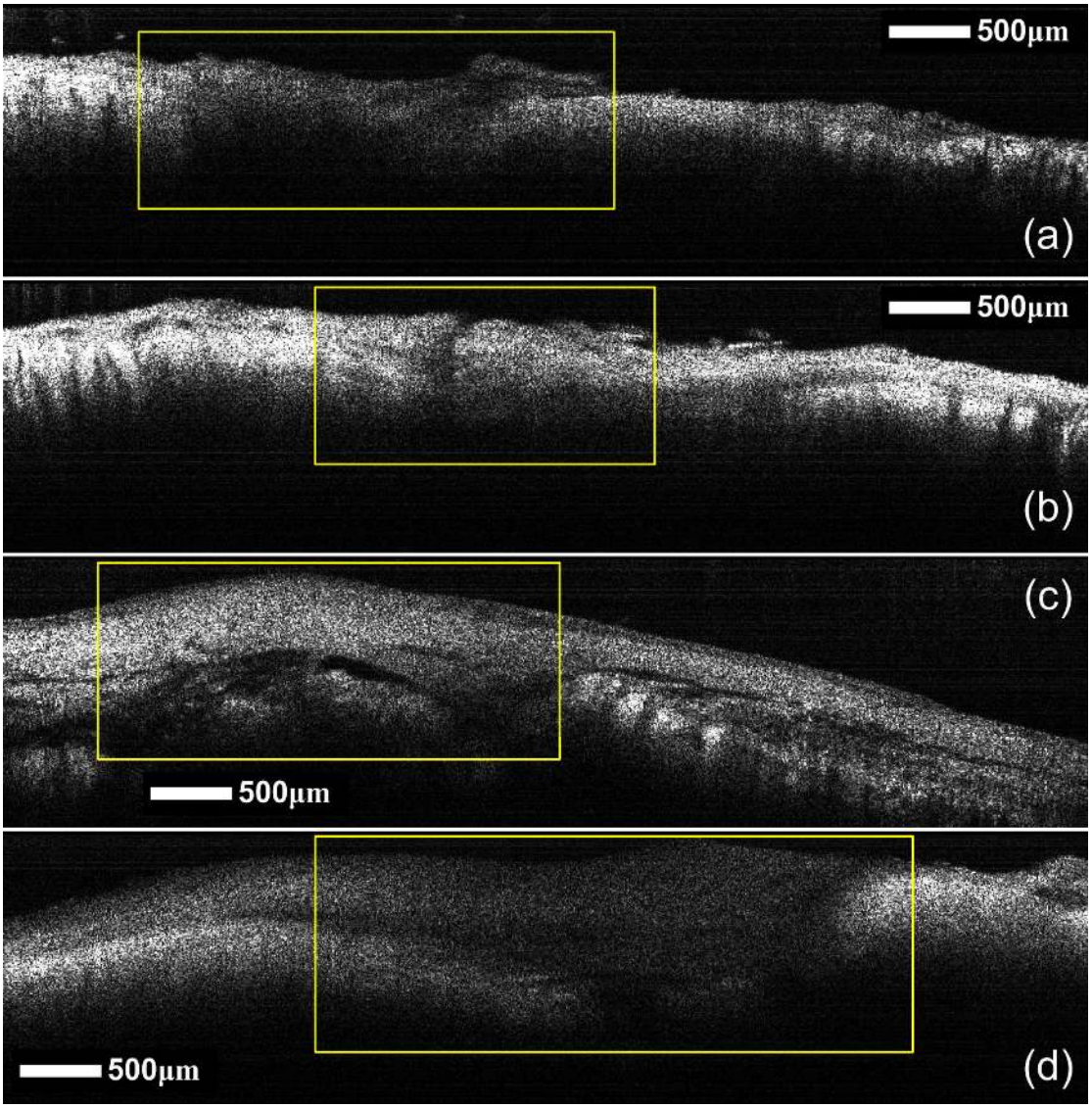

Figure 6-14: Intensity-based OCT images of (a) fibrin glue control, (b) 1M autologous BMSC seeded, (c) 1M allogeneic BMSC seeded and (d) 4M allogeneic BMSC seeded flexor tendons at the 8 weeks time point. Yellow boxes indicate tendon healing region.

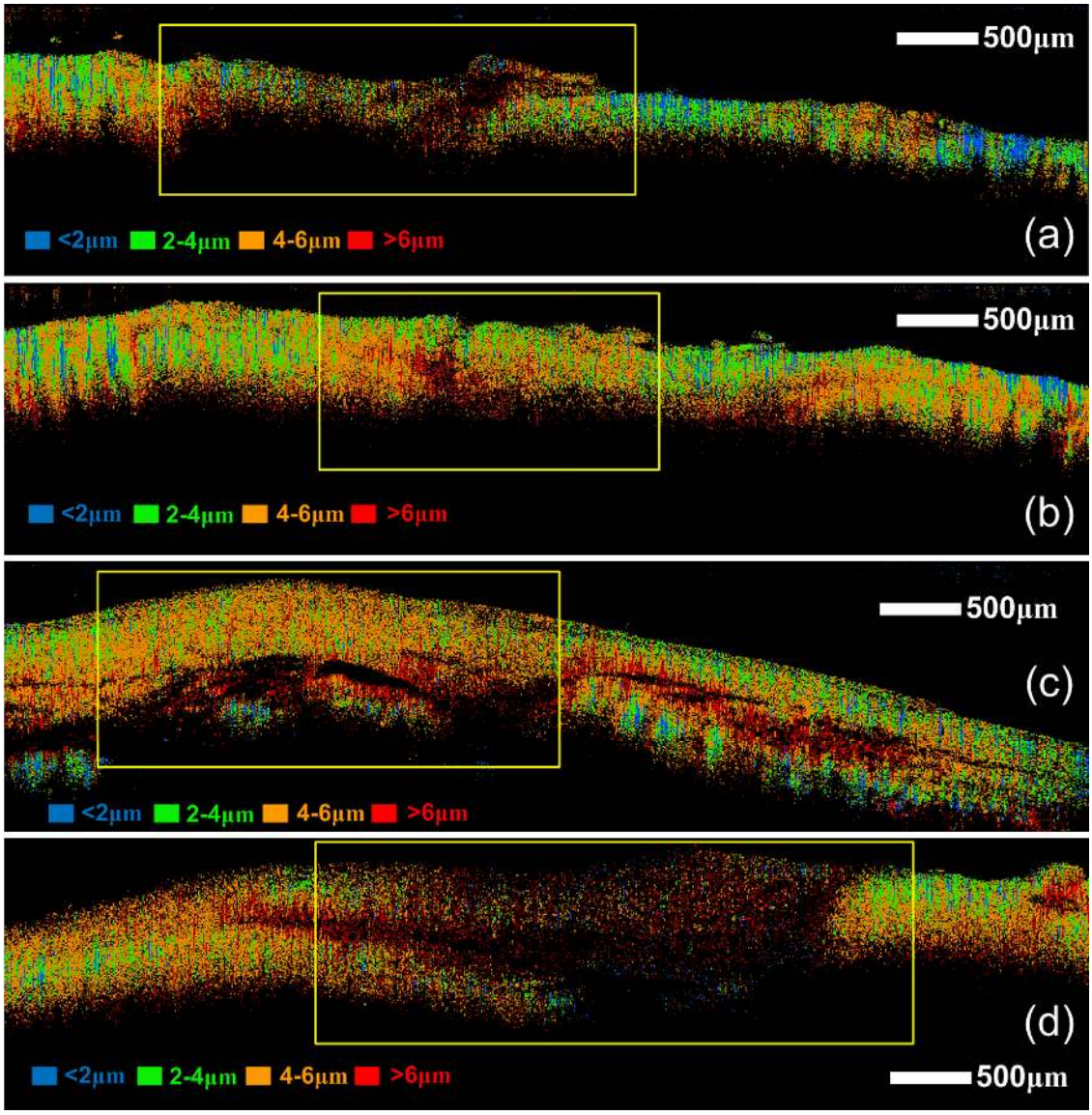

Figure 6-15: DWDB-SOCT images of (a) fibrin glue control, (b) 1M autologous BMSC seeded, (c) 1M allogeneic BMSC seeded and (d) 4M allogeneic BMSC seeded flexor tendons at the 8 weeks time point. Yellow boxes indicate tendon healing region.

The different spectroscopic images of the tendon groups resulted from the unique healing conditions within each rabbit. To quantify the healing rate in each study group, the fraction of large scatterers, r_{ls}, within a region-of-interest (ROI) in the spectroscopic image is used:

$$r_{ls} = \frac{n_r + n_o}{n_r + n_o + n_g + n_b} \quad \textbf{(6.1)}$$

where n_r and n_o are the number of red and orange pixels representing large scatterers, and n_g and n_b are the number of green and blue pixels representing small scatterers in the selected region. The fraction of small scatterers, r_{ss}, within the same ROI in the SOCT image is given by:

$$r_{ss} = 1 - r_{ls} \quad \textbf{(6.2)}$$

Equation 6.2 is used to quantify the formation of new collagen (blue and green pixels) with respect to the total number of scatterers within the healing region.

A large variability in the analysis of the scatterers in the tendon healing region is expected due to the biological variation in the healing process. Thus to obtain an accurate picture of the healing condition of an injured tendon, a total of 41 tendons are used for this study. The result of the analysis based on the healing regions in the DWDB-SOCT images is tabulated in Table 6-1. The fraction of small scatterers in the healing region of each tendon seeding group is also plotted in Figure 6-16 for comparison. At the 3 weeks time point, all the BMSC-seeded tendons show a larger concentration of small scatterers compared to the fibrin glue control. This signifies the formation of organized collagen fibrils in the BMSC-seeded tendons. In particular, the 1M allogeneic BMSC seeded tendon group shows the largest concentration of small scatterers, surpassing even the 4M allogeneic MSC seeded tendon group. This suggests that a higher concentration of BMSCs introduced to the tendon injury site does not translate to a greater rate of collagen formation. At the 8 weeks time point, the small scatterer concentration for the fibrin glue

control is similar to those of BMSC seeded tendon groups. The results indicate that BMSC seeding is effective in the early stages of tendon healing following suture repair. After the 8 week time point, all tendon groups exhibit similar levels of collagen concentration. The results are supported by the statistical analysis of small scatterer percentage across all cell seeding groups for the 3 and 8 weeks time points shown in Table 6-2. There is statistically significant difference ($p<0.05$) between the 1M allogeneic BMSC cell seeding group and the Tisseel fibrin glue control group at the 3 weeks time point. At the 8 weeks time point, however, there is no statistical difference between the cell seeding groups.

Table 6-1: Fraction of large and small scatterers in the healing region of BMSC seeded flexor tendons at different time points.

	Time Points									
	3 weeks					8 weeks				
Type of seeding at repair site	**n**	**Large Scatterers (%)**	**Large Scatterers SD (%)**	**Small Scatterers (%)**	**Small Scatterers SD (%)**	**n**	**Large Scatterers (%)**	**Large Scatterers SD (%)**	**Small Scatterers (%)**	**Small Scatterers SD (%)**
Tisseel Fibrin Glue	4	78	4.1	22	4.1	5	67	15.5	33	15.5
1M Autologous BMSC	6	75	6.6	25	6.6	8	71	14.4	29	14.4
1M Allogeneic BMSC	5	66	16.9	34	16.9	5	68	15.4	32	15.4
4M Allogeneic BMSC	5	72	14	28	14	3	69	14.6	31	14.6

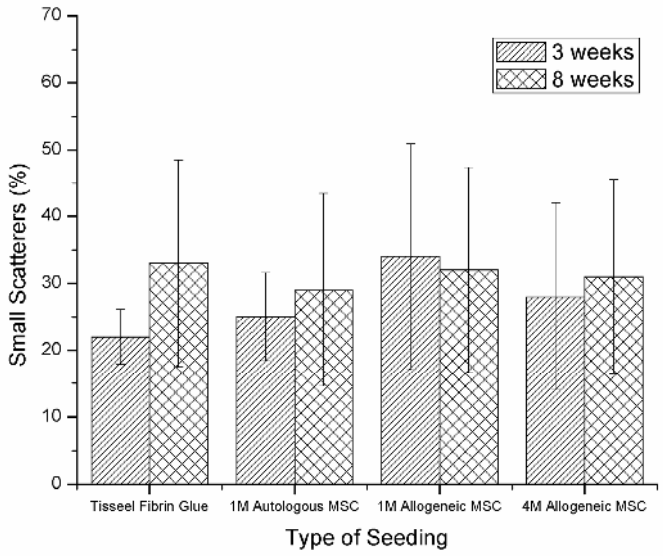

Figure 6-16: Fraction of small scatterers in the healing region of each tendon seeding group. Error bars represent ±1σ.

Table 6-2: Statistical analysis of the small scatterer percentage across all cell seeding groups for 3 and 8 week time points. P-values of less than 0.05 are in bold.

	3 weeks				***8 weeks***			
Type of cell seeding	Tisseel Fibrin Glue	1M Autologous BMSC	1M Allogeneic BMSC	4M Allogeneic BMSC	Tisseel Fibrin Glue	1M Autologous BMSC	1M Allogeneic BMSC	4M Allogeneic BMSC
Tisseel Fibrin Glue		0.259	**0.0305**	0.12		0.404	0.476	0.452
1M Autologous BMSC			0.115	0.334			0.42	0.447
1M Allogeneic BMSC				0.37				0.476

6.4 Discussion

Conventional intensity-based OCT images do not show significant difference between the tendon samples. The spectroscopic images, on the other hand, showed good contrast

between scatterers of size greater and less than 4 μm. However, the effects of multiple scattering in normal tendon sections exclude spectroscopic analysis in this regions and limit the analysis to the healing sections. The results showed that BMSC seeded tendons achieved a greater degree of healing at the 3 weeks time point compared to fibrin glue control tendon. At the 8 week time point, however, all BMSC seeded tendons were observed to given similar healing effects as the fibrin glue control. The findings are in good agreement with the study of Chong *et al.* [22], where intratendinous cell therapy with allogeneic BMSCs following primary tendon repair was found to improve histological and biomechanical parameters in the early stages of healing (<3 weeks) but not at subsequent periods.

The use of allogeneic BMSCs solves the problem of cell supply for implantation and they perform similarly to autologous cells without the side effects of host immune response. No immune response in histology was observed in this study, and there is much evidence to show that allogeneic BMSCs can moderate host immune behaviour [189-190]. Studies have also shown that the improvement in tendon properties at three weeks is due to accelerated healing [22] rather than inflammation or scar formation. The results in this work show that allogeneic BMSCs perform better than autologous BMSCs at three weeks in terms of collagen synthesized at the repair site. The concentration of the cells used, on the other hand, does not follow a linear relationship with rate of healing. The reason for this could lie in the exact role that implanted BMSCs plays in tendon healing, but this still remains uncertain [22]. It is postulated that the implanted BMSCs differentiate into fibroblasts which participate in collagen production and remodeling. Alternatively they may contribute

to healing by producing growth factors to encourage cell growth by the body, instead of participating in direct cell differentiation.

As healing tendons can have highly varied morphology at the healing site, the SOCT imaging of the healing region in injured tendons and the subsequent quantitative analysis can be made more accurate by increasing the sections analyzed for every tendon. A volumetric analysis of each tendon would present quantitative results of higher statistical accuracy for comparison between healing tendons.

6.5 Summary

DWDB-SOCT is used to study the effect of BMSCs on flexor tendon healing in a rabbit model. Four different tendon seeding groups were established for comparison, based on the types of stem cells introduced to the injury site, namely tisseel control (fibrin glue), 1M autologous BMSCs, 1M allogeneic BMSCs and 4M allogeneic BMSCs. The rabbit flexor tendons were harvested at two time points, 3 weeks and 8 weeks, for *ex vivo* imaging. It was found that the organized collagen sections of normal tendon exhibit large scatterer characteristics in spectroscopic analysis, probably due to the dense packing of collagen fibrils.

Although conventional intensity-based OCT images showed significant structural differences between organized collagen and the healing site, differences between the tendon seeding groups cannot be discerned. By contrast the spectroscopic images were able to differentiate fibroblasts/stem cells and collagen by scatterer size using a threshold size of 4

μm. A scatterer size quantification method was used to compare the fraction of large and small scatterers in the healing regions of the spectroscopic images. The small scatterers are of interest as they represent newly synthesized collagen in the healing sections of injured tendons. The results showed that BMSC seeded tendons achieved a greater degree of healing at the 3 weeks time point compared to fibrin glue control tendon. At the 8 weeks time point, however, all BMSC seeded tendons showed identical healing effects as the fibrin glue control. Allogeneic BMSCs were found to perform better than autologous BMSCs in terms of collagen synthesized at the repair site.

Chapter 7 Monitoring Cell Proliferation in Silk Fibroin Scaffolds using DWDB-SOCT

7.1 Introduction

7.1.1 Background

The replacement of failed organs or damaged tissue in the human body involves organ transplants or tissue grafting, and these methods have greatly improved the quality of life post-treatment. The availability of suitable organs or tissues that are biocompatible with the recipient, however, can be severely limited and there is always the risk of organ/tissue rejection and a need for lifelong immunosuppressive therapy [118]. Tissue engineering is an established field whose purpose is the repair, replacement or regeneration of tissues and organs using living cells and biomaterials [191-192]. Tissue scaffolds are essentially used to house growing cells. The tissue scaffolds also support, reinforce and in some cases organize the regenerating tissue [25]. Such requirements call for a porous scaffold microstructure, with pore size and porosity characteristics being application-specific [24-25]. An ideal scaffold should have several characteristics [23, 193]: (i) A 3D and highly porous with an interconnected pore network for cell growth and flow transport of nutrients and metabolic waste; (ii) biocompatible and bioresorbable with a controllable degradation and resorption rate to match cell/tissue growth *in vitro* and/or *in vivo*; (iii) suitable surface chemistry for cell attachment, proliferation, and differentiation and (iv) mechanical properties to match those of the tissues at the site of implantation.

Synthetic polymers have been explored as biomaterials for tissue scaffolds as they are able to withstand harsh processing conditions and do not degrade or decompose easily when

exposed to chemical solvents or high processing temperatures. Naturally derived biomaterials, like silk, are rarely used in advanced tissue engineering methods despite their superior biocompatibility compared to synthetic polymers. Silk is a fibrous protein that is spun into fibers by silkworms and spiders [194-195]. Silk is characterized by a highly repetitive primary sequence that leads to significant homogeneity in secondary structure (β-sheets). The relative environmental stability, excellent biocompatibility, unique mechanical properties of silk (resistance to tension and compression) and ease of growing/harvesting raw material provide an excellent basis for use in tissue scaffolds over other natural polymers [194].

Silk fibroin (SF), a protein-based material derived from the cocoons of *Bombyx mori* silkworms, has been used extensively for biomedical applications owing to its biocompatibility and high mechanical strength [194]. An example of the structure of a silk fibroin (SF) scaffold is shown in Figure 7-1. The scanning electron microscopy (SEM) image of the internal morphology shows leaf-like structures corresponding to the β-sheet structure of SF [196]. SF scaffolds have been used in tissue engineering applications like skeletal tissue engineering of articular cartilage, bone, ligaments/tendon, as well as connective tissue like skin [197-199]. The SF tissue scaffolds are often processed under mild conditions and yielded in the form of sponges or meshes to mimic the tissue extracellular matrix (ECM). However, these conventional fabrication methods only allow limited user-defined control over the internal architecture of the SF scaffolds [200]. As a result, this drawback may lead to cell attachment and growth only at the periphery of the tissue scaffolds due to the lack of mass transfer of nutrients within the constructs.

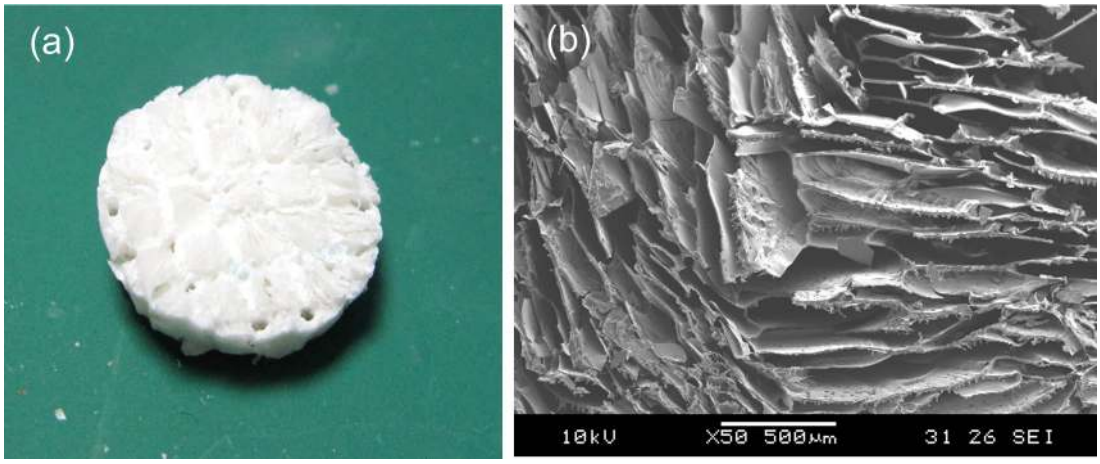

Figure 7-1: (a) 10% (wt/wt) SF scaffold and its (b) SEM image, showing the β-sheet of SF [200].

To overcome the limitations and difficulties experienced with conventional fabrication methods, the application of Rapid Prototyping (RP) or Additive Manufacturing (AM) techniques such as selective laser sintering (SLS), fused deposition modelling (FDM) and 3D printing have been explored [201-209]. These RP processes are commonly combined with computer aided designs (CAD) to manufacture patient-specific tissue scaffolds. Furthermore, with complete user control over the structural features of the scaffold models, customized environments can be established for cell anchorage, proliferation and secretion of tissue-specific components within the constructs [210-213].

When a tissue scaffold is fabricated, several parameters need to be characterized to verify that the fabrication process has resulted in the desired scaffold architecture (pore size, porosity, strut size) [23-25]. Newly designed and fabricated scaffolds are evaluated for cell growth by seeding cells onto them. Parameters of interest includes monitoring a tissue scaffold include cell proliferation rate [214], cell-scaffold interaction [23] and tissue culture

conditions. In addition, the assessment of cell-scaffold interaction during late stages, where the scaffold starts to degrade and the tissue start to form with blood vessels, presents another picture of nutrient transport mechanisms [23].

7.1.2 Motivation

SEM [24-25, 214-215] is primarily used for the visualization and analysis of tissue scaffold structure, and the technique offers the highest resolution images (~3 nm) [216]. This enables fine scaffold features such as pore size and porosity, and even cells attached to the scaffold to be observed with good resolution [200] but it is limited to imaging the surface features of a sample. Furthermore SEM imaging, which requires sample sectioning and preparation, is time-consuming and tedious, and above all, destructive. Cell concentration/proliferation can be measured using DNA fluorescence assays [217] or MTT colorimetric assays [214], which are also destructive methods. The advantage of using biological assays is that the viability of the cells in the scaffold can be measured as only live cells will be counted. Confocal fluorescence microscopy [214] has been used for imaging fibroblast cell proliferation in seeded scaffolds; the advantages include the non-invasive imaging of cells with good contrast and resolution (~1 μm) [214]. The drawbacks are the low penetration depth and toxic reagent staining. Such analyses therefore only provide end-point observations and results. This poses a severe limitation in monitoring the health of seeded tissue scaffolds throughout the culture period [148].

μCT been used in bone tissue engineering to analyze scaffolds, focusing on imaging and quantification of scaffold characteristics like pore sizes, porosity and strut thickness [23,

218]. It can also achieve precise measurements of bone growth into the scaffold and onto its surface. The advantages of the technique include high resolution (5–100 μm) and 3D imaging of tissue scaffold structure [23]. The drawbacks of the technique are the use of harmful radiation, toxic contrast agents and the limitation of tissue imaging mainly to bone tissue. MRI has also been used to image tissue growth in scaffolds, and can achieve relatively high resolution (~100 μm) using high field systems [26-27, 219]. Tissue implantation after the scaffold tissue is ready can also be imaged *in vivo* with MRI. The drawbacks of the technique are the poor resolution, and the ability to image only soft tissues with high water content, e.g. adipose tissue. Bone does not show up with good contrast in MRI images due to low concentration of hydrogen atoms in bones [27].

OCT has been used to study engineered tissue in tissue scaffolds [80, 110, 118, 146-148, 220-230]. Initial studies have shown that conventional OCT images of seeded tissue scaffold offered little contrast between the scaffold and the seeded cells [148]. It was found that conventional OCT is capable of characterizing scaffold architecture and the pore size, porosity or micro-channel dimension can be determined both quantitatively and qualitatively [110, 147-148]. In other words, characteristics of blank tissue scaffolds can be determined with conventional OCT imaging, but there are limitations in the monitoring of cell seeded tissue scaffolds as there is little to no differentiation between cells and the scaffold material in intensity-based OCT images.

SOCT [118] can give functional information about engineered tissues growing within scaffolds or as an inference to scaffold architecture and design. Engineered tissues with

fibroblasts and macrophage cells were cultured in porous chitosan scaffolds and imaged using SOCT [38, 118]. Color codes of the cells in the image were based on spectral modulation, characterized with autocorrelation bandwidth, to give information of relative cellular size. It was found that fibroblast cells exhibited a wider profile compared to the macrophage cells. Due to the use of STFT and 80% autocorrelation bandwidth as the spectroscopic metric, a more accurate particle sizing is not achieved and only relative comparisons between the cells were made. Nevertheless, SOCT is a potentially powerful tool for observing cell distribution over time in a scaffold, tracking cell growth as well as the efficacy of scaffold structure as a cell incubator.

In this chapter, the use of DWDB-SOCT for monitoring SF scaffolds cell proliferation *in vivo* over various time-points is presented. Mouse embryo fibroblast (MEF) cells are seeded into the SF scaffolds and the scaffolds are monitored by SOCT after one, three and five weeks. These time points are chosen to give sufficient time for the fibroblasts to proliferate and the imaging results are analyzed to determine the cell proliferation rate. Cell proliferation is measured by quantifying the large scatterers with respect to the total number of scatterers in the spectroscopic image as a function of time.

7.2 Materials and Methods

7.2.1 Silk Fibroin Tissue Scaffold Fabrication and Cell Seeding

Aqueous SF solution was obtained from degummed cocoons of the *Bombyx Mori* silkworm [200]. To fabricate the protein-based 3D tissue scaffold with internal channels, aqueous SF with concentration of 10% (wt/wt) was cast into the sacrificial thermoplastic moulds. The

negative sacrificial moulds were designed using a commercial CAD software and manufactured using a 3D inkjet printer where rapid prototyping technology was applied. The cast moulds were allowed to stand for 15 minutes under room temperature to ensure full penetration of the aqueous SF within the scaffold's negative template. Subsequently, the moulds containing the SF solution were frozen and freeze dried to obtain the SF tissue constructs. After the freeze drying process, the specimens were immersed in ethanol to induce β-sheet structure of silk. Subsequently, the scaffolds were immersed into ethanol to remove the thermoplastic moulds, and then rinsed with de-ionized water and freeze dried. A thermoplastic negative mould and a blank 10% (wt/wt) SF tissue scaffold within internal channels are shown in Figure 7-2a and Figure 7-2b, respectively. The width of each printed strut of the mould was approximately 700 μm and the strut was clearly replicated onto the SF construct.

The scaffolds were conditioned with cultured medium (DMEM supplemented by 10% (v/v) fetal bovine serum and 1% (v/v) penicillin/streptomycin mixture, Invitrogen) using a 24-well culture plate and incubated for 24 hours (Figure 7-2c). On the day of cell seeding, the culture medium in the culture plate was discarded and each sample was seeded with 1.5×10^6 cells (3T3, MEFs) in 200 μL of culture medium. The medium was changed every two days until harvest at one, three and five week time points. The respective seeded SF scaffolds are imaged using SOCT and subsequently sent for histological processing.

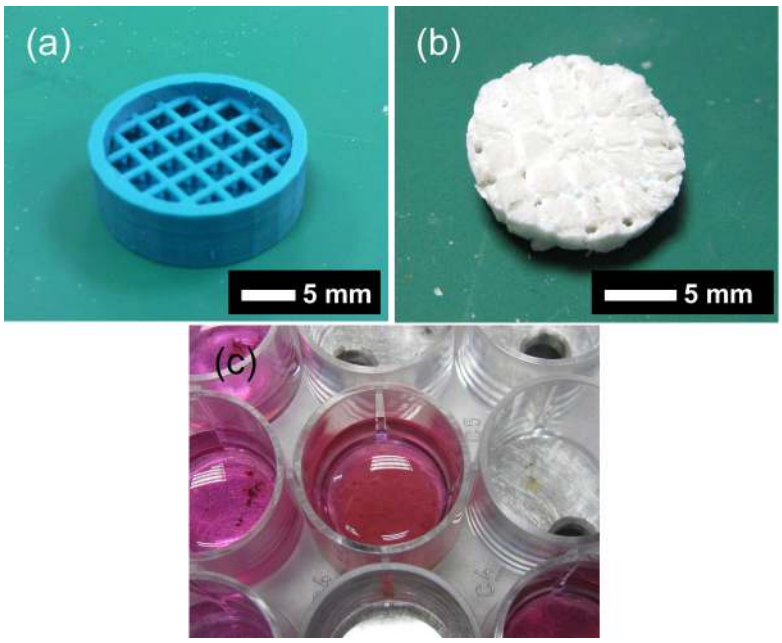

Figure 7-2: (a) Printed thermoplastic mould and the (b) SF scaffold obtained from the RP-fabricated mould [200]. (c) The cell seeded SF scaffolds are incubated in culture medium.

7.2.2 MEF Seeded Silk Fibroin Scaffold Imaging

The seeded scaffolds are imaged *in vivo* through culture medium in the culture plate. A $6.5\times1\times2$ mm^3 imaging volume was taken. The measurement data is recorded as raw B-scan spectral information and is processed using custom Matlab programs to obtain the OCT and spectroscopic images. After imaging, the OCT line scan region on the SF scaffold is marked with two microinjections of ink before sending for routine histological processing. Multiple 5 μm thick sections are obtained from the marked region and stained with H&E. Bright field images of the scaffold sections are taken digitally using a standard microscope.

7.3 Results

7.3.1 SF Scaffold Histology

The histological section of a blank SF scaffold is shown in Figure 7-3a. The section shows surface macro-channels (indicated by black arrows) with widths ranging from 600–700 μm. Internal macro-channels for nutrient and waste transport can be observed in the image within the yellow box and they have the same dimensions as the surface macro-channels. The sheet structure of the SF can also be observed and the spacing between sheets is measured to be <100 μm. Due to the histological processing conditions, the scaffold section may undergo some deformation and the sheet spacing may be increased from the actual dimensions. Figure 7-3b shows the bright-field image of a MEF seeded SF scaffold section at the 5 weeks time point. Seeded SF scaffold sections of 1 and 3 weeks time points did not survive the histological processing. The fibroblast cells did not attached properly to the scaffolds and were washed away during processing. By contrast, cell masses in 5 weeks seeded SF scaffold sections had grown to an extent significant enough to anchor securely onto the scaffolds and thus survive the histological processing.

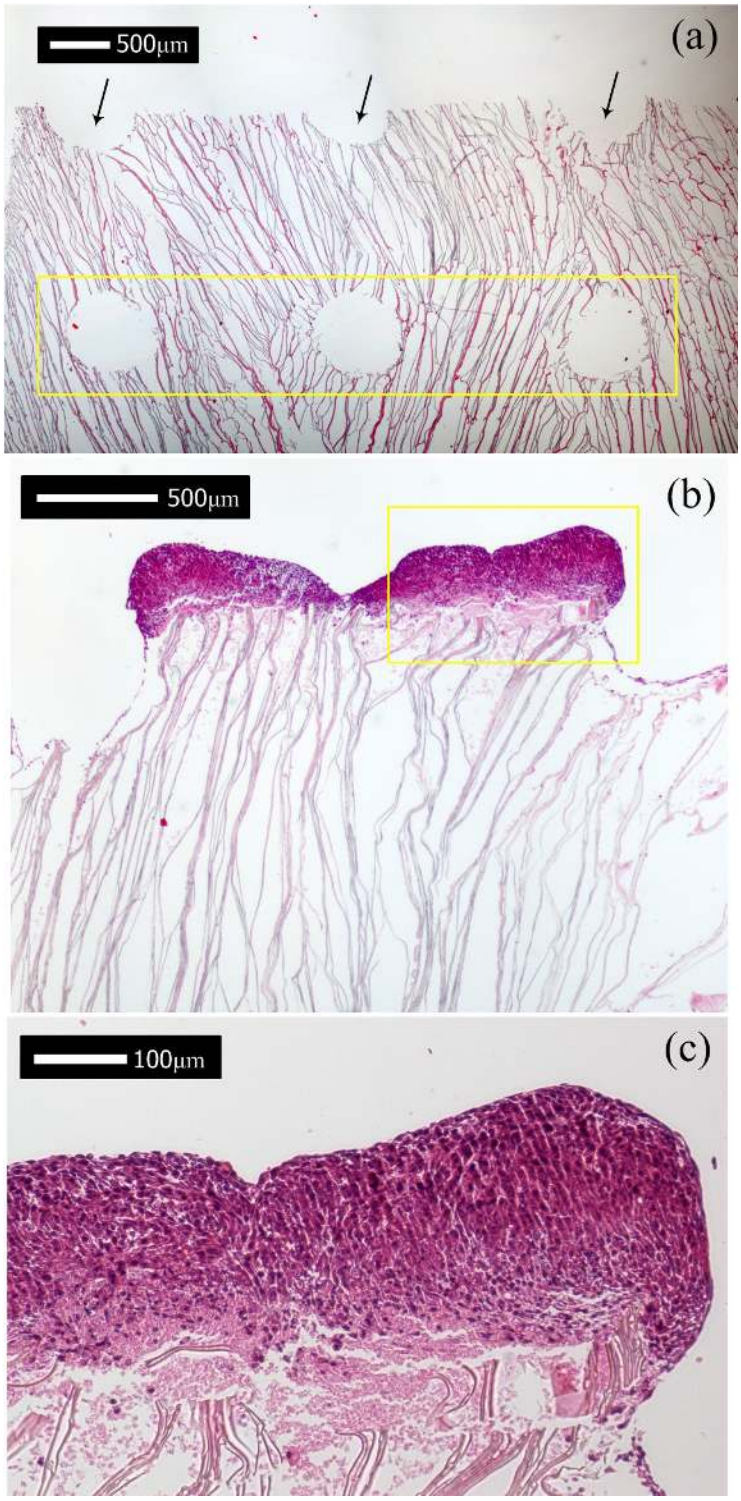

Figure 7-3: H&E stained bright-field images of (a) blank SF scaffold section (black arrows indicate the surface macro-channels) and (b) MEF seeded SF scaffold after 5 weeks. Yellow boxes highlight the internal macro-channels. (c) Expanded view of yellow box in (b).

MEF cells were reported to have a nuclei diameter of about 10 μm when not attached to any surface [231]. However the MEF cell cytoplasm elongate and branches out with the cell nuclei compressed to an elliptical shape ranging from 4–7 μm when attached to a surface. It is observed that the fibroblast cells tend to grow on the surface of the SF scaffolds without penetrating inward. The seeded SF scaffolds are incubated in well plates without flow circulation. Hence even with macro-channels leading to the scaffold interior, the fibroblast cells only anchor onto the scaffold surface due to the stagnant flow condition of the medium. The cell mass was observed to protrude out from the scaffold sections in between the surface macro-channels, as shown in Figure 7-3c.

7.3.2 Spectroscopic Imaging of Blank SF Scaffold

The scaffold is first imaged to quantify its spectroscopic characteristics. The scaffold can be observed in the conventional intensity-based OCT image of Figure 7-4a as diffused, leaf-like structures due to the high porosity, low density morphology of SF. The surface macro-channels can be clearly observed with a width of about 720 μm and a depth of 860 μm. The strut width matches closely the mould designed strut width of 700 μm. The pore sizes between the SF β-sheets ranges from 50 to 170 μm and corroborates the SEM images of the SF scaffold sections [200]. A higher contrast was observed on the channel walls compared to the scaffold surface due to compaction of SF during the fabrication process. The SF sheets, on the other hand, gave a poor contrast due to a limited backscattering of light.

The DWDB-SOCT image shown in Figure 7-4b is obtained by setting the hue of scatterer size of <2 μm, 2–4 μm, 4–6 μm and >6 μm to blue, green, orange and red, respectively.

Scatterers with size of >4 μm (orange and red) are considered large scatterers while small scatterers have size <4 μm (blue and green). The size of MEF nuclei measured from histology ranges from 4–7 μm in thickness. Since the cells are imaged axially, the thickness of the fibroblast nuclei will determine its scatterer sizing and are considered large scatterers. SF is made up of small molecules that are processed to form diffuse scaffold structures and the spectroscopic signal from the scaffold is expected to show up as mainly small scatterers size of <2 μm. This is indeed observed in the DWDB-SOCT image of Figure 7-4b, where largely small scatterers (blue) are measured. The small quantity of larger scatterers measured in the image is attributed to SF compaction.

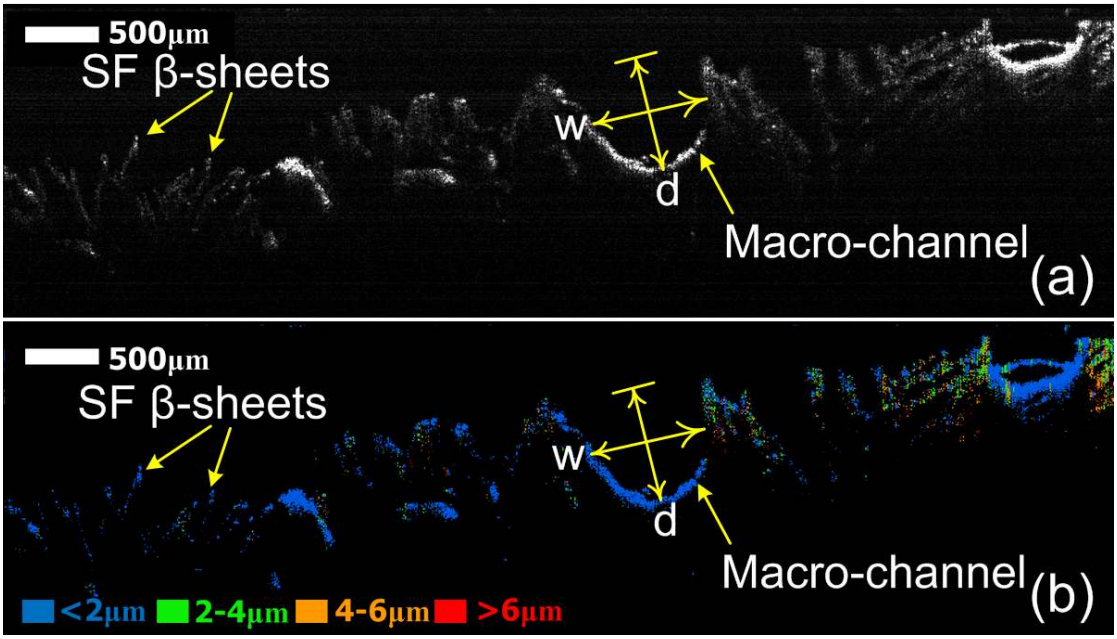

Figure 7-4: (a) Conventional intensity-based OCT and (b) DWDB-OCT images of a blank SF scaffold. *w* – width. *d* – depth of macro-channel.

7.3.3 Spectroscopic Imaging of Mouse Embryo Fibroblasts (MEF)

A concentrated sample solution of pure MEFs is cultured and extracted for OCT imaging. This serves as a control sample to determine its spectroscopic characteristics. The resulting intensity-based OCT image (Figure 7-5a) shows a uniformly scattering MEF sample. The DWDB-SOCT image in Figure 7-5b reveals a majority of large scatterers (orange and red) of size >4 μm. This is in good agreement with histological observations. Fibroblast cells have a branched cytoplasm surrounding an elliptical nucleus and when the cells are adhered to a surface the thickness of the nucleus can be reduced. The green vertical stripes observed in Figure 7-5b could be due to the presence of elongated cell nuclei in these regions which present a reduced axial size leading to a green hue.

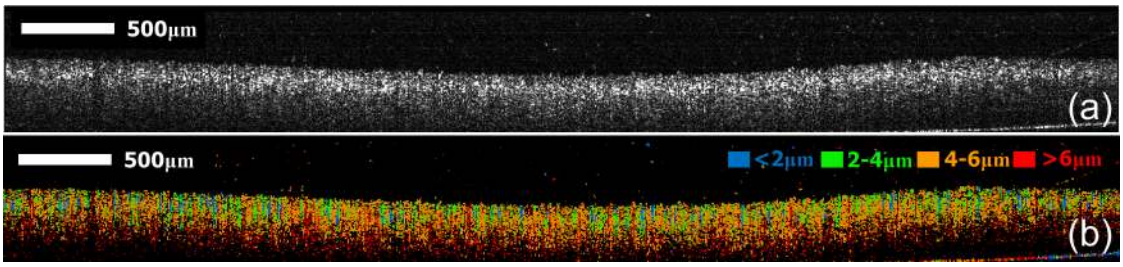

Figure 7-5: (a) Conventional intensity-based OCT and (b) DWDB-SOCT images of concentrated MEF sample.

7.3.4 Spectroscopic Imaging of MEF Seeded SF Tissue Scaffolds

Cell proliferation in MEF seeded SF scaffolds grown till 1 week, 3 weeks and 5 weeks time points were monitored *in vivo* using DWDB-SOCT imaging. The intensity-based OCT and DWDB-SOCT images of the resulting MEF seeded scaffolds are shown in Figure 7-6 and Figure 7-7, respectively. The macro-channels that are created in the SF scaffold by the thermoplastic moulds for nutrient and cellular transport are clearly observed in the

intensity-based OCT image, and the measured depth and width are 700–850 μm and 570 μm, respectively.

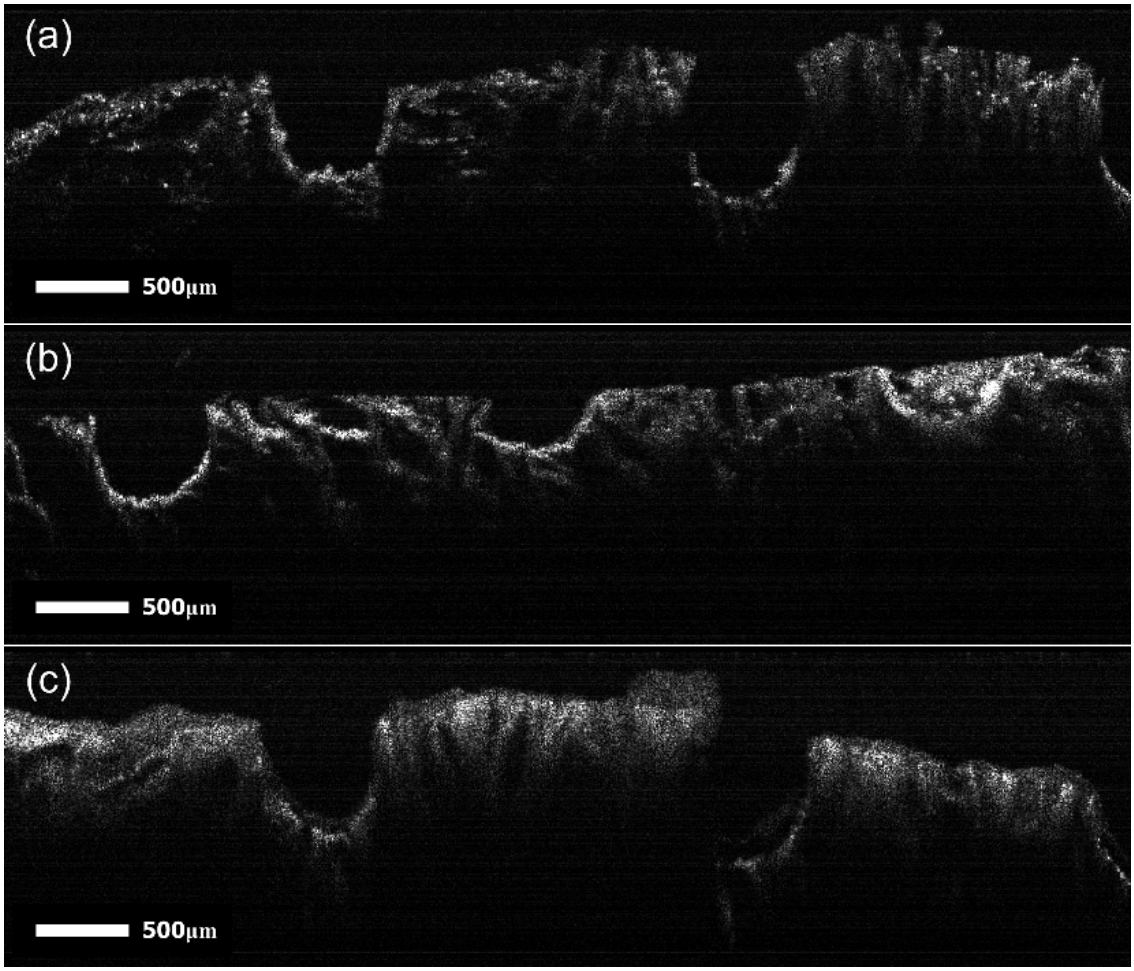

Figure 7-6: Conventional intensity-based OCT images of fibroblast seeded SF scaffolds at (a) 1 week, (b) 3 weeks, and (c) 5 weeks time points.

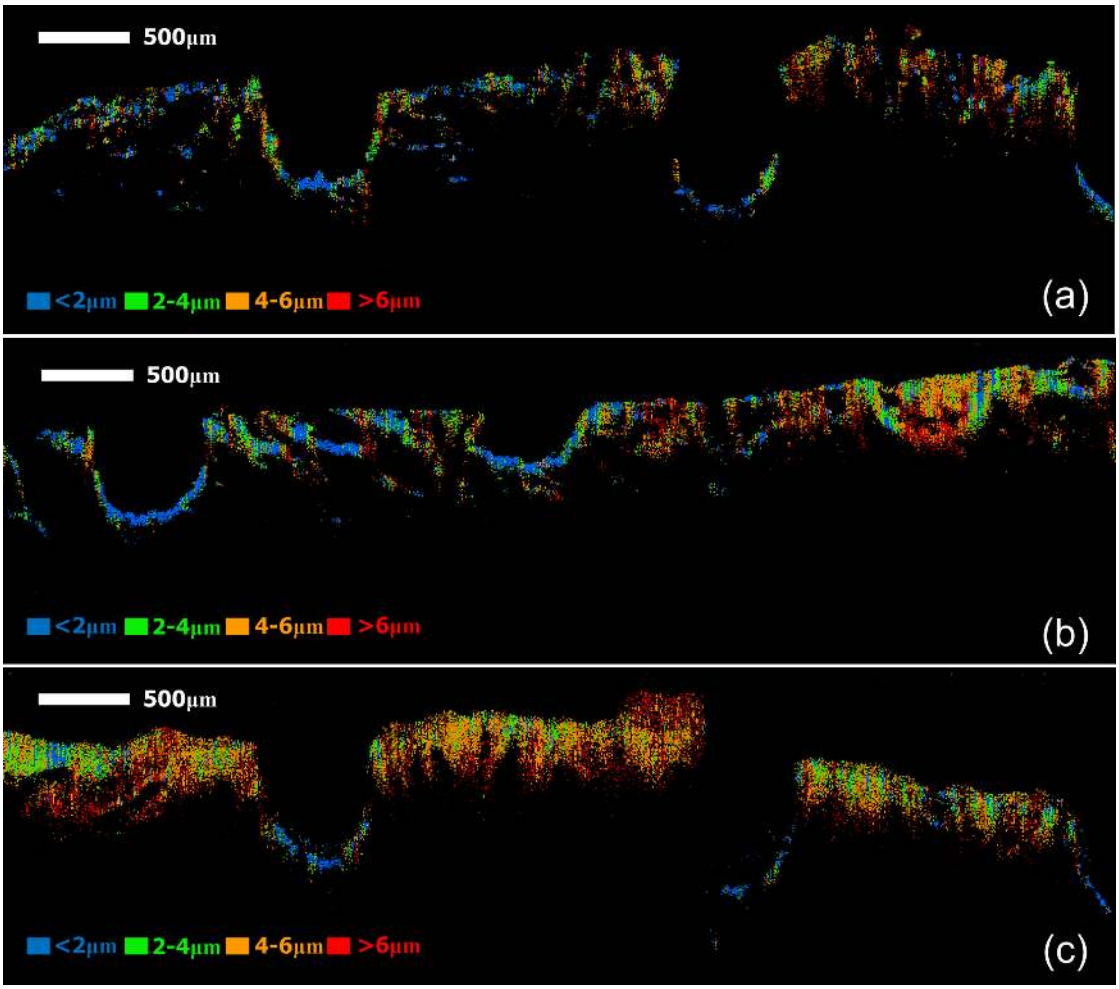

Figure 7-7: DWDB-SOCT images of fibroblast seeded SF scaffolds at (a) 1 week, (b) 3 weeks, and (c) 5 weeks time points.

In the intensity-based OCT images (Figure 7-6), the pores of the SF sheets were observed to become more scattering with time due to the proliferation of cells. However, it is difficult to differentiate between cells and the scaffold material due to low contrast in the image. The intensity-based OCT image of the MEF seeded scaffold at 1 week (Figure 7-6a) revealed the leaf-like β-sheet structure of silk in between the surface macro-channels. The structural features of the SF scaffold are still clear at this early stage and the presence of MEF cells is not obvious. At 3 weeks (Figure 7-6b), a section with higher scattering

contrast in the rightmost macro-channel was detected. Some growths, presumably fibroblast cell masses, were found to fill the gaps of the scaffold and extend out of the scaffold at 5 weeks (Figure 7-6c). An accurate determination of cell distribution on the scaffold from the intensity-based OCT image is hindered by the low contrast between the scaffold and the cell aggregates.

By contrast, the DWDB-SOCT images in Figure 7-7 clearly differentiate the fibroblast cell aggregates and the SF scaffold. At the 1 week time point (Figure 7-7a), the presence of the MEFs is revealed by large scatterers (orange and red) growing on the surface of the SF scaffolds. The pores are observed to be sparsely populated and cells (orange and red) are seen to penetrate to a depth of up to 450 μm below the surface. Figure 7-7b shows that MEFs inhabit the rightmost macro-channel as well as the surface of the SF scaffolds after 3 weeks. The MEFs are found to penetrate to a depth of up to 450 μm below the surface, similar to the seeded SF scaffold after 1 week.

It is observed in Figure 7-7c that the micro-pores in the SF scaffold are fully filled with cell aggregates (orange and red) and a cell mass even grows outside the scaffold at the 5 weeks time point. The large scatterers with size >4 μm shown in the DWDB-SOCT images are consistent with MEFs identified in histological images. The macro-channels do not have any cell growth, possibly due to the compacted nature of the SF material compared to the SF β-sheets which forms micro-pores aiding cell attachment and proliferation. The DWDB-SOCT images provide a significantly improved contrast than the intensity-based OCT images due to the ability to differentiate tissue scatterers.

The locations of MEF cells within the SF scaffolds can be determined even at the early stages of cell seeding using the DWDB-SOCT method. The cell proliferation within the SF scaffold over time is of interest, and this can be quantified by analyzing the spectroscopic images at various time points for large scatterers with size >4 μm. The fraction of large scatterers within the scaffold is computed using Equation 6.1 to quantify the relative MEF cells population at each time point.

Table 7-1 shows the scatterer distribution in each sample at different time points. The presence of small scatterers in a purely large scatterer sample like fibroblast cell culture and the presence of large scatterers in a purely small scatterer sample like a blank SF scaffold can be attributed to background noise, and a larger sample size will help to reduce these variations. The rate of fibroblast cell (large scatterers) proliferation in the SF scaffold is plotted in Figure 7-8. The fibroblast cells are observed to increases monotonically with culture time.

Table 7-1: Fraction of large and small scatterers in MEF culture, blank SF scaffold and MEF seeded SF scaffolds at different time points.

Sample	Large Scatterers (%)	Small Scatterers (%)
Fibroblast Cell Culture	82	18
Blank SF Scaffold	30	70
MEF seeded SF Scaffold at 1 week	45	55
MEF seeded SF Scaffold at 3 weeks	47	53
MEF seeded SF Scaffold at 5 weeks	71	29

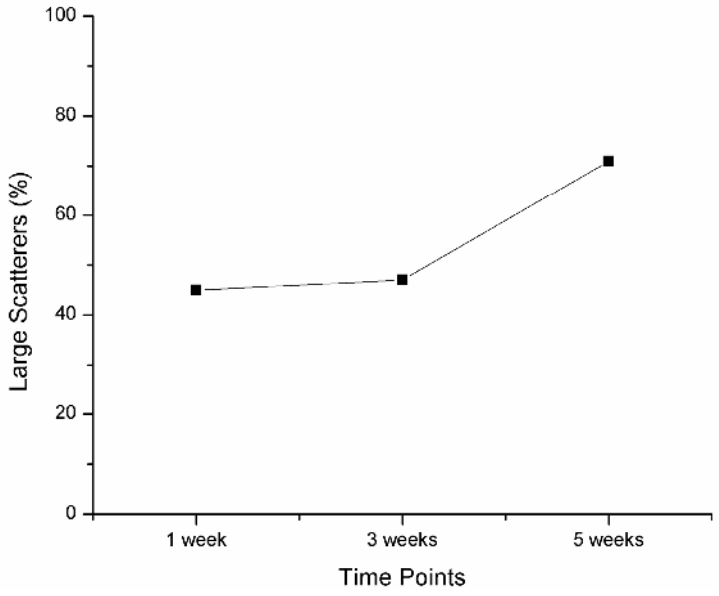

Figure 7-8: Plot of large scatterer percentage in SF scaffolds over time.

7.4 Discussion

Due to the unique β-sheet structure of SF, the conventional intensity-based OCT images (Figure 7-4a) reveal leaf-like morphologies which are consistent with the results reported by Kaplan *et al.* [232]. The pore walls, or wall of the "leaves", in the SF scaffold are made of homogenous SF and the intensity-based OCT images showed uniform scattering within the "leaves". The density of the SF material is found to be low except for certain locations in the scaffold, such as the macro-channels, where the SF is compacted. The intensity-based OCT is therefore suitable for imaging the structural features of tissue scaffolds.

For cell culture in the scaffold of up 1 week, the cell concentration is still sparse and the scaffold contrast does not increase due to the low density of the SF material. This limits the backscatter intensity of incident light. The contrast of intensity-based OCT images

increases for 3 weeks and beyond. The slightly clearer images provided sufficient details to show that the fibroblasts were able to migrate within the pores of SF, proliferate and fill the voids. The cells acted as contrast enhancement agents for the scaffold, due to the higher light scattering from cell boundaries and the surrounding medium. These observations match previously reported investigations which incorporated cell growth, particles and beads of known reflective indexes to enhance the image contrast of scaffolds [148, 233].

Intensity-based OCT image comparisons of blank and five weeks fibroblast seeded SF scaffold showed the filling of interstitial spaces in the scaffold by the fibroblasts. These results were consistent with those of Ying [148] who used PLLA scaffolds seeded with bone cells and presented images of blank and seeded scaffolds at five weeks time point, showing the filling of pore spaces in the scaffold. However, the cells cannot be distinguished from the scaffold in the conventional intensity-based OCT images. Fibroblast cells grown in chitosan scaffolds have been imaged using SOCT [38, 118], although cellular sizes were not determined. Even though the MEF cell nuclear size is smaller than human fibroblast cells with cell nuclear size ranging from 40 to 50 μm [178], they are very different in size from the surrounding tissue scaffold. Consequently SOCT can be used for tissue scatterer differentiation in seeded tissue scaffolds. The MEF cells can easily be monitored within the SF scaffold by DWDB spectroscopic analysis (Figure 7-7). This allows several parameters of interest to be found non-invasively, including cell proliferation based on the fraction of large scatterers within a ROI, cell-scaffold interaction based on the distribution of large scatterers, and tissue culture conditions based on the quantity of large scatterers at the surface compared to those within the scaffold.

The rate of cell proliferation through the scaffold with time was monitored by quantifying the fraction of large scatterers in a scaffold ROI, as illustrated in Figure 7-8. The result indicates that the cell mass slowly increases in the first 3 weeks and almost doubled after 5 weeks of culture in the scaffold. Cell-scaffold interaction was also evident in the DWDB-SOCT images where fibroblast cells (large scatterers) were found to avoid the macro-channels in the scaffold (Figure 7-7c). This is attributed to the compact nature of the SF in the region which does not provide good anchorage for cells. Instead the DWDB-SOCT images revealed that the cells occupy the SF sections in between the macro-channels, which have pores for housing the cells.

The effect of tissue culture conditions such as nutrient delivery and waste removal on the cell distribution in the scaffold was also determined. As the seeded SF scaffolds are housed in a well plate with no circulation of the culture medium, fibroblast cells were found to reside on the scaffold surface instead of migrating to the interior of the scaffold. Therefore nutrients have to be circulated and waste materials removed dynamically, so that cells can penetrate the scaffold and grow into the shape of the scaffold [234]. Such information obtained using DWDB-SOCT can help tissue engineers to optimize the scaffold material and fabrication process to achieve better cellular attachment and nutrition, as well as to monitor the health of the engineered tissue during the growth phase.

As seeded SF scaffolds can have highly varied cell distribution at the early growth stage, the SOCT imaging of seeded tissue scaffolds and the subsequent quantitative analysis can

be made more accurate by increasing the sections analyzed. A volumetric analysis of each scaffold would present quantitative results of higher statistical accuracy for comparison between seeded scaffolds.

7.5 Summary

DWDB-SOCT was used for monitoring cell proliferation in MEF seeded SF scaffolds. The scaffolds were harvested at time points of 1, 3 and 5 weeks for *in vivo* OCT imaging. These time points were chosen to give sufficient time for the fibroblasts to proliferate before imaging and analysis are carried out. The intensity-based OCT image of a control blank scaffold shows structural details like pore size and macro-channel width and depth. The DWDB-SOCT images of the blank scaffold and a MEF cell sample correctly depict the corresponding scatterer sizes associated with the scaffold material (small scatterers) and fibroblast cells (large scatterers). While the micro- and macro- scaffold structural features are clearly observed in the intensity-based OCT images, clear differentiation between the SF scaffold and fibroblast cells is only observed in the DWDB-SOCT images. The scatterer size quantification presented in chapter 6 was used to compare cell proliferation in the scaffolds at different time. The rate of cell proliferation is found to increase monotonically with time with the cell mass almost doubling at the 5 weeks time point. The interaction between the fibroblasts and the scaffold were also observed from the cell distributions in the DWDB-SOCT images. The quantity of fibroblasts at the surface and inside the scaffold gives valuable information on tissue culture conditions as well.

DWDB-SOCT, with the ability to differentiate MEF cells from SF scaffold material, can be used to monitor cell proliferation in cell seeded tissue scaffolds over time with high resolution. This is not possible with techniques like conventional optical microscopy, SEM imaging, X-ray μCT and MRI. DWDB-SOCT offers advantages such as the use of non-ionizing radiation, no contrast agents, non-invasive real-time imaging and the ability to image most biological tissues in tissue scaffolds. The morphology of SF scaffolds as well as cell proliferation and distribution within the scaffolds are imaged and quantified non-invasively in this first SOCT study of cell-proliferation monitoring in cell seeded SF scaffolds.

Chapter 8 Conclusions and Recommendations

8.1 Conclusions

A FD-OCT system is designed, built and characterized for OCT imaging. The FD-OCT system is based on a SLD source with a center wavelength of 840 nm to achieve a balance between axial resolution and imaging depth. The FD-OCT system is used to investigate the optical characteristics of normal and injured flexor tendons with load. Vertical and horizontal bands were observed in the OCT images of rest state tendon. Biomechanical tests of both normal and repaired tendons were performed by loading the samples with weights of up to 1 kg and imaged with the FD-OCT system. The OCT images of normal tendon under load show increasing brightness with the gradual disappearance of vertical bands caused by the straightening of the tendon crimp. Microtears within the tendon, while not visible to the naked eye, were observed in the OCT images after the maximum load of 10 N was removed. The 2 mm gap force and the ultimate tensile force of rabbit flexor tendons were found to be 5 N and 10 N, respectively. The nonlinear changes in the gap separation (above 2 mm) and the inelastic deformation of the repaired rabbit tendon under loads greater than 5 N were attributed to microtears forming near the suture joint. The OCT modality is suitable for the non-invasive quantification of tendon biomechanical properties and assessing the quality of suture repair techniques, and has great potential for monitoring the healing process in repaired tendons.

Using the FD-OCT system, microspheres of various sizes (0.5, 1, 10, 25 and 45 μm) are characterized with SOCT to investigate the correlation of spectral modulation

autocorrelation bandwidths to scatterer size. The spectroscopic analysis of the OCT axial profile is based on the DW method with comparisons to the conventional STFT method. A DB spectroscopic metric defined as the ratio of the 10% to 90% autocorrelation bandwidths gave the best contrast enhancement for scatterer size differentiation in the resulting spectroscopic image. The DWDB metric is found to exhibit a monotonic change with microsphere size. Simulation of the DWDB metric supports the experimental results and revealed a trade-off between the smallest detectable scatterer size and the maximum scatterer size in the linearity range of the DWDB metric for a specific light source optical bandwidth. Spectroscopic images of polystyrene microspheres and tonsil tissue samples based on the proposed DWDB metric showed clear differentiation between different-sized scatterers as compared to those determined with conventional STFT-calculated metric. Differences between connective tissue, epithelial and lymphoid cells, as well as between the upper and lower epithelium cells, of tonsil tissues are clearly observed in the SOCT images. The DWDB metric greatly improves the contrast in SOCT imaging and can aid the visualization of abnormal cell distribution in biological tissues and samples. Potential applications include the early detection of cell nuclear changes in tissue carcinogenesis, the monitoring of healing tendons and cell proliferation in tissue scaffolds.

The DWDB-SOCT is used to study the effect of BMSCs on flexor tendon healing in a rabbit model. Four different tendon seeding groups based on the types of stem cells introduced to the injury site, namely tisseel control (fibrin glue), 1M autologous BMSCs, 1M allogeneic BMSCs and 4M allogeneic BMSCs were established for comparison. The rabbit flexor tendons were harvested at two time points, 3 weeks and 8 weeks, for *ex vivo*

imaging. It is found that the organized collagen sections of normal tendon exhibit large scatterer characteristics in spectroscopic analysis, probably due to the densely packed collagen fibrils. Although conventional intensity-based OCT images showed significant structural differences between organized collagen and the healing site, differences between the tendon seeding groups cannot be discerned. The DWDB-SOCT images, however, were able to differentiate fibroblasts/stem cells and collagen by scatterer size. A scatterer size quantification parameter was defined and used to compare the fraction of large and small scatterers in the healing regions of the spectroscopic images. The small scatterers are of interest as they represent newly synthesized collagen in the healing sections of injured tendons. The results showed that BMSC seeded tendons achieved a greater degree of healing at the 3 weeks time point compared to fibrin glue control tendon. At the 8 weeks time point, however, all BMSC seeded tendons showed identical healing effects as the fibrin glue control. Allogeneic BMSCs were found to perform better than autologous BMSCs in terms of collagen synthesized at the repair site.

Lastly, the proposed DWDB-SOCT technique is used to monitor cell proliferation in MEF seeded SF scaffolds. The scaffolds were harvested at time points of 1, 3 and 5 weeks for *in vivo* OCT imaging. These time points were chosen to allow the fibroblasts sufficient time to proliferate before imaging and analysis are performed. The intensity-based OCT image of a control blank scaffold shows structural details like pore size and the macro-channel profile. The DWDB-SOCT images of the blank scaffold and a MEF cell sample correctly depict the corresponding scatterer sizes associated with the scaffold material (small scatterers) and fibroblast cells (large scatterers). While the micro- and macro- scaffold structural features

are clearly observed in the intensity-based OCT images, clear differentiation between the SF scaffold and fibroblast cells is only observed in the DWDB-SOCT images. The scatterer size quantification parameter is used to compare cell proliferation in the scaffolds at different time. The rate of cell proliferation is found to increase monotonically with time with the cell mass almost doubling at the 5 weeks time point. The interaction between the fibroblasts and the scaffold were also observed from the cell distributions in the DWDB-SOCT images. The quantity of fibroblasts at the surface and inside the scaffold can provide valuable information on tissue culture conditions.

8.2 Recommendations for Future Work

In this section, several recommendations for future research work are proposed. The recommendations are divided into three areas, namely the relationship between the light source bandwidth and scatterer size differentiation, sensitivity enhancement of scatter size differentiation and potential SOCT application areas.

8.2.1 Relationship between Light Source Bandwidth and Scatterer Size Differentiation

Simulation performed in this work showed that uniformly increasing the light source bandwidth increases the spectroscopic resolution of the DWDB-SOCT method. While the smallest detectable scatterer size improves with light source bandwidth, the corresponding linear range of the detectable scatterer sizes is drastically decreased. Alternatively this trade-off can potentially be overcome by using a suitably large bandwidth light source to

detect the smallest scatterer size and subsequently digitally limiting the light source bandwidth to achieve the desired linear monotonic range for quantifying the large scatterers. This has important implications as large bandwidth light sources can be used for all tissue imaging applications. Experimental investigations should be conducted to confirm the simulations and to determine the optimal method to vary light source bandwidth to obtain spectroscopic information on all scatterer sizes for various tissue imaging applications.

8.2.2 Sensitivity Enhancement of Scatterer Size Differentiation

During the calibration of the DWDB spectroscopic metric with respect to microsphere sizes, the metric values obtained for a single microsphere size have a large standard deviation. This is due to both hardware limitation and the microsphere control samples. Firstly, the OCT setup used in this work is based on a conventional Michelson interferometric setup. Minute fluctuations in the reference and sample arms due to temperature or vibrations can cause the interference fringes to fluctuate significantly, resulting in a larger variation in the value of the metric values. A common-path interferometric setup provides stability and minimizes fluctuations as light travels the same path in the reference and sample arms as they are incorporated together. An example of a common-path FD-OCT setup is illustrated in Figure 8-1. A common-path OCT system can achieve mainly *ex vivo* sample imaging, due to the need for the reference plane to be in contact or in close proximity to the sample. Secondly, the microsphere control samples used in this work are microspheres suspended in water. They represent a dynamic system

where the microspheres do not remain stationary during measurement. The statistical sum of the spectral modulations corresponding to the microsphere size is recorded. However the metric values obtained have large variation due to constant movement of the microspheres in the water. Despite so, differentiation between scatterer sizes can still be achieved. The advantage of using a dynamically moving calibration sample is the ability to perform spectroscopic measurements of particles in fluid as well. If the calibration samples used are fixed spatially, the statistical spread of the metric values can be reduced.

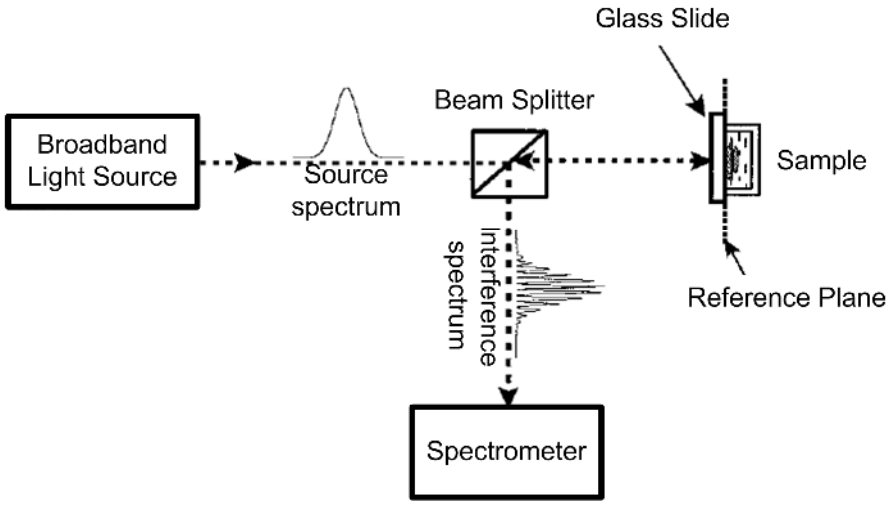

Figure 8-1: Common-path FD-OCT setup [235].

The DWDB analysis method developed in this work are more sensitive to scatterer size than previous methods based on STFT and a single autocorrelation bandwidth at 90%. Although the autocorrelation function is sensitive to spectral modulation, other methods can still be developed to describe the shape of the function more accurately. Identifying a

suitable alternative parameter to better quantify the shape information can further improve scatterer size differentiation.

8.2.3 Investigation of the Effect of Scatterer Concentration on the DWDB Spectroscopic Metric

Scatterer concentration is a sample parameter which affects the spectroscopic metric, and this is observed from the microsphere calibration experiments. Higher particle concentrations affect the spectroscopic metric adversely due to the limited inter-particle distance that is usually below the axial resolution limit of the OCT system (Table 5-1). The DWDB metric becomes inaccurate in relating to particle sizes when this happens. We observed in the spectroscopic metric calibration experiments that when using particles smaller than 0.5 μm, the metric values become more indicative of larger particles, similar to the results that Adler et al. reported [115]. Hence, in order to investigate this phenomenon, experiments should be conducted to study the effect of inter-particle spacings in relation to scatterer concentration on the DWDB spectroscopic metric.

8.2.4 Investigation of the Effect of Multiple Scattering on the DWDB Spectroscopic Metric

In densely scattering samples, high particle/scatterer concentrations affect the spectroscopic metric adversely when the inter-particle spacing is less than the axial resolution of the OCT system. In such cases, such as the normal tendon sample in Figure 6-9, multiple hues are

observed in the SOCT image of a uniform sample and this is possibly the effect of multiple scattering due to densely packed collagen fibers. Spectroscopic analysis should be excluded from these sections. A better understanding of the effect of multiple scattering on the spectroscopic metric and how to overcome it should be conducted in future experiments.

8.2.5 Potential DWDB-SOCT Applications

The applications of the DWDB-SOCT method to epithelial tissue, healing tendons and seeded tissue scaffolds were successfully carried out in this thesis. The method enables the differentiation of tissue scatterer sizes for contrast enhancement in the spectroscopic image for direct visualization as well as quantification of the tissue scatterers detected within the imaging volume. As such, applications requiring the detection and measurement of particle sizes above or below the sample mean in static or dynamic environments can benefit from the DWDB-SOCT method.

For example, the main commercial uses of *in vivo* OCT imaging involve retinal imaging and arterial imaging. Commercial OCT systems have been developed for these applications but only structural information, not functional information, are obtained. The DWDB-SOCT technique can be incorporated into the image processing algorithms of these systems to give the additional functionality of tissue scatterer differentiation at no extra equipment cost. Furthermore, *in vivo* OCT systems can be used for early cancer detection, where abnormal cells in epithelial tissue can be detected and monitored for possible malignancy. Current *in vivo* OCT systems provide only structural information, which do not provide

sufficient contrast for early cancer detection until cancerous cells have reached a later stage of development.

The DWDB-SOCT method can be used for imaging particles that are dynamically moving in a fluid environment. The statistical sum of the spectral modulations corresponding to the particles sizes can be measured even when the particles are moving around. The spectral modulations can then be related to particle sizes. Thus, potential applications like detection of pathogens in waste-water treatment, or the monitoring of micro- or nano-particles growth on a substrate can be achieved using the DWDB-SOCT method.

Author's Publications

Journal Papers:

Published

1. T. H. Chow, K. M. Tan, B. K. Ng, S. G. Razul, **C. M. Tay**, T. F. Chia and W. T. Poh, "Diagnosis of virus infection in orchid plants with high-resolution optical coherence tomography," *Journal of Biomedical Optics* **14**(1), 014006-014006 (2009).

2. M. J. J. Liu, S. M. Chou, C. K. Chua, **C. M. B. Tay** and B. K. Ng, "The development of silk fibroin scaffolds using an indirect rapid prototyping approach: Morphological analysis and cell growth monitoring by spectral-domain optical coherence tomography," Article in Press, *Medical Engineering and Physics Journal* (2011).

3. **B. C. M. Tay**, B. K. Ng, T. K. S. Loh, "Dual window dual bandwidth spectroscopic optical coherence tomography metric for qualitative scatterer size differentiation in tissues", accepted by IEEE Transactions in Biomedical Engineering (May 2012).

In preparation for submission

4. **B. C. M. Tay**, B. K. Ng, M. He, W. T. A. Gan, A. K. S. Chong, "Monitoring the effect of bone marrow-derived mesenchymal stem cells on flexor tendon healing

using spectroscopic optical coherence tomography", currently under preparation for submission.

5. **B. C. M. Tay**, B. K. Ng, J. M. J. Liu, S. M. Chou and C. K. Chua, "Monitoring cell proliferation in silk fibroin scaffolds using spectroscopic optical coherence tomography", currently under preparation for submission.

Conference Papers:

Published

1. **C.-M. B. Tay**, T.-H. Chow, B.-K. Ng, M. He, W.-T. A. Gan and K.-S. A. Chong, "Monitoring of sutured flexor tendons using Fourier domain optical coherence tomography," in SPIE Photonics West 2010, pp. 75542F-75545, San Francisco, California, USA (2010).

2. M. J. J. Liu, S. M. Chou, C. K. Chua, **C. M. B. Tay** and B. K. Ng, "The study of micro- and macro-structural features of silk fibroin scaffolds," in Proceedings of the 1st International Symposium on Bioengineering, ISOB 2011, pp. 330-338, Singapore (2011).

References

1. C. M. C. Tempany, and B. J. McNeil, "Advances in Biomedical Imaging," JAMA: The Journal of the American Medical Association **285**, 562-567 (2001).
2. P. N. Prasad, *Introduction to biophotonics* (Wiley-Interscience, Hoboken, NJ, 2003).
3. A. R. Webb, *Introduction to biomedical imaging* (Wiley, Hoboken, New Jersey, 2003).
4. K. Licha, and C. Olbrich, "Optical imaging in drug discovery and diagnostic applications," Advanced Drug Delivery Reviews **57**, 1087-1108 (2005).
5. J. G. Fujimoto, "Optical coherence tomography for ultrahigh resolution in vivo imaging," Nature Biotechnology **21**, 1361-1367 (2003).
6. C. Balas, "Review of biomedical optical imaging - A powerful, non-invasive, non-ionizing technology for improving in vivo diagnosis," Measurement Science and Technology **20** (2009).
7. W. R. Hendee, "Cross sectional medical imaging: a history," Radiographics : a review publication of the Radiological Society of North America, Inc **9**, 1155-1180 (1989).
8. P. N. T. Wells, "Ultrasound imaging," Physics in Medicine and Biology **51**, R83-R98 (2006).
9. J. G. Fujimoto, and D. L. Farkas, *Biomedical optical imaging* (Oxford University Press, Oxford; New York, 2009).
10. B. Taouli, M. Losada, A. Holland, and G. Krinsky, "Magnetic resonance imaging of hepatocellular carcinoma," Gastroenterology **127**, S144-S152 (2004).
11. J. W. Bailet, J. A. Sercarz, E. Abemayor, Y. Anzai, R. B. Lufkin, and C. K. Hoh, "The use of positron emission tomography for early detection of recurrent head and neck squamous cell carcinoma in postradiotherapy patients," Laryngoscope **105**, 135-139 (1995).
12. L. Kostakoglu, and S. J. Goldsmith, "PET in the assessment of therapy response in patients with carcinoma of the head and neck and of the esophagus," Journal of Nuclear Medicine **45**, 56-68 (2004).
13. F. R. Miller, D. Hussey, M. Beeram, T. Eng, H. S. McGuff, and R. A. Otto, "Positron emission tomography in the management of unknown primary head and neck carcinoma," Archives of Otolaryngology - Head and Neck Surgery **131**, 626-629 (2005).
14. H. Schöder, and S. M. Larson, "Positron emission tomography for prostate, bladder, and renal cancer," Seminars in Nuclear Medicine **34**, 274-292 (2004).
15. R. A. Robb, "Biomedical Imaging: Past, Present and Predictions " Mayo Clinic College of Medicine.
16. M. Moller, P. Kalebo, G. Tidebrant, T. Movin, and J. Karlsson, "The ultrasonographic appearance of the ruptured Achilles tendon during healing: A longitudinal evaluation of surgical and nonsurgical treatment, with comparisons to MRI appearance," Knee Surgery, Sports Traumatology, Arthroscopy **10**, 49-56 (2002).
17. G. Bosch, P. René van Weeren, A. Barneveld, and H. T. M. van Schie, "Computerised analysis of standardised ultrasonographic images to monitor the repair of surgically created core lesions in equine superficial digital flexor tendons following treatment with intratendinous platelet rich plasma or placebo," Veterinary Journal **187**, 92-98 (2011).

18. K. Jeyapalan, M. A. Bisson, J. J. Dias, Y. Griffin, and R. Bhatt, "The role of ultrasound in the management of flexor tendon injuries," Journal of Hand Surgery: European Volume **33**, 430-434 (2008).
19. A. Shalabi, "Magnetic resonance imaging in chronic achilles tendinopathy," Acta Radiologica **45**, 1-45 (2004).
20. B. A. Kumar, A. R. Tolat, G. Threepuraneni, and B. Jones, "The role of magnetic resonance imaging in late presentation of isolated injuries of the flexor digitorum profundus tendon in the finger," Journal of Hand Surgery **25 B**, 95-97 (2000).
21. U. G. Longo, A. Lamberti, N. Maffulli, and V. Denaro, "Tissue engineered biological augmentation for tendon healing: A systematic review," British Medical Bulletin **98**, 31-59 (2011).
22. A. K. S. Chong, A. D. Ang, J. C. H. Goh, J. H. P. Hui, A. Y. T. Lim, E. H. Lee, and B. H. Lim, "Bone marrow-derived mesenchymal stem cells influence early tendon-healing in a rabbit Achilles tendon model," Journal of Bone and Joint Surgery - Series A **89**, 74-81 (2007).
23. G. H. van Lenthe, H. Hagenmüller, M. Bohner, S. J. Hollister, L. Meinel, and R. Müller, "Nondestructive micro-computed tomography for biological imaging and quantification of scaffold-bone interaction in vivo," Biomaterials **28**, 2479-2490 (2007).
24. V. Karageorgiou, and D. Kaplan, "Porosity of 3D biomaterial scaffolds and osteogenesis," Biomaterials **26**, 5474-5491 (2005).
25. S. V. Madihally, and H. W. T. Matthew, "Porous chitosan scaffolds for tissue engineering," Biomaterials **20**, 1133-1142 (1999).
26. H. Xu, S. F. Othman, L. Hong, I. A. Peptan, and R. L. Magin, "Magnetic resonance microscopy for monitoring osteogenesis in tissue-engineered construct in vitro," Physics in Medicine and Biology **51**, 719-732 (2006).
27. H. Xu, S. F. Othman, and R. L. Magin, "Monitoring Tissue Engineering Using Magnetic Resonance Imaging," Journal of Bioscience and Bioengineering **106**, 515-527 (2008).
28. F. H. White, and K. Gohari, "Cellular and nuclear volumetric alterations during differentiation of normal hamster cheek pouch epithelium," Archives of Dermatological Research **273**, 307-318 (1982).
29. F. H. White, R. M. Codd, and K. Gohari, "An ultrastructural morphometric study of cellular and nuclear volume alterations during experimental oral carcinogenesis," Journal of submicroscopic cytology **17**, 481-493 (1985).
30. A. H. M. Shabana, N. G. El-Labban, and K. W. Lee, "Morphometric analysis of basal cell layer in oral premalignant white lesions and squamous cell carcinoma," Journal of Clinical Pathology **40**, 454-458 (1987).
31. Y. Jin, F. H. White, and L. Yang, "A histological morphometric study of nuclear size in benign and malignant neoplasms of the human cheek," Histopathology **23**, 271-274 (1993).
32. W. Jung, J. Zhang, J. Chung, P. Wilder-Smith, M. Brenner, J. S. Nelson, and Z. Chen, "Advances in oral cancer detection using optical coherence tomography," IEEE Journal on Selected Topics in Quantum Electronics **11**, 811-816 (2005).

33. M.-T. Tsai, C.-K. Lee, H.-C. Lee, H.-M. Chen, C.-P. Chiang, Y.-M. Wang, and C.-C. Yang, "Differentiating oral lesions in different carcinogenesis stages with optical coherence tomography," Journal of Biomedical Optics **14**, 044028-044027 (2009).
34. D. Huang, E. A. Swanson, C. P. Lin, J. S. Schuman, W. G. Stinson, W. Chang, M. R. Hee, T. Flotte, K. Gregory, C. A. Puliafito, and J. G. Fujimoto, "Optical coherence tomography," Science **254**, 1178-1181 (1991).
35. B. E. Bouma, and G. J. Tearney, *Handbook of optical coherence tomography* (Marcel Dekker, New York, 2002).
36. W. Drexler, and J. G. Fujimoto, "Optical coherence tomography technology and applications," (Springer, 2008), http://dx.doi.org/10.1007/978-3-540-77550-8.
37. J. G. Fujimoto, M. E. Brezinski, G. J. Tearney, S. A. Boppart, B. Bouma, M. R. Hee, J. F. Southern, and E. A. Swanson, "Optical biopsy and imaging using optical coherence tomography," Nature Medicine **1**, 970-972 (1995).
38. A. L. Oldenburg, C. Xu, and S. A. Boppart, "Spectroscopic optical coherence tomography and microscopy," IEEE Journal on Selected Topics in Quantum Electronics **13**, 1629-1640 (2007).
39. F. E. Robles, Y. Zhu, J. Lee, S. Sharma, and A. Wax, "Detection of early colorectal cancer development in the azoxymethane rat carcinogenesis model with Fourier domain low coherence interferometry," Biomed. Opt. Express **1**, 736-745 (2010).
40. J. W. Strickland, "The scientific basis for advances in flexor tendon surgery," Journal of Hand Therapy **18**, 94-111 (2005).
41. A. T. Yeh, B. Kao, W. G. Jung, Z. Chen, J. S. Nelson, and B. J. Tromberg, "Imaging wound healing using optical coherence tomography and multiphoton microscopy in an in vitro skin-equivalent tissue model," Journal of Biomedical Optics **9**, 248-253 (2004).
42. L. V. Wang, and H.-i. Wu, *Biomedical optics : principles and imaging* (Wiley-Interscience, Hoboken, N.J., 2007).
43. R. R. Alfano, S. G. Demos, and S. K. Gayen, "Advances in Optical Imaging of Biomedical Media," Annals of the New York Academy of Sciences **820**, 248-271 (1997).
44. A. Diaspro, *Confocal and two-photon microscopy : foundations, applications, and advances* (Wiley-Liss, New York, 2002).
45. M. C. Skala, J. M. Squirrell, K. M. Vrotsos, J. C. Eickhoff, A. Gendron-Fitzpatrick, K. W. Eliceiri, and N. Ramanujam, "Multiphoton microscopy of endogenous fluorescence differentiates normal, precancerous, and cancerous squamous epithelial tissues," Cancer Research **65**, 1180-1186 (2005).
46. F. Helmchen, and W. Denk, "Deep tissue two-photon microscopy," Nature Methods **2**, 932-940 (2005).
47. W. R. Zipfel, R. M. Williams, and W. W. Webb, "Nonlinear magic: Multiphoton microscopy in the biosciences," Nature Biotechnology **21**, 1369-1377 (2003).
48. A. Diaspro, and M. Robello, "Two-photon excitation of fluorescence for three-dimensional optical imaging of biological structures," Journal of Photochemistry and Photobiology B: Biology **55**, 1-8 (2000).
49. P. J. Campagnola, and L. M. Loew, "Second-harmonic imaging microscopy for visualizing biomolecular arrays in cells, tissues and organisms," Nature Biotechnology **21**, 1356-1360 (2003).

50. P. J. Campagnola, H. A. Clark, W. A. Mohler, A. Lewis, and L. M. Loew, "Second-harmonic imaging microscopy of living cells," Journal of Biomedical Optics **6**, 277-286 (2001).
51. P. J. Campagnola, A. C. Millard, M. Terasaki, P. E. Hoppe, C. J. Malone, and W. A. Mohler, "Three-dimensional high-resolution second-harmonic generation imaging of endogenous structural proteins in biological tissues," Biophysical Journal **82**, 493-508 (2002).
52. J. A. Palero, H. S. De Bruijn, A. Van Der Ploeg-Van Den Heuvel, H. J. C. M. Sterenborg, and H. C. Gerritsen, "In vivo nonlinear spectral imaging in mouse skin," Optics Express **14**, 4395-4402 (2006).
53. A. Zoumi, A. Yeh, and B. J. Tromberg, "Imaging cells and extracellular matrix in vivo by using second-harmonic generation and two-photon excited fluorescence," Proceedings of the National Academy of Sciences of the United States of America **99**, 11014-11019 (2002).
54. D. A. Boas, D. H. Brooks, E. L. Miller, C. A. DiMarzio, M. Kilmer, R. J. Gaudette, and Q. Zhang, "Imaging the body with diffuse optical tomography," IEEE Signal Processing Magazine **18**, 57-75 (2001).
55. A. P. Gibson, J. C. Hebden, and S. R. Arridge, "Recent advances in diffuse optical imaging," Physics in Medicine and Biology **50**, R1-R43 (2005).
56. M. Xu, and L. V. Wang, "Photoacoustic imaging in biomedicine," Review of Scientific Instruments **77** (2006).
57. H. F. Zhang, K. Maslov, G. Stoica, and L. V. Wang, "Functional photoacoustic microscopy for high-resolution and noninvasive in vivo imaging," Nature Biotechnology **24**, 848-851 (2006).
58. OBEL, "Introduction to OCT, "http://obel.ee.uwa.edu.au/research/oct/intro/"," (University of Western Australia, 2011).
59. N. N. Boustany, S. A. Boppart, and V. Backman, "Microscopic imaging and spectroscopy with scattered light," Annual Review of Biomedical Engineering **12**, 285-314 (2010).
60. M. Abramowitz, "Microscope Basics and Beyond, http://micro.magnet.fsu.edu/primer/pdfs/basicsandbeyond.pdf," (2003).
61. P. SciCast, "Lenses, "http://www.planet-scicast.com/experiment.cfm?cit_id=2681"," (2008).
62. Luis Carlos Junqueira, Jose Carneiro, and R. O. Kelley, "Basic Histology," (Appleton & Lange, 1998).
63. R. L. Price, and W. G. J. Jerome, eds. *Basic Confocal Microscopy* (Springer, New York, 2011).
64. M. C. Pierce, D. J. Javier, and R. Richards-Kortum, "Optical contrast agents and imaging systems for detection and diagnosis of cancer," International Journal of Cancer **123**, 1979-1990 (2008).
65. L. T. Perelman, V. Backman, M. Wallace, G. Zonios, R. Manoharan, A. Nusrat, S. Shields, M. Seiler, C. Lima, T. Hamano, I. Itzkan, J. Van Dam, J. M. Crawford, and M. S. Feld, "Observation of periodic fine structure in reflectance from biological tissue: A new technique for measuring nuclear size distribution," Physical Review Letters **80**, 627-630 (1998).

66. I. Georgakoudi, B. C. Jacobson, J. Van Dam, V. Backman, M. B. Wallace, M. G. Müller, Q. Zhang, K. Badizadegan, D. Sun, G. A. Thomas, L. T. Perelman, and M. S. Feld, "Fluorescence, reflectance, and light-scattering spectroscopy for evaluating dysplasia in patients with Barrett's esophagus," Gastroenterology **120**, 1620-1629 (2001).
67. R. Graf, and A. Wax, "Nuclear morphology measurements using Fourier domain low coherence interferometry," Opt. Express **13**, 4693-4698 (2005).
68. F. E. Robles, and A. Wax, "Measuring morphological features using light-scattering spectroscopy and Fourier-domain low-coherence interferometry," Optics Letters **35**, 360-362 (2010).
69. A. Wax, C. Yang, and J. A. Izatt, "Fourier-domain low-coherence interferometry for light-scattering spectroscopy," Opt. Lett. **28**, 1230-1232 (2003).
70. A. Wax, C. Yang, R. R. Dasari, and M. S. Feld, "Measurement of angular distributions by use of low-coherence interferometry for light-scattering spectroscopy," Optics Letters **26**, 322-324 (2001).
71. C. Pitris, M. E. Brezinski, B. E. Bouma, G. J. Tearney, J. F. Southern, and J. G. Fujimoto, "High resolution imaging of the upper respiratory tract with optical coherence tomography: A feasibility study," American Journal of Respiratory and Critical Care Medicine **157**, 1640-1644 (1998).
72. R. Leitgeb, C. K. Hitzenberger, and A. F. Fercher, "Performance of fourier domain vs. time domain optical coherence tomography," Optics Express **11**, 889-894 (2003).
73. M. Wojtkowski, R. Leitgeb, A. Kowalczyk, T. Bajraszewski, and A. F. Fercher, "In vivo human retinal imaging by Fourier domain optical coherence tomography," Journal of Biomedical Optics **7**, 457-463 (2002).
74. J. F. De Boer, B. Cense, B. H. Park, M. C. Pierce, G. J. Tearney, and B. E. Bouma, "Improved signal-to-noise ratio in spectral-domain compared with time-domain optical coherence tomography," Optics Letters **28**, 2067-2069 (2003).
75. M. A. Choma, M. V. Sarunic, C. Yang, and J. A. Izatt, "Sensitivity advantage of swept source and Fourier domain optical coherence tomography," Optics Express **11**, 2183-2189 (2003).
76. S. H. Yun, G. J. Tearney, B. E. Bouma, B. H. Park, and J. F. De Boer, "High-speed spectral-domain optical coherence tomography at 1.3 um wavelength," Optics Express **11**, 3598-3604 (2003).
77. M. E. Brezinski, *Optical Coherence Tomography: Principles and Applications* (Academic Press, 2006).
78. G. Häusler, and M. W. Lindner, ""Coherence radar" and "spectral radar" - New tools for dermatological diagnosis," Journal of Biomedical Optics **3**, 21-31 (1998).
79. R. Leitgeb, W. Drexler, A. Unterhuber, B. Hermann, T. Bajraszewski, T. Le, A. Stingl, and A. Fercher, "Ultrahigh resolution Fourier domain optical coherence tomography," Opt. Express **12**, 2156-2165 (2004).
80. C. Mason, and et al., "The potential of optical coherence tomography in the engineering of living tissue," Physics in Medicine and Biology **49**, 1097 (2004).
81. X. Li, S. Martin, C. Pitris, R. Ghanta, D. L. Stamper, M. Harman, J. G. Fujimoto, and M. E. Brezinski, "High-resolution optical coherence tomographic imaging of osteoarthritic cartilage during open knee surgery," Arthritis research & therapy. **7** (2005).

82. X. D. Li, S. A. Boppart, J. Van Dam, H. Mashimo, M. Mutinga, W. Drexler, M. Klein, C. Pitris, M. L. Krinsky, M. E. Brezinski, and J. G. Fujimoto, "Optical coherence tomography: Advanced technology for the endoscopic imaging of Barrett's esophagus," Endoscopy **32**, 921-930 (2000).
83. U. Mahmood, J. Ridgway, R. Jackson, S. Guo, J. Su, W. Armstrong, T. Shibuya, R. Crumley, Z. Chen, and B. Wong, "In vivo optical coherence tomography of the nasal mucosa," American Journal of Rhinology **20**, 155-159 (2006).
84. C. Pitris, C. Jesser, S. A. Boppart, D. Stamper, M. E. Brezinski, and J. G. Fujimoto, "Feasibility of optical coherence tomography for high-resolution imaging of human gastrointestinal tract malignancies," Journal of Gastroenterology **35**, 87-92 (2000).
85. C. Pitris, T. Ko, W. Drexler, R. Ghanta, X. Li, C. Chudoba, I. Hartl, J. G. Fujimoto, and M. Weinstein, "Ultrahigh-resolution in vivo versus ex vivo OCT imaging and tissue preservation," in *Proceedings of SPIE - The International Society for Optical Engineering*, V. V. Tuchin, J. A. Izatt, and J. G. Fujimoto, eds. (San Jose, CA, 2001), pp. 170-173.
86. C. Pitris, K. T. Saunders, J. G. Fujimoto, and M. E. Brezinski, "High-resolution imaging of the middle ear with optical coherence tomography: A feasibility study," Archives of Otolaryngology - Head and Neck Surgery **127**, 637-642 (2001).
87. W. B. Armstrong, J. M. Ridgway, D. E. Vokes, S. Guo, J. Perez, R. P. Jackson, M. Gu, J. Su, R. L. Crumley, T. Y. Shibuya, U. Mahmood, Z. Chen, and B. J. F. Wong, "Optical coherence tomography of laryngeal cancer," Laryngoscope **116**, 1107-1113 (2006).
88. A. L. Clark, A. Gillenwater, R. Alizadeh-Naderi, A. K. El-Naggar, and R. Richards-Kortum, "Detection and diagnosis of oral neoplasia with an optical coherence microscope," Journal of Biomedical Optics **9**, 1271-1280 (2004).
89. T. Gambichler, A. Orlikov, R. Vasa, G. Moussa, K. Hoffmann, M. Stücker, P. Altmeyer, and F. G. Bechara, "In vivo optical coherence tomography of basal cell carcinoma," Journal of Dermatological Science **45**, 167-173 (2007).
90. M. Kraft, H. Glanz, S. Von Gerlach, H. Wisweh, H. Lubatschowski, and C. Arens, "Clinical value of optical coherence tomography in laryngology," Head and Neck **30**, 1628-1635 (2008).
91. A. M. Sergeev, V. M. Gelikonov, G. V. Gelikonov, F. I. Feldchtein, R. V. Kuranov, N. D. Gladkova, N. M. Shakhova, L. B. Snopova, A. V. Shakhov, I. A. Kuznetzova, A. N. Denisenko, V. V. Pochinko, Y. P. Chumakov, and O. S. Streltzova, "In vivo endoscopic OCT imaging of precancer and cancer states of human mucosa," Optics Express **1**, 432-440 (1997).
92. M. T. Tsai, H. C. Lee, C. K. Lee, C. H. Yu, H. M. Chen, C. P. Chiang, C. C. Chang, Y. M. Wang, and C. C. Yang, "Effective indicators for diagnosis of oral cancer using optical coherence tomography," Optics Express **16**, 15847-15862 (2008).
93. P. Wilder-Smith, W. G. Jung, M. Brenner, K. Osann, H. Beydoun, D. Messadi, and Z. Chen, "In vivo optical coherence tomography for the diagnosis of oral malignancy," Lasers in Surgery and Medicine **35**, 269-275 (2004).
94. B. J. F. Wong, R. P. Jackson, S. Guo, J. M. Ridgway, U. Mahmood, J. Su, T. Y. Shibuya, R. L. Crumley, M. Gu, W. B. Armstrong, and Z. Chen, "In vivo optical coherence tomography of the human larynx: Normative and benign pathology in 82 patients," Laryngoscope **115**, 1904-1911 (2005).

95. C. Zhou, A. D. Aguirre, Y. Wang, B. Bryan, T.-H. Tsai, J. L. Connolly, and J. G. Fujimoto, "Ex vivo imaging of human pathologies with integrated optical coherence tomography (OCT) and optical coherence microscopy (OCM)," in *Optical Coherence Tomography and Coherence Domain Optical Methods in Biomedicine XIII*(SPIE, San Jose, CA, USA, 2009), pp. 71680N-71688.
96. B. J. Vakoc, R. M. Lanning, J. A. Tyrrell, T. P. Padera, L. A. Bartlett, T. Stylianopoulos, L. L. Munn, G. J. Tearney, D. Fukumura, R. K. Jain, and B. E. Bouma, "Three-dimensional microscopy of the tumor microenvironment in vivo using optical frequency domain imaging," Nature Medicine (2009).
97. J. Gallwas, L. Turk, K. Friese, and C. Dannecker, "Optical coherence tomography as a non-invasive imaging technique for preinvasive and invasive neoplasia of the uterine cervix," Ultrasound in Obstetrics and Gynecology **36**, 624-629 (2010).
98. Z. Chen, T. E. Milner, D. Dave, and J. S. Nelson, "Optical Doppler tomographic imaging of fluid flow velocity in highly scattering media," Optics Letters **22**, 64-66 (1997).
99. Z. Chen, T. E. Milner, S. Srinivas, X. Wang, A. Malekafzali, M. J. C. Van Gemert, and J. S. Nelson, "Noninvasive imaging of in vivo blood flow velocity using optical Doppler tomography," Optics Letters **22**, 1119-1121 (1997).
100. Z. Chen, Y. Zhao, S. M. Srinivas, J. S. Nelson, N. Prakash, and R. D. Frostig, "Optical Doppler tomography," IEEE Journal on Selected Topics in Quantum Electronics **5**, 1134-1142 (1999).
101. J. A. Izatt, M. D. Kulkarni, S. Yazdanfar, J. K. Barton, and A. J. Welch, "In vivo bidirectional color Doppler flow imaging of picoliter blood volumes using optical coherence tomography," Optics Letters **22**, 1439-1441 (1997).
102. R. A. Leitgeb, L. Schmetterer, W. Drexler, A. F. Fercher, R. J. Zawadzki, and T. Bajraszewski, "Real-time assessment of retinal blood flow with ultrafast acquisition by color Doppler Fourier domain optical coherence tomography," Optics Express **11**, 3116-3121 (2003).
103. S. Yazdanfar, A. M. Rollins, and J. A. Izatt, "Imaging and velocimetry of the human retinal circulation with color Doppler optical coherence tomography," Optics Letters **25**, 1448-1450 (2000).
104. M. R. Hee, D. Huang, E. A. Swanson, and J. G. Fujimoto, "Polarization-sensitive low-coherence reflectometer for birefringence characterization and ranging," J. Opt. Soc. Am. B **9**, 903-908 (1992).
105. J. F. De Boer, S. M. Srinivas, B. H. Park, T. H. Pham, Z. Chen, T. E. Milner, and J. S. Nelson, "Polarization effects in optical coherence tomography of various biological tissues," IEEE Journal on Selected Topics in Quantum Electronics **5**, 1200-1204 (1999).
106. S. D. Martin, N. A. Patel, S. B. Adams, M. J. Roberts, S. Plummer, D. L. Stamper, M. E. Brezinski, and J. G. Fujimoto, "New technology for assessing microstructural components of tendons and ligaments," International Orthopaedics **27**, 184-189 (2003).
107. S. J. Matcher, C. P. Winlove, and S. V. Gangnus, "Polarization-sensitive OCT applied to equine tendon and bovine intervertebral disk," in *Proceedings of SPIE - The International Society for Optical Engineering*, V. V. Tuchin, J. A. Izatt, and J. G. Fujimoto, eds. (San Jose, CA, 2003), pp. 360-365.

108. S. J. Matcher, C. P. Winlove, and S. V. Gangnus, "The collagen structure of bovine intervertebral disc studied using polarization-sensitive optical coherence tomography," Physics in Medicine and Biology **49**, 1295-1306 (2004).
109. N. Kemp, H. Zaatari, J. Park, H. G. Rylander Iii, and T. Milner, "Form-biattenuance in fibrous tissues measured with polarization-sensitive optical coherence tomography (PS-OCT)," Opt. Express **13**, 4611-4628 (2005).
110. M. Ahearne, P. O. Bagnaninchi, Y. Yang, and A. J. El Haj, "Online monitoring of collagen fibre alignment in tissue-engineered tendon by PSOCT," Journal of tissue engineering and regenerative medicine **2**, 521-524 (2008).
111. P. O. Bagnaninchi, D. Churmakov, M. Bonesi, Y. Yang, C. Phelan, N. Maffulli, I. Meglinski, and A. El Haj, "Optical properties of human tendons characterized by PSOCT and their relation to tendinopathy: A clinical study," in *Progress in Biomedical Optics and Imaging - Proceedings of SPIE*(San Jose, CA, 2008).
112. M. R. Strakowski, J. PluciÅ„ski, M. Jedrzejewska-Szczerska, R. Hypszer, M. Maciejewski, and B. B. Kosmowski, "Polarization sensitive optical coherence tomography for technical materials investigation," Sensors and Actuators, A: Physical **142**, 104-110 (2008).
113. P. O. Bagnaninchi, Y. Yang, M. Bonesi, G. Maffulli, C. Phelan, I. Meglinski, A. El Haj, and N. Maffulli, "In-depth imaging and quantification of degenerative changes associated with Achilles ruptured tendons by polarization-sensitive optical coherence tomography," Physics in Medicine and Biology **55**, 3777-3787 (2010).
114. U. Morgner, W. Drexler, F. X. Kartner, X. D. Li, C. Pitris, E. P. Ippen, and J. G. Fujimoto, "Spectroscopic optical coherence tomography," Optics Letters **25**, 111-113 (2000).
115. D. C. Adler, T. H. Ko, P. R. Herz, and J. G. Fujimoto, "Optical coherence tomography contrast enhancement using spectroscopic analysis with spectral autocorrelation," Optics Express **12**, 5487-5501 (2004).
116. F. Robles, R. N. Graf, and A. Wax, "Dual window method for processing spectroscopic optical coherence tomography signals with simultaneously high spectral and temporal resolution," Opt. Express **17**, 6799-6812 (2009).
117. R. N. Graf, F. E. Robles, X. Chen, and A. Wax, "Detecting precancerous lesions in the hamster cheek pouch using spectroscopic white-light optical coherence tomography to assess nuclear morphology via spectral oscillations," Journal of Biomedical Optics **14**, 064030 (2009).
118. X. Liang, B. W. Graf, and S. A. Boppart, "Imaging engineered tissues using structural and functional optical coherence tomography," Journal of Biophotonics **2**, 643-655 (2009).
119. A. M. Rich, M. I. Nataatmadja, and P. C. Reade, "Basal cell nuclear size in experimental oral mucosal carcinogenesis," British Journal of Cancer **64**, 96-98 (1991).
120. G. L. Tipoe, F. H. White, and C. J. Pritchett, "A morphometric study of histological variations during cellular differentiation of normal human colorectal epithelium," Journal of Anatomy **181**, 189-197 (1992).
121. C. Giardina, D. M. Caniglia, M. D'Aprile, T. Lettini, G. Serio, T. Cipriani, R. Ricco, and V. Pesce Delfino, "Nuclear morphometry in squamous cell carcinoma (SCC) of the tongue," European Journal of Cancer Part B: Oral Oncology **32**, 91-96 (1996).

122. A. M. Marchevsky, A. A. Gal, S. Shah, and M. N. Koss, "Morphometry confirms the presence of considerable nuclear size overlap between "small cells" and "large cells" in high-grade pulmonary neuroendocrine neoplasms," American Journal of Clinical Pathology **116**, 466-472 (2001).
123. M. Martano, B. Restucci, O. Paciello, V. Russo, and P. Maiolino, "Nuclear morphometry in canine acanthomatous ameloblastomas and squamous cell carcinomas," European Journal of Histochemistry **50**, 125-130 (2006).
124. V. V. Tuchin, *Tissue Optics : Light Scattering Methods and Instruments for Medical Diagnosis* (SPIE International Society for Optical Engineering, 2006).
125. Y.-Y. Huang, M. Hamblin, and A. C.-H. Chen, "Low-level laser therapy: an emerging clinical paradigm," (SPIE Newsroom, 2009), DOI: 10.1117/2.1200906.1669.
126. P. H. Tomlins, and R. K. Wang, "Theory, developments and applications of optical coherence tomography," Journal of Physics D: Applied Physics **38**, 2519-2535 (2005).
127. E. Hecht, *Optics* (Addison-Wesley, Reading, Mass, 2002).
128. M. Wojtkowski, B. L. Sikorski, I. Gorczynska, M. Gora, M. Szkulmowski, D. Bukowska, J. KaÅ‚uzny, J. G. Fujimoto, and A. Kowalczyk, "Comparison of reflectivity maps and outer retinal topography in retinal disease by 3-D Fourier domain optical coherence tomography," Optics Express **17**, 4189-4207 (2009).
129. B. Potsaid, I. Gorczynska, V. J. Srinivasan, Y. Chen, J. Jiang, A. Cable, and J. G. Fujimoto, "Ultrahigh speed spectral / Fourier domain OCT ophthalmic imaging at 70,000 to 312,500 axial scans per second," Optics Express **16**, 15149-15169 (2008).
130. A. M. Rollins, M. D. Kulkarni, S. Yazdanfar, R. Ung-Arunyawee, and J. A. Izatt, "In vivo video rate optical coherence tomography," Optics Express **3**, 219-229 (1998).
131. N. A. Nassif, B. Cense, B. H. Park, M. C. Pierce, S. H. Yun, B. E. Bouma, G. J. Tearney, T. C. Chen, and J. F. De Boer, "In vivo high-resolution video-rate spectral-domain optical coherence tomography of the human retina and optic nerve," Optics Express **12**, 367-376 (2004).
132. R. Bracewell, *The Fourier Transform and Its Applications* (McGraw-Hill Science/Engineering/Math, 1999).
133. D. Huang, J. Wang, C. P. Lin, C. A. Puliafito, and J. G. Fujimoto, "Micron-resolution ranging of cornea anterior chamber by optical reflectometry," Lasers in Surgery and Medicine **11**, 419-425 (1991).
134. Nikon, "MicroscopyU, (http://www.microscopyu.com/)."
135. F. E. Robles, R. N. Graf, and A. Wax, "Dual window method for processing spectroscopic optical coherence tomography signals with high spectral and spatial resolution," in *Progress in Biomedical Optics and Imaging - Proceedings of SPIE*(San Jose, CA, 2009).
136. F. E. Robles, C. Wilson, G. Grant, and A. Wax, "Molecular imaging true-colour spectroscopic optical coherence tomography," Nature Photonics **5**, 744-747 (2011).
137. C. Xu, F. Kamalabadi, and S. A. Boppart, "Comparative performance analysis of time-frequency distributions for spectroscopic optical coherence tomography," Appl. Opt. **44**, 1813-1822 (2005).
138. C. Xu, C. Vinegoni, T. S. Ralston, W. Luo, W. Tan, and S. A. Boppart, "Spectroscopic spectral-domain optical coherence microscopy," Optics Letters **31**, 1079-1081 (2006).

139. R. Leitgeb, M. Wojtkowski, A. Kowalczyk, C. K. Hitzenberger, M. Sticker, and A. F. Fercher, "Spectral measurement of absorption by spectroscopic frequency-domain optical coherence tomography," Optics Letters **25**, 820-822 (2000).
140. S. Woo, K. An, C. Frank, and e. al., "Anatomy, biology, and biomechanics of tendon and ligament [Chapter 24]," in *Orthopaedic Basic Science: Biology and Biomechanics of the Musculoskeletal System*, J. A. Buckwalter, T. A. Einhorn, and S. R. Simon, eds. (American Academy of Orthopaedic Surgeons, Rosemont, IL, 2000), pp. 582-614.
141. J. Strickland, "Flexor Tendon Injuries: I. Foundations of Treatment," J Am Acad Orthop Surg **3**, 44-54 (1995).
142. M. Aoki, P. R. Manske, D. L. Pruitt, and B. J. Larson, "Tendon repair using flexor tendon splints: An experimental study," The Journal of Hand Surgery **19**, 984-990 (1994).
143. P. O. Bagnaninchi, Y. Yang, N. Maffulli, R. K. Wang, and A. El Haj, "Monitoring tissue formation and organization of engineered tendon by optical coherence tomography," in *Proceedings of SPIE - The International Society for Optical Engineering*(San Jose, CA, 2006).
144. K. A. Hansen, J. A. Weiss, and J. K. Barton, "Recruitment of tendon crimp with applied tensile strain," Journal of Biomechanical Engineering **124**, 72-77 (2002).
145. Y. Yang, L. Wu, Y. Feng, and R. K. Wang, "Observations of birefringence in tissues from optic-fibre-based optical coherence tomography," Measurement Science and Technology **14**, 41-46 (2003).
146. P. O. Bagnaninchi, Y. Yang, N. Zghoul, N. Maffulli, R. K. Wang, and A. J. El Haj, "Chitosan microchannel scaffolds for tendon tissue engineering characterized using optical coherence tomography," Tissue Engineering **13**, 323-331 (2007).
147. Y. Yang, P. O. Bagnaninchi, B. Hu, K. Hampson, and A. J. El Haj, "Characterisation of scaffold architecture and tendons using optical coherence tomography and polarisation-sensitive optical coherence tomography," IET Optoelectronics **2**, 188-194 (2008).
148. Y. Ying, and et al., "Investigation of optical coherence tomography as an imaging modality in tissue engineering," Physics in Medicine and Biology **51**, 1649 (2006).
149. C. Pitris, "High Resolution Imaging of Neoplasia using Optical Coherence Tomography," (Massachusetts Institute of Technology, 2000).
150. M. E. Brezinski, G. J. Tearney, B. E. Bouma, J. A. Izatt, M. R. Hee, E. A. Swanson, J. F. Southern, and J. G. Fujimoto, "Optical coherence tomography for optical biopsy: Properties and demonstration of vascular pathology," Circulation **93**, 1206-1213 (1996).
151. D. V. Palanker, M. S. Blumenkranz, D. Andersen, M. Wiltberger, G. Marcellino, P. Gooding, D. Angeley, G. Schuele, B. Woodley, M. Simoneau, N. J. Friedman, B. Seibel, J. Batlle, R. Feliz, J. Talamo, and W. Culbertson, "Femtosecond Laser–Assisted Cataract Surgery with Integrated Optical Coherence Tomography," Science Translational Medicine **2**, 58ra85-58ra85 (2010).
152. Olympus, "Microscopy Resource Center, (http://www.olympusmicro.com/index.html)."
153. T. H. Chow, S. Gulam Razul, B. K. Ng, G. Ho, and C. B. A. Yeo, "Enhancement of Fourier domain optical coherence tomography images using discrete Fourier transform

method," in *Progress in Biomedical Optics and Imaging - Proceedings of SPIE*(San Jose, CA, 2008).
154. T. H. Chow, W. M. Lee, K. M. Tan, B. K. Ng, and C. J. R. Sheppard, "Resolving interparticle position and optical forces along the axial direction using optical coherence gating," Applied Physics Letters **97** (2010).
155. W. J. Marshall, "Two methods for measuring laser beam diameter," Journal of Laser Applications **22**, 132-136 (2010).
156. A. E. Siegman, M. W. Sasnett, and T. F. Johnston Jr, "Choice of clip levels for beam width measurements using knife-edge techniques," IEEE Journal of Quantum Electronics **27**, 1098-1104 (1991).
157. S. T. Flock, S. L. Jacques, B. C. Wilson, W. M. Star, and M. J. C. Van Gemert, "Optical properties of intralipid: A phantom medium for light propagation studies," Lasers in Surgery and Medicine **12**, 510-519 (1992).
158. A. H. Hielscher, J. R. Mourant, and I. J. Bigio, "Influence of particle size and concentration on the diffuse backscattering of polarized light from tissue phantoms and biological cell suspensions," Applied Optics **36**, 125-135 (1997).
159. D. D. Royston, R. S. Poston, and S. A. Prahl, "Optical properties of scattering and absorbing materials used in the development of optical phantoms at 1064 NM," Journal of Biomedical Optics **1**, 110-116 (1996).
160. M. Bass, V. N. Mahajan, and E. W. Van Stryland, eds. *Handbook of optics. Volume II, Design, fabrication and testing, sources and detectors, radiometry and photometry* (McGraw-Hill, New York, 1995).
161. S. Glass, "BK7 Datasheet, http://www.us.schott.com/advanced_optics/us/abbe_datasheets/schott_datasheet_n-bk7.pdf," (2007).
162. K. A. Hansen, J. K. Barton, and J. A. Weiss, "Optical coherence tomography imaging of collagenous tissue microstructure," Proceedings of SPIE - The International Society for Optical Engineering **3914**, 581-587 (2000).
163. L. H. Nakama, K. B. King, S. Abrahamsson, and D. M. Rempel, "Evidence of tendon microtears due to cyclical loading in an in vivo tendinopathy model," Journal of Orthopaedic Research **23**, 1199-1205 (2005).
164. L. H. Nakama, K. B. King, S. Abrahamsson, and D. M. Rempel, "Effect of repetition rate on the formation of microtears in tendon in an in vivo cyclical loading model," Journal of Orthopaedic Research **25**, 1176-1184 (2007).
165. Y. Dogramaci, A. Kalaci, T. T. Sevinç, E. Esen, M. Komurcu, and A. N. Yanat, "Does strand configuration and number of purchase points affect the biomechanical behavior of a tendon repair? A biomechanical evaluation using different Kessler methods of flexor tendon repair," Hand **3**, 266-270 (2008).
166. R. H. Gelberman, M. I. Boyer, M. D. Brodt, S. C. Winters, and M. J. Silva, "The effect of gap formation at the repair site on the strength and excursion of intrasynovial flexor tendons: An experimental study on the early stages of tendon-healing in dogs," Journal of Bone and Joint Surgery - Series A **81**, 975-982 (1999).
167. T. M. Lawrence, and T. R. C. Davis, "A biomechanical analysis of suture materials and their influence on a four-strand flexor tendon repair," Journal of Hand Surgery **30**, 836-841 (2005).

168. J. B. Tang, B. Wang, F. Chen, C. Z. Pan, and R. G. Xie, "Biomechanical evaluation of flexor tendon repair techniques," Clinical Orthopaedics and Related Research, 252-259 (2001).
169. M. Vigler, S. K. Lee, R. Palti, J. C. Williams, A. J. Kaminsky, M. A. Posner, and M. R. Hausman, "Biomechanical Comparison of Techniques to Reduce the Bulk of Lacerated Flexor Tendon Ends Within Digital Sheaths of the Porcine Forelimb," Journal of Hand Surgery **34**, 1653-1658 (2009).
170. C. A. Squier, and W. H. Bausch, "Three-dimensional organization of fibroblasts and collagen fibrils in rat tail tendon," Cell and Tissue Research **238**, 319-327 (1984).
171. J. W. Strickland, "Development of Flexor Tendon Surgery: Twenty-Five Years of Progress," The Journal of Hand Surgery **25**, 214-235 (2000).
172. A. Cristiano, A. Marcellan, R. Long, C. Y. Hui, J. Stolk, and C. Creton, "An experimental investigation of fracture by cavitation of model elastomeric networks," Journal of Polymer Science, Part B: Polymer Physics **48**, 1409-1422 (2010).
173. Y. Churei, T. Yoshizu, Y. Maki, and N. Tsubokawa, "Flexor tendon repair in a rabbit model using a 'core' of extensor retinaculum with synovial membrane: An experimental study," Journal of Hand Surgery **24 B**, 267-271 (1999).
174. T. W. Lin, L. Cardenas, and L. J. Soslowsky, "Biomechanics of tendon injury and repair," Journal of Biomechanics **37**, 865-877 (2004).
175. R. N. Graf, and A. Wax, "Temporal coherence and time-frequency distributions in spectroscopic optical coherence tomography," Journal of the Optical Society of America A: Optics and Image Science, and Vision **24**, 2186-2195 (2007).
176. H. v. d. Hulst, *Light Scattering by Small Particles* ((Dover Publications, New York, New York, 1981).).
177. H. Boonstra, J. W. Oosterhuis, A. M. Oosterhuis, and G. J. Fleuren, "Cervical tissue shrinkage by formaldehyde fixation, paraffin wax embedding, section cutting and mounting," Virchows Archiv A Pathological Anatomy and Histology **402**, 195-201 (1983).
178. B. Alberts, A. Johnson, J. Lewis, M. Raff, K. Roberts, and P. Walter, *Molecular Biology of the Cell* (Garland Science, New York, 2002).
179. A. K. S. Chong, J. Riboh, R. L. Smith, D. P. Lindsey, H. M. Pham, and J. Chang, "Flexor tendon tissue engineering: Acellularized and reseeded tendon constructs," Plastic and Reconstructive Surgery **123**, 1759-1766 (2009).
180. M. A. Costa, C. Wu, B. V. Pham, A. K. S. Chong, H. M. Pham, and J. Chang, "Tissue engineering of flexor tendons: Optimization of tenocyte proliferation using growth factor supplementation," Tissue Engineering **12**, 1937-1943 (2006).
181. G. S. Kryger, A. K. S. Chong, M. Costa, H. Pham, S. J. Bates, and J. Chang, "A Comparison of Tenocytes and Mesenchymal Stem Cells for Use in Flexor Tendon Tissue Engineering," Journal of Hand Surgery **32**, 597-605 (2007).
182. R. G. Young, D. L. Butler, W. Weber, A. I. Caplan, S. L. Gordon, and D. J. Fink, "Use of mesenchymal stem cells in a collagen matrix for achilles tendon repair," Journal of Orthopaedic Research **16**, 406-413 (1998).
183. M. F. Pittenger, A. M. Mackay, S. C. Beck, R. K. Jaiswal, R. Douglas, J. D. Mosca, M. A. Moorman, D. W. Simonetti, S. Craig, and D. R. Marshak, "Multilineage potential of adult human mesenchymal stem cells," Science **284**, 143-147 (1999).

184. S. P. Bruder, K. H. Kraus, V. M. Goldberg, and S. Kadiyala, "The effect of implants loaded with autologous mesenchymal stem cells on the healing of canine segmental bone defects," Journal of Bone and Joint Surgery - Series A **80**, 985-996 (1998).
185. T. L. Arinzeh, S. J. Peter, M. P. Archambault, C. Van Den Bos, S. Gordon, K. Kraus, A. Smith, and S. Kadiyala, "Allogeneic mesenchymal stem cells regenerate bone in a critical-sized canine segmental defect," Journal of Bone and Joint Surgery - Series A **85**, 1927-1935 (2003).
186. J. M. Ryan, F. P. Barry, J. M. Murphy, and B. P. Mahon, "Mesenchymal stem cells avoid allogeneic rejection," Journal of Inflammation **2** (2005).
187. H. Ren, Y. Wang, Z. Ding, Y. Zhao, J. S. Nelson, and Z. Chen, "Phase-resolved polarization sensitive optical coherence tomography imaging of tendon and muscle," in *Proceedings of SPIE - The International Society for Optical Engineering*, V. V. Tuchin, J. A. Izatt, and J. G. Fujimoto, eds. (San Jose, CA, 2003), pp. 320-328.
188. D. J. Prockop, "Marrow stromal cells as stem cells for nonhematopoietic tissues," Science **276**, 71-74 (1997).
189. S. Aggarwal, and M. F. Pittenger, "Human mesenchymal stem cells modulate allogeneic immune cell responses," Blood **105**, 1815-1822 (2005).
190. P. A. Sotiropoulou, S. A. Perez, A. D. Gritzapis, C. N. Baxevanis, and M. Papamichail, "Interactions between human mesenchymal stem cells and natural killer cells," Stem Cells **24**, 74-85 (2006).
191. T. Ahsan, and R. M. Nerem, "Bioengineered tissues: the science, the technology, and the industry," Orthodontics & craniofacial research **8**, 134-140 (2005).
192. M. J. Lysaght, and J. Reyes, "The growth of tissue engineering," Tissue Engineering **7**, 485-493 (2001).
193. L. S. Nair, and C. T. Laurencin, "Biodegradable polymers as biomaterials," Progress in Polymer Science (Oxford) **32**, 762-798 (2007).
194. G. H. Altman, F. Diaz, C. Jakuba, T. Calabro, R. L. Horan, J. Chen, H. Lu, J. Richmond, and D. L. Kaplan, "Silk-based biomaterials," Biomaterials **24**, 401-416 (2003).
195. J. G. Hardy, L. M. Römer, and T. R. Scheibel, "Polymeric materials based on silk proteins," Polymer **49**, 4309-4327 (2008).
196. U. J. Kim, J. Park, C. Li, H. J. Jin, R. Valluzzi, and D. L. Kaplan, "Structure and properties of silk hydrogels," Biomacromolecules **5**, 786-792 (2004).
197. A. C. MacIntosh, V. R. Kearns, A. Crawford, and P. V. Hatton, "Skeletal tissue engineering using silk biomaterials," Journal of tissue engineering and regenerative medicine **2**, 71-80 (2008).
198. L. Meinel, S. Hofmann, V. Karageorgiou, L. Zichner, R. Langer, D. Kaplan, and G. Vunjak-Novakovic, "Engineering cartilage-like tissue using human mesenchymal stem cells and silk protein scaffolds," Biotechnology and Bioengineering **88**, 379-391 (2004).
199. Y. Wang, H. J. Kim, G. Vunjak-Novakovic, and D. L. Kaplan, "Stem cell-based tissue engineering with silk biomaterials," Biomaterials **27**, 6064-6082 (2006).
200. M. J. J. Liu, S. M. Chou, C. K. Chua, C. M. B. Tay, and B. K. Ng, "The study of micro- and macro-structural features of silk fibroin scaffolds," in *Proceedings of the 1st International Symposium on Bioengineering, ISOB 2011*(Singapore, 2011), pp. 330-338.
201. K. H. Low, K. F. Leong, C. K. Chua, Z. H. Du, and C. M. Cheah, "Characterization of SLS parts for drug delivery devices," Rapid Prototyping Journal **7**, 262-267 (2001).

202. M. H. Too, K. F. Leong, C. K. Chua, Z. H. Du, S. F. Yang, C. M. Cheah, and S. L. Ho, "Investigation of 3D Non-Random Porous Structures by Fused Deposition Modelling," The International Journal of Advanced Manufacturing Technology **19**, 217-223 (2002).
203. S. M. Warren, K. D. Fong, C. M. Chen, E. G. Loboa, C. M. Cowan, H. P. Lorenz, and M. T. Longaker, "Tools and Techniques for Craniofacial Tissue Engineering," Tissue Engineering **9**, 187-200 (2003).
204. C. K. Chua, K. F. Leong, K. H. Tan, F. E. Wiria, and C. M. Cheah, "Development of tissue scaffolds using selective laser sintering of polyvinyl alcohol/hydroxyapatite biocomposite for craniofacial and joint defects," Journal of Materials Science: Materials in Medicine **15**, 1113-1121 (2004).
205. K. H. Tan, C. K. Chua, K. F. Leong, C. M. Cheah, W. S. Gui, W. S. Tan, and F. E. Wiria, "Selective laser sintering of biocompatible polymers for applications in tissue engineering," Bio-Medical Materials & Engineering **15**, 113-124 (2005).
206. W. Y. Yeong, N. Sudarmadji, H. Y. Yu, C. K. Chua, K. F. Leong, S. S. Venkatraman, Y. C. F. Boey, and L. P. Tan, "Porous polycaprolactone scaffold for cardiac tissue engineering fabricated by selective laser sintering," Acta Biomaterialia **6**, 2028-2034 (2010).
207. P. J. Bartolo, C. K. Chua, H. A. Almeida, S. M. Chou, and A. S. C. Lim, "Biomanufacturing for tissue engineering: Present and future trends," Virtual and Physical Prototyping **4**, 203 - 216 (2009).
208. H. S. Ramanath, M. Chandrasekaran, C. K. Chua, K. F. Leong, and K. D. Shah, "Modeling of extrusion behavior of biopolymer and composites in fused deposition modeling," Key Engineering Materials **334-335**, 1241-1244 (2007).
209. H. S. Ramanath, M. Chandrasekaran, C. K. Chua, K. F. Leong, and K. D. Shah, "Melt flow behaviour of poly-ε-caprolactone in fused deposition modelling," Journal of Materials Science - Materials in Medicine **19**, 2541 - 2550 (2008).
210. C. K. Chua, K. F. Leong, C. M. Cheah, and S. W. Chua, "Development of a tissue engineering scaffold structure library for rapid prototyping. Part 1: Investigation and lassification " International Journal of Advanced Manufacturing Technology **21**, 291-301 (2003).
211. C. K. Chua, K. F. Leong, C. M. Cheah, and S. W. Chua, "Development of a tissue engineering scaffold structure library for rapid prototyping. Part 2: Parametric library and assembly program " International Journal of Advanced Manufacturing Technology **21**, 302-312 (2003).
212. C.-M. Cheah, C.-K. Chua, K.-F. Leong, C.-H. Cheong, and M.-W. Naing, "Automatic Algorithm for Generating Complex Polyhedral Scaffold Structures for Tissue Engineering," Tissue Engineering **10**, 595-610 (2004).
213. M. W. Naing, C. K. Chua, K. F. Leong, and Y. Wang, "Fabrication of customised scaffolds using computer-aided design and rapid prototyping techniques," Rapid Prototyping Journal **11**, 11 (2005).
214. T. W. Chung, and Y. L. Chang, "Silk fibroin/chitosan-hyaluronic acid versus silk fibroin scaffolds for tissue engineering: Promoting cell proliferations in vitro," Journal of Materials Science: Materials in Medicine **21**, 1343-1351 (2010).

215. S. Sahoo, S. L. Toh, and J. C. H. Goh, "A bFGF-releasing silk/PLGA-based biohybrid scaffold for ligament/tendon tissue engineering using mesenchymal progenitor cells," Biomaterials **31**, 2990-2998 (2010).
216. E. Suzuki, "High-resolution scanning electron microscopy of immunogold-labelled cells by the use of thin plasma coating of osmium," Journal of Microscopy **208**, 153-157 (2002).
217. D. Dziong, P. O. Bagnaninchi, R. E. Kearney, and M. Tabrizian, "Nondestructive online in vitro monitoring of pre-osteoblast cell proliferation within microporous polymer scaffolds," IEEE Transactions on Nanobioscience **6**, 249-258 (2007).
218. F. Peyrin, "Evaluation of bone scaffolds by micro-CT," Osteoporosis International **22**, 2043-2048 (2011).
219. J. J. Crowe, S. C. Grant, T. M. Logan, and T. Ma, "A magnetic resonance-compatible perfusion bioreactor system for three-dimensional human mesenchymal stem cell construct development," Chemical Engineering Science **66**, 4138-4147 (2011).
220. X. Xu, R. K. Wang, and A. El Haj, "Investigation of changes in optical attenuation of bone and neuronal cells in organ culture or three-dimensional constructs in vitro with optical coherence tomography: relevance to cytochrome oxidase monitoring," European Biophysics Journal **32**, 355-362 (2003).
221. W. Tan, A. Sendemir-Urkmez, L. J. Fahrner, R. Jamison, D. Leckband, and S. A. Boppart, "Structural and functional optical imaging of three-dimensional engineered tissue development," Tissue Engineering **10**, 1747-1756 (2004).
222. W. Tan, A. L. Oldenburg, J. J. Norman, T. A. Desai, and S. A. Boppart, "Optical coherence tomography of cell dynamics in three-dimensional tissue models," Opt. Express **14**, 7159-7171 (2006).
223. W. Tan, C. Vinegoni, J. J. Norman, T. A. Desai, and S. A. Boppart, "Imaging cellular responses to mechanical stimuli within three-dimensional tissue constructs," Microscopy Research and Technique **70**, 361-371 (2007).
224. I. Georgakoudi, W. L. Rice, M. Hronik-Tupaj, and D. L. Kaplan, "Optical spectroscopy and imaging for the noninvasive evaluation of engineered tissues," Tissue Engineering - Part B: Reviews **14**, 321-340 (2008).
225. B. Veksler, E. Kobzev, M. Bonesi, and I. Meglinski, "Application of optical coherence tomography for imaging of scaffold structure and micro-flows characterization," Laser Physics Letters **5**, 236-239 (2008).
226. Z. Wang, H. Pan, Z. Yuan, J. Liu, W. Chen, and Y. Pan, "Assessment of dermal wound repair after collagen implantation with optical coherence tomography," Tissue Engineering - Part C: Methods **14**, 35-45 (2008).
227. Y. Jia, L. An, and R. K. Wang, "Doppler optical microangiography improves the quantification of local fluid flow and shear stress within 3-D porous constructs," Journal of Biomedical Optics **14**, 050504 (2009).
228. Y. Jia, P. O. Bagnaninchi, Y. Yang, A. E. Haj, M. T. Hinds, S. J. Kirkpatrick, and R. K. Wang, "Doppler optical coherence tomography imaging of local fluid flow and shear stress within microporous scaffolds," Journal of Biomedical Optics **14**, 034014 (2009).
229. B. W. Graf, and S. A. Boppart, "Imaging and analysis of three-dimensional cell culture models," Methods in molecular biology (Clifton, N.J.) **591**, 211-227 (2010).

230. D. Levitz, M. T. Hinds, A. Ardeshiri, S. R. Hanson, and S. L. Jacques, "Non-destructive label-free monitoring of collagen gel remodeling using optical coherence tomography," Biomaterials **31**, 8210-8217 (2010).
231. E. M. Levina, M. A. Kharitonova, Y. A. Rovensky, and J. M. Vasiliev, "Cytoskeletal control of fibroblast length: Experiments with linear strips of substrate," Journal of Cell Science **114**, 4335-4341 (2001).
232. U.-J. Kim, J. Park, C. Li, H.-J. Jin, R. Valluzzi, and D. L. Kaplan, "Structure and Properties of Silk Hydrogels," Biomacromolecules **5**, 786-792 (2004).
233. P. O. Bagnaninchi, Y. Yang, N. Zghoul, N. Maffulli, R. K. Wang, and A. J. E. Haj, "Chitosan Microchannel Scaffolds for Tendon Tissue Engineering Characterized Using Optical Coherence Tomography," Tissue Engineering **13**, 323-331 (2007).
234. I. K. Angelidis, J. Thorfinn, I. D. Connolly, D. Lindsey, H. M. Pham, and J. Chang, "Tissue engineering of flexor tendons: The effect of a tissue bioreactor on adipoderived stem cellseeded and fibroblast-seeded tendon constructs," Journal of Hand Surgery **35**, 1466-1472 (2010).
235. A. B. Vakhtin, D. J. Kane, W. R. Wood, and K. A. Peterson, "Common-path interferometer for frequency-domain optical coherence tomography," Applied Optics **42**, 6953-6958 (2003).